From Quantum Gravity to Combinatorial Hives: Addressing Longstanding Puzzles with Novel Approaches

John Lombard

A dissertation
submitted in partial fulfillment of the
requirements for the degree of

Doctor of Philosophy

University of Washington

2018

Reading Committee:

Stephen Sharpe, Chair

Hariharan Narayanan

Jason Detwiler

Program Authorized to Offer Degree:
Department of Physics

University of Washington

Abstract

From Quantum Gravity to Combinatorial Hives: Addressing Longstanding Puzzles with Novel Approaches

John Lombard

Chair of the Supervisory Committee:
Professor Stephen Sharpe
Department of Physics

A thesis in two parts, this manuscript concerns the applications of contemporary techniques in optimization, network theory, combinatorial topology, and other branches of discrete mathematics to longstanding problems in theoretical physics and algebraic representation theory. We begin with an initial inquiry into the wild world of quantum gravity, reviewing the paradigm of causal dynamical triangulations as a preface to introducing our own novel approach for investigating the emergence of classical geometries from the combinatorial background. In an effort to address the question of whether macroscopic geometric order can be generated from fundamental building blocks of spacetime, we introduce, expand upon, and test the limits of an extremely general combinatorial model for quantum geometry. Along the way, we illustrate interesting model phenomenology such as an intrinsic UV scale cutoff, and, through simulations and numerical analysis, demonstrate the appearance of extended triangulations and probe the far-unconstrained regime of our model for its limiting behavior. As tools used to further characterize our theory, we introduce new algorithms for sampling on spaces of abstract simplicial complexes, and provide theoretical justification for the numerical toolkit that was constructed in the course of this study. Concluding, we state our open questions regarding this model, and propose applications of the technologies that we have developed outside the scope of quantum gravity and into the practical space of network

dynamics.

We then take an abrupt turn into the realm of combinatorial hives, a mathematical construction introduced by Knutson and Tao. After detailing the fundamentals, we examine two distinct applications of these hives: studying the geometric properties of matrix ensembles, and computing Littlewood-Richardson coefficients. To each end, we propose analytical models that additionally map onto tractable computational algorithms, and demonstrate the experimental confirmation of these algorithms. Our work includes a theoretical counterproof and local numerical counterexamples to the Appleby-Whitehead theorem on hives from Hermitian matrix pairs, as well as the first computational implementation that generates hives with almost certain probability in select matrix ensembles. We also include dual algorithms for estimating deep Littlewood-Richardson coefficients that we provide as tools that the research community may find useful.

TABLE OF CONTENTS

LIST OF FIGURES

ACKNOWLEDGMENTS

I would first like to thank my advisor and mentor, Stephen Sharpe, for his tireless encouragement that has provided me the opportunity to study such rewarding problems. You have impressed upon me priceless lessons of educational philosophy that I will forever carry with me, and without your confidence in my inquiries, this thesis would surely have never come to fruition. I extend a similar gratitude to Hariharan Narayanan, my co-advisor, for his enthusiasm in my independent work and excitement in approaching new problems together.

The faculty and resources of the University of Washington have been very generous to my studies, and I would also like to thank the Perimeter Institute, in particular Lee Smolin, for his roll in supporting my research during its burgeoning stages.

It would be terribly remiss of me to not single out Brandon Robinson, my colleague and friend, who has been an immense source of insight and conversation and has undoubtedly shaped the trajectory of my research with equal passion. How you managed to get any work done with me taking residence at your office door these past years, I'll never know.

I'd like to thank my friends for their tremendous support, both technical and lighthearted, social and serious. To Michael Wagman, Dorota Grabowska, Gabriel Magill, Christoph Uhlemann, David Sommer, Jesse Stryker, Julie Cass, my office mates Isaac Shelby and Andrew Baumgartner, Catherine Provost, and Annelise Smith—I am indebted to the kind, nurturing, and engaging environment you have surrounded me with, and I intend to pay it back though our continued friendship.

And lastly, a very large thank you for the loving foundation that my family has provided me. You carefully tended the spark in my curiosity until it grew into a bonfire, and I am eternally grateful.

DEDICATION

To the universe and its siren's call of unending mystery

Preface

The work and figures included in this thesis are largely reproduced from three papers, one of which is still in the midst of the review process for publication at the time of writing. Chapter 3 is based on "Network Gravity" [43], published in *Physical Review D*, and Chapter 6 is based on "Honey from the Hives: A theoretical and Computational Exploration of Combinatorial Hives" [44], to be published in *Experimental Mathematics*, while "A Balanced Algorithm for Sampling Abstract Simplicial Complexes" (half of the content in Chapter 5) is currently being reviewed in the journal *Methodology and Computing in Applied Probability*.

Chapter 1

INTRODUCTION TO THE 'PROBLEM' OF QUANTUM GRAVITY

We begin with a deconstruction of the term 'quantum gravity,' as its parts are independently some of the most accurate predictive models of aspects of our universe that physics has constructed.

1.0.1 Quantum

The theory of quantum mechanics, pioneered in the early 20^{th} century by the cohort of Dirac, Schrödinger, Bohr, de Broglie, and Heisenberg, stands as the reigning model for understanding the nonrelativistic and nongravitational motion of matter. Essential at the scales of the atomic and subatomic, but equally valid for much larger ensembles through the correspondence principle, quantum mechanics is a deterministic theory of probability amplitudes wherein the canonically conjugate quantities that characterize the motion of a particle, its position and momentum, are inherently nondeterministic in nature and obey an uncertainty relation that prevents the absolute knowledge of either. Combined with the theory of special relativity and the promotion of our fundamental objects to fields, relativistic quantum field theory (QFT) is a framework in which the standard model of particle physics, our strongest predictive model, is capable of computations that, in some cases, agree with experimental results with a precision better than one part in a billion [26].

1.0.2 Gravity

Our classical theory of gravity, Einstein's theory of general relativity (GR), introduces the symmetry of diffeomorphisms (general coordinate reparameterization invariance) as a fun-

damental property of our universe and establishes the dynamic structure of spacetime as the classical backdrop in which matter is embedded. Particles naturally follow geodesic paths in spacetime, and the warping of this background due to the presence of energy is responsible for experimentally confirmed predictions such as the bending of light around celestial bodies. Without corrections from general relativity, the clocks that are crucial for many of the world's communication and positioning systems would become unsynchronized [6].

1.0.3 Problem?

One often overhears in the rumblings of popular science that quantum mechanics and general relativity are deeply incompatible. This errant statement relies mainly on the notion that either quantum mechanics or general relativity tend to produce suspect results when performing computations that require corrections from both compared to a classical non-relativistic picture. However, the careers of quite a large number of physicists (and the content in this thesis) would be largely irrelevant if this were the case, as it is clear from the experimental confirmation of our models that both theories have remarkable applicability to our universe, and the mode of failure comes through attempts to erroneously push one (or both) of these theories outside of their realm of validity and expect sensible answers. In this sense, we maintain that in the context of regimes of applicability, there is no such incompatibility between these models wherein we face a problem of the likes that in light of GR, QFT must be 'wrong' or *vice versa*. However, knowing their limitations, the last century has been filled with endeavors to extend QFT to appropriately handle gravitation, canonically quantize GR in some way, or otherwise combine them under a unified theory with applicability over a larger domain. It is by no means a necessity of nature that such a unified theory exist, but from a model-building perspective, one is motivated through historical precedent with successful unifications of other theories (for a famous example, see the electroweak unification [65]) and a modern view of addressing questions through the framework of effective field theories. Nature doesn't guarantee our ability to model it with indefinite accuracy without simply pushing inconsistencies from one area to another, Gödel

incompleteness notwithstanding, but we can certainly try. Many of the approaches we study take the process of quantization through the Dirac procedure to hold true, and then apply these techniques to gravity. We will not dwell on extensions of QFT (which often naturally lead to string theory) in this thesis, but instead expand upon elements of a theory of gravity, quantized.

As exemplified in Newtonian physics, there are parameters and scales that serve to indicate where a model maintains predictive accuracy. For the regime of quantum gravity, Max Planck in 1899 identified combinations of fundamental constants of our universe that yield the scales of length, time, and temperature around which we expect quantum gravitational effects to manifest strongly [55]. With the gravitational constant G, speed of light c, quantum of action $\hbar$, and Boltzmann constant k_B, these are

$$\begin{aligned} l_P &= \sqrt{\frac{\hbar G}{c^3}} \approx 10^{-35} m\,, \\ t_P &= \frac{l_P}{c} \approx 10^{-44} s\,, \\ T_P &= \frac{\hbar c}{l_P k_B} \approx 10^{32} K\,. \end{aligned} \tag{1.1}$$

We note that these regimes are clearly extremes of our universe, and in terms of direct experimental probes, we do not yet know how to access them. However, not every prediction of a quantum theory of gravity requires extremes, and there are a host of macroscopic results and experiments that can also inform us as to the nature of quantum gravity [22, 18]. Yet even without any experimental results to shape our theories, we know from our existing models many characteristics that we expect a theory of quantum gravity to have. At the least, quantum gravity must produce results that we know to be valid in the regimes where QFT and GR are independently applicable, and semiclassical or perturbative quantum gravity from frameworks like QFT on curved spacetimes provide windows into this transition. However, the burning questions that quantum gravity hopes to answer, and one of the primary questions concerned in this thesis, are questions in the regime far removed from these treatments.

Foremost, we face a question of time: how do we reconcile the usage of time as a fixed external parameter in quantum mechanics, while it is a dynamic quantity in GR? And in a similar vein, QFT is defined on patches of the flat Lorentzian Minkowski space in order to invoke the Poincaré invariance necessary in defining particle representations. This creates a background dependence that is counter to the intrinsic nature of GR. Constructing a truly background-independent theory is essential for a theory of quantum gravity.

We also face questions about singularities: from black holes to the big bang, what happens to the topology of spacetime in these extreme regions? Models for quantum gravity should aim to resolve these singularities with analytically well-behaved physics.

Lastly, we face questions of the emergent geometry of our universe. Science has progressed immensely whenever we pose the question, 'What is it made out of?', and through experimental probes and theoretical models, we have developed a strong sense of the constituent components of matter. We should apply the same line of inquiry to spacetime itself in an attempt to ascertain a more fundamental description. Are there quantum building blocks to spacetime, and what are their dynamics? If one were to examine the interface between our universe and the absolute empty state—the ultimate vacuum wherein there is no spacetime at all—what physics lies at this boundary? Can we develop a model where spacetime is an apparently classical phenomenon at the macroscopic level, while its fundamental nature strays far from our familiar manifold description? And in this way, can we then ask and address basic questions about the structure of our universe—why do we appear to live in a four dimensional spacetime, and in short, can we formally mathematically model how one might 'weave the fabric of spacetime' itself?

Although broad and nearly philosophical questions, these are very much questions that a theory of quantum gravity may hope to rigorously answer. In fact, due to the delicacies of understanding measurement in a background-independent fashion with relational observables, the questions of quantum geometry and the patchwork nature of emergent spacetime naturally arise and must be contended with when one studies quantum gravity. These are the questions that we aim to make meager contributions toward resolving in the first part of

this thesis.

Chapter 2

MOTIVATION AND A BACKGROUND IN CAUSAL DYNAMICAL TRIANGULATIONS

2.1 What Does Quantum Geometry Look Like?

Macroscopically, we model the geometry of our universe as a smooth Lorentzian manifold that we call spacetime. The dynamics of this manifold and its warping due to energy are governed by our classical theory of gravity, general relativity. At the quantum gravity scale, however, we do not expect spacetime to have a manifold structure [59]. Quantum observables are measured by expectation values of operators over superpositions of states that live in a Hilbert space. As such, assuming quantum foundations, associated geometric observables such as areas or volumes should also be given by expectation values over corresponding Dirac quantized operators from classical gravity instead, which under a coarse macroscopic limit, return to a familiar metric construction.

Frameworks such as weak-field QFT or even perturbative string theory require a background metric, and as a result, the starting point of the theory may not provide insight into the foundational structure of spacetime in the regime where the background simply may not admit a metric topology [54]. For example, if one were to find a quantized metric that vanishes in certain regions, there would be no way to appropriately define the metric inverse. A perturbative approach that treats the metric as some series expansion around a well-behaved background, however, still admits an inverse defined in the same perturbative way, and as a result, Planck length effects that may include topology change are best investigated within a framework that avoids any such expression that inadvertently 'smooths out' such quantum effects. Pedagogically and historically, it is in our best interest for model building that we avoid any assumptions about the nature of quantum geometry as informed from the classical

world other than what one should aim to recover in an appropriate limit. In fact, one can examine this prospect from a very general representation theory perspective and ask about the support of a measure with the appropriate diffeomorphism symmetry on a Hilbert space of quantized geometries. In the mid 1980's, Isham pursued this line of inquiry and discovered that although one will find states that smear out singularities and provide conventional metrics that correspond to classical states, the measure is actually concentrated precisely on random T-sets—general topological spaces that are very likely to be fractal and certainly far from our picture of smooth manifold geometry [34]. Thus, although it is certainly more challenging to start so far removed from our familiar setting of modern physics, starting from a model that precludes such states would be disingenuous.

With this in mind, other background-independent approaches to quantum gravity have been attempted. For example, loop quantum gravity (LQG) attempts to address these questions directly with geometric operators in a noncanonical loop space of states that can act on the absolute empty state to produce objects called 'spin-networks' corresponding to chunks of spacetime [58]. The operators of area and volume are found to have discrete spectra, which give us an intuitive picture of quantum space as fundamentally atomic. The covariant spinfoam framework also attempts to address these questions. The spinfoam quantization of a constrained topological background field (BF) theory is based on an arbitrary simplicial decomposition of an underlying base manifold [7]. The construction admits nonsimplicial states—those where the quantum nature of the geometric operators only loosely impose the constraint conditions for realized geometries. These states are argued to peak to classical geometries in the appropriate limit.

An approach to probing quantum geometry that has a foundation much more familiar to the general physicist in terms of its techniques comes from the paradigm of dynamical triangulations, which we will now dive into with more detail.

2.2 Dynamical Triangulation Approach

2.2.1 Statistical Physics

The aim of many questions in statistical physics is to understand the probabilistic nature of certain observables of a system. Observables are random variables, often corresponding to physical quantities of interest, that can be studied to ascertain their statistical properties such as average values and fluctuations. One of the critical constructions for understanding statistical systems is the partition function, which contains a probability measure over the space of states and provides a weighting dependent on the physics of the system at hand. In the late 19^{th} century, Boltzmann developed a measure, later formalized by Gibbs, that applies to a vast array of statistical systems [29]. It is this measure that we will be focusing on, as its correspondence with the path integral approach to quantum mechanics has been an extremely fruitful tool for understanding our models.

Consider an ensemble consisting of a finite number of states ϕ in a state-space Φ that have compact and discrete support over the Gibbs measure. In natural units, for a given equilibrium background temperature T, the expected value of a random variable A is given as follows:

$$E[A] \equiv \frac{\sum_{\phi\in\Phi} A(\phi) e^{\frac{-S_E[\phi]}{T}}}{\sum_{\phi\in\Phi} e^{\frac{-S_E[\phi]}{T}}} \,. \tag{2.1}$$

The normalizing factor in the denominator,

$$Z \equiv \sum_{\phi\in\Phi} e^{\frac{-S_E[\phi]}{T}} \,, \tag{2.2}$$

is known as the partition function. Here, what is usually called the energy associated with a given state we denote $S_E[\phi]$, a 'Euclidean action' that is a state functional equivalent to the energy. The utility of introducing this object here will become apparent shortly. Rewriting our sum over possible values of the action, we can introduce $\Omega(S_E[\phi])$ to denote the state

multiplicities associated with a given energy:

$$Z = \sum_{S_E[\phi]\forall\phi\in\Phi} \Omega(S_E[\phi]) e^{\frac{-S_E[\phi]}{T}} . \tag{2.3}$$

Recall that entropy S is associated with the number of microstates of a given macrostate of a system, which in natural units goes as $S[S_E[\phi]] = \ln(\Omega(S_E[\phi]))$. Thus, rearranging, we find

$$Z = \sum_{S_E[\phi]\forall\phi\in\Phi} e^{-\frac{(S_E[\phi]-TS[S_E[\phi]])}{T}} . \tag{2.4}$$

One should note that the measure is concentrated where the parenthetical term $(S_E[\phi] - TS[S_E[\phi]])$, known as the 'free-energy,' is minimized. In the zero temperature limit, the minimization is an example of the 'principle of least action,' an ansatz that claims that nature prefers configurations that extremize the action. This principle is employed in the path integral in Minkowski field theories for computing transition amplitudes or other observables, and, through a saddle point approximation, one can see the correspondence to the classical equations of motion. There, the wave function can be constructed from superpositions of amplitudes that are proportional to $e^{i\frac{S[\phi]}{\hbar}}$, where for a $(3+1)$D theory of a scalar field ϕ,

$$S[\phi] = \int dt \int d^3x \mathscr{L}[\phi] . \tag{2.5}$$

The action here is the classical action functional related to the Lagrange energy density $\mathscr{L}[\phi]$ for a field configuration ϕ. Under a Wick rotation to Euclidean time $\tau \equiv it$, the Lagrange density turns into a Hamiltonian density, and the action becomes replaced by the energy functional of the field. With $\hbar \to T$, we recover the form of the Gibbs partition function above and make apparent the relationship between a zero-temperature statistical theory and the classical $\hbar \to 0$ limit of a Wick-rotated quantum field theory.

However, such path integrals as mathematical objects are often only formal symbols due to the difficulty in defining the measure, and as we will be primarily interested in understanding observables on generic spaces of states in a statistical sense, we will aim to avoid introducing these complexities as much as possible. Furthermore, we will be primarily

working in Euclidean spaces and will drop our subscripts on the action henceforth without worrying about Wick rotations.

As a matter of philosophy, the action that we will define for our theory should be taken as an *effective* Euclidean action that aims to reproduce classical physics as extrema in the regimes of applicability. We will not derive any action from first principles, as it is not clear what a 'first principles derivation' would be for studying emergent geometry where we are attempting to uncover exactly what entities are fundamental, and concepts like a Lagrangian energy density, or even 'density' itself, are not well defined until one considers a classical macroscopic limit. As we are not constructing the kinematic state space from the ground up, we will be satisfied with studying the properties of a system that, by assumption, can be described by our effective action, and attempting to understand what lessons can be learned by drawing parallels to physical theories through model phenomenology.

It should be clear that, given a way of enumerating the states in our system, and provided a well defined effective action, we can now begin to probe the statistical properties of observables. Enumerating the states will prove to be the most difficult problem to surmount.

2.2.2 Sum Over Geometries

Using the path integral approach to understanding the wave function of what may be considered the ground state amplitude for a particular geometry, Hartle and Hawking introduced a proposal that treated the partition function as a state sum on the space of all compact positive-definite 4 dimensional geometries with a fixed 3-geometry as their boundaries [30]. A 'sum over geometries' approach to quantum gravity, the goal of the proposal was to compute the probability amplitude for the ground state geometry to appear from the empty state—or in other terms, the probability amplitude for "the universe to appear from nothing." Handling the generic case of all 3-manifolds, while dealing with the large symmetry group of diffeomorphisms, is a tall order. The original computation restricted to particular symmetric compact manifolds with a positive cosmological constant where the scale factor is the only gravitational degree of freedom to aid this. However, general questions on the

full space were left unanswered, and as argued by Isham, treating the measure of quantum gravity as concentrated on smooth metrics is a questionable start for understanding quantum geometry [34].

A more general approach to formalizing the geometry state sum comes in the form of dynamical triangulations. These are nonperturbative background-independent paradigms in the sense that the path integral is computed explicitly, and no initial geometry is singled out in the formulation. In Euclidean dynamical triangulations (EDT), the space of all geometries on a smooth manifold M is given by

$$\mathrm{Geom}(M) \equiv \mathscr{M}/\mathrm{Diff}(M)\,, \tag{2.6}$$

where $\mathscr{M}$ is the space of metrics on M, and we take equivalences classes with respect to diffeomorphisms. To get a handle on this space, we consider a simplicial regularization in terms of piecewise linear manifolds, or Regge geometries at some finite length scale. These discrete triangulations of the manifolds provide analytic parameterizations with which one can then enumerate inequivalent metrics up to a symmetry given by $\|\mathrm{Aut}(T)\|$, the order of the automorphism group that takes a triangulation into itself under a relabeling of the vertices. Once such a state sum is performed, one can look for continuum limits that do not depend on the regularization details. In this way, we return to a picture of statistical physics on the space of random surfaces, each weighted by the usual Boltzmann weight where the action depends on the nature of the geometry of each state.

2.2.3 Regge Action from the Einstein-Hilbert Action

The action for continuum classical gravity on a smooth manifold M is given by the Einstein-Hilbert action:

$$S_{EH} = \int_M \sqrt{-g}(R - 2\Lambda)\,, \tag{2.7}$$

where the Jacobian is built from the metric determinant g, R is the Riemannian Ricci scalar, $\Lambda \in \mathbb{R}$ is the cosmological constant, and we have suppressed the gravitational coupling. The volume-weighted curvature form of this action can be effectively discretized for triangulations of a d-dimensional manifold, giving us the action of Euclidean Regge calculus (suppressing boundary terms):

$$S_R = \sum_h V_h \epsilon_h + \Lambda \sum_\sigma V_\sigma \,, \tag{2.8}$$

where d-simplexes are indexed by σ, $(d-2)$-simplexes (hinges where curvature is concentrated) are indexed by h, simplicial volumes V replace the continuum Jacobian, and deficit angles ϵ replace the Ricci curvature [57][25]. The sign of the cosmological term is changed from the Einstein-Hilbert action (and from other formulations of the Regge action), as we will later be considering Λ to be providing a homogeneous curvature contribution on the simplicies. Subtleties on how the deficit angles specify the corrected curvatures are suppressed as they are not integral to the discussion, but for more details, see [8].

It is not difficult to motivate this discrete action in 2 dimensions. There, the curvature is concentrated around the vertices, where the sum of the angles of the adjoining triangular vertices meeting at a given point give rise to the curvature deficit—any deviation from 2π indicates intrinsic curvature. The volume terms follow naturally from the simplicial volumes that cover the space.

2.2.4 EDT Failures and CDT Successes

Euclidean dynamical triangulations in 4 dimensions have a storied history that results in a phase diagram of emergent geometries that does not agree with our current picture of the universe. To quantify this, the Hausdorff dimension is used as an observable, which is a 'box-counting' measure of geometric dimension that agrees with the topological dimension for smooth shapes but can easily be applied to fractals, yielding fractional dimensions. In one phase, the states that are produced have a Hausdorff dimension of infinity. That is to say, the geometries are crumpled up such that any site is essentially one link away from another.

In the other phase, the states resemble branched polymers where effectively 2-dimensional geometries emerge as spindles. Neither of these represent the extended macroscopic 4D universe we would hope to emerge in a classical continuum limit. For a brief summary of the history of Euclidean dynamical triangulations, see [41].

First introduced in 1998 by Renate Loll, the causal dynamical triangulation (CDT) paradigm is a modification to the previous Euclidean attempts that introduces a proper Wick rotation and a causal structure to the triangulations [40]. The main ingredients for a 4D CDT are regular 4-simplex building blocks with fixed attachment rules and edge lengths. Spacetime is assumed to admit a foliation such that a global time coordinate intrinsic to the space can be established, and the topological structure is some $M^3 \times \mathbb{R}^1$. For convenience, the 3-manifolds are taken to have the topology of spheres. At this stage, the path integral amounts to summing over all possible gluings of all possible triangulations of spheres that respect causality, where temporal links are arranged to connect the spatial slices. Not every Euclidean manifold admits a Lorentzian analogue, and as a result, the restriction on the space of geometries can be shown to yield a different phase diagram in the continuum limit.

Numerical results indicate the emergence of a new geometric phase of extended geometry with a macroscopic spectral dimension of 4 and a microscopic fractional dimension slightly greater than 2, signaling nonclassical behavior at the short-distance scale [1]. The spectral dimension,

$$d_s = -2 \lim_{\sigma \to \infty} \frac{\ln p_\psi(\sigma)}{\ln \sigma}, \tag{2.9}$$

is a diffeomorphism-invariant measure of dimension related to the physical dimension through the discrete Laplacian, where $p_\psi(\sigma)$ is the return probability of a discrete diffusion of length σ on the triangulation.

2.2.5 Generalizing a Dynamical Triangulation

There remain many open questions on the CDT paradigm and results. Foremost, although we see that the causal constraints admit a new phase of emergent geometry, is causality truly

a *necessary* condition for emergent geometry? And furthermore, the topology restrictions, foliation assumption, triangulation constraints and forbidding of topology change obstructs what one can truly hope to discover about the emergent dimensional properties of the universe when so much is fixed or restricted *a priori*. If one hopes to ask the very general question of "Why do we appear to live in a macroscopic 4-dimensional spacetime?", it seems natural that the methods and models used to probe such an inquiry should be as agnostic as possible to any topological dimension. This takes us far away from many of the approaches to quantum gravity mentioned thus far. Even the spinfoam framework with its states distant from classical geometries still requires one to prescribe which dimensional BF theory one hopes to quantize, and as such, the literature is filled with work on 3d and 4d spinfoam models as quantizations of 3d and 4d gravity [53]. Although these models are further achievements toward a geometric and nonperturbative understanding of quantum gravity, here we take the perspective that absolute emergent dimensionality might be a property that a theory of quantum gravity could hope to explain.

The goal of the construction to follow is to investigate the limit of Euclidean classical geometries emerging from a fundamentally combinatorial network framework that does not presume the properties of an underlying triangulation. The field of emergent networks is a highly active area of research where the physical applicability of a model is often determined *a posteriori* to the growth paradigm. Here, we attempt to make rigorous a stochastic growth paradigm that is designed specifically to probe questions in emergent simplicial geometry without guiding the growth structure 'by hand', starting with a basic combinatorial structure and asking in what limits can it be demonstrated to contain substructures that approximate more familiar geometric constructions. If quantum geometry admits such a description, an analytical handle on emergent near-simplicial manifolds with nonsimplicial defects may be obtained that will facilitate a better understanding of the semiclassical limit for the very strange quantum structures we expect at that scale. Observational evidence and phenomenological bounds for a discrete structure to our universe could be ascertained by studying precisely such defects [32][33].

In Chapter 3, we will define our model and the covering space that allows us to sample our partition function around ensembles that minimize our effective classical action. We will discuss analytic properties of the action, give an intuitive picture for the correspondence between our parameters and regimes of the model which may give rise to physical macroscopic geometry, compute closed-form expressions for some symmetric states and study their behavior, and illustrate the first glimpse of emergent geometry from a combinatorial background through our simulated annealing procedure.

Chapter 4 will continue our analysis, and in addition to introducing new metrics on our space, we develop full quantum simulations on a regime of the model that admits such a probe. We explore this space, studying this model in the extreme combinatorial and ambient dimensional limits in an effort to better understand its infrared behavior.

Chapter 3

COMBINATORIAL NETWORK GRAVITY

3.1 Brief Summary

The framework we develop has two complementary pictures. On one side, we define a space of states with boundaries built from a highly constrained, purely combinatorial structure. Every such state admits a representation as an embedded abstract simplicial complex with geometric realization at the skeletal levels. On this space, we define a Euclidean action that is a heuristic combinatorial analogue of the Regge action. We study the properties of this system and can sample the action-weighted space of states through traditional Markov Chain Monte-Carlo (MCMC) sampling techniques.

On the other side of the framework, we consider a space of unconstrained states consisting of embedded undirected networks with boundaries. We consider a stochastic process on the space of emergent networks and seek to sample the distribution of optimized final states for a finite horizon growth procedure under the evaluation of a scalar cost function.

We show through the explicit construction of the surjective covering that the space of embedded emergent networks can be mapped onto our combinatorial state space of interest. Equating the cost function with the combinatorial action, the optimization procedure on the embedded graph states translates into an importance sampling on the combinatorial space, generating an ensemble that is peaked around the minima of the action and allows for discrete topological observables to be computed against the states near classical fixed-points to gain insight into the concentration of the combinatorial measure as an effective model for emergent geometry.

3.2 State Spaces

We first take the opportunity to rigorously define the space of states, both on the combinatorial side with Ψ_m representing the gauge fixed space of physical states, and in the emergent network picture with $\tilde{G}_m$ as the corresponding embedded graph space. Once this is established, we will demonstrate the covering between the spaces with an explicit construction of the map. We can initially set aside any boundary considerations, defining a generic bulk state instead. The addition of boundaries will be shown to constrain the spaces, but will not impede the general construction.

3.2.1 Combinatorial State Definition

A state $\phi_m \in \Psi_m$ can be represented by a simple (excludes single-node loops and multi-edges between the same nodes) graph, where V is the vertex set:

$$\{v_i\}|\{v_i \in V \,\forall\, i \in [|V|]\} \ ; \tag{3.1}$$

and E is the edge set:

$$\{(v_i, v_j)\}|\{(v_i, v_j) \in E\} \, . \tag{3.2}$$

This graph has a number of distinct properties that we will detail: it is leveled, rooted, directed, weighted, and constrained. These properties make the state space difficult to numerically sample, as it is challenging to establish a random walk on this space that can be used in traditional MCMC methods. Chapter 5 details some algorithms which are used to sample specific regimes of this space. However, our use of an unconstrained covering will provide us with a relaxed space that is much more amenable to simulation and lends us a tool for studying Ψ_m through projection.

A graph representation of the combinatorial state is first constructed by distinguishing a vertex subset as roots. From these roots, all edges will be directed with an outward orientation. The rest of the vertices in the state are divided into further subsets denoted 'levels,' which we will now define through the use of directed paths, or 'dipaths.'

Let us denote rooted dipaths of edge cardinality d (directed paths starting at a root vertex and containing d edges in the graph) as P_d. The state has maximal dipaths P_m, and the leveled vertex subsets are indexed by the order of the dipath arriving at that vertex, $0 \leq d \leq m$. Strictly, each level consists of the vertex subsets defined by the union of the terminals T of P_d,

$$V|_d \equiv \cup_i v_i \,|\, \{v_i = T(P_d) \,\forall\, P_d\}\,. \tag{3.3}$$

For example, the set of vertices at level $d = 0$, $V|_0$, constitute the roots of the graph, while all vertices arrived at by following dipaths from roots through 2 consecutive edges are vertices at level $d = 2$, $V|_2$. The outward orientation of the edges is propagated through this structure, with the foot and head of each edge directed from lower to higher leveled vertices. Furthermore, edges are constrained to connect only vertices at level d with those at level $(d-1)$. That is, no edge can 'skip' over a level. Beyond the roots, the number of edges incoming on a vertex at level d is $(d+1)$.

Lastly, there is a weighting $\omega_{\alpha_d} \in \mathbb{R}^+$ assigned to each vertex. We illustrate this structure in Fig. 3.1 for an example state ϕ_m.

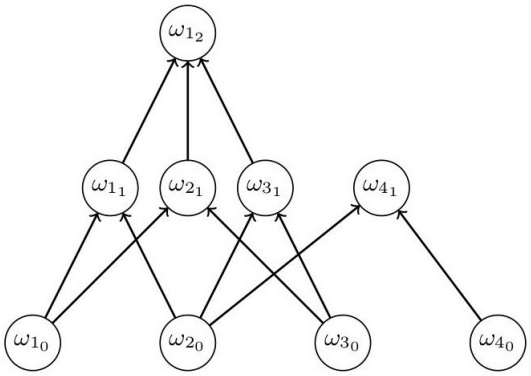

Figure 3.1: Representative of a Combinatorial State. We draw the reader's attention both to the roots of the graph at the 0 level indicated by the outward orientation of all of the directed edges (and the corresponding 0 labels on the weights), and the linked structure of the 3 levels.

We can now repackage the levels V_d into a data structure that also defines the connectivity data between each level. We parameterize our state in terms of adjacency data K^* and weights ω_{α_d}, where $K^* = \sqcup_{d=0}^{m} K_d^*$ and each K_d^* is an ordered set that specifies data at a given level. As demonstrated in Fig. 3.1, we maintain α as a vertex label on the indexing set $\alpha \in [|K_d^*|]$ for each level.

To define the data structures K_d^*, we take each vertex's α_d to encode the unique subset $\{\alpha_0, \ldots, \alpha_0\}$ of $d+1$ root vertices that the dipaths terminating at α_d originate from. To give an explicit example from our state in Fig. 3.1, the left-most vertex on level 1 is connected to the two left-most roots, and thus has the following α_d structure:

$$\alpha_d = 1_1 = \{1_0, 2_0\}\,. \tag{3.4}$$

The structures on the roots are themselves defined implicitly as the singletons

$$\alpha_0 \equiv \{\alpha\}\,\forall\,\alpha \in [|K_0^*|]\,. \tag{3.5}$$

Uniqueness is characterized by $|\alpha_d \cap \beta_d| < |\alpha_d|\,\forall\,(\beta \neq \alpha)$.

To illustrate the K^* structure of Fig. 3.1, we enumerate the components of the disjoint union at each level with a lexicographical ordering imposed on the roots as follows:

$$\begin{aligned} K_0^* &= \{(\{1\},1),(\{2\},2),(\{3\},3),(\{4\},4)\}\,; \\ K_1^* &= \{(\{1,2\},1),(\{1,3\},2),(\{2,3\},3),(\{2,4\},4)\}\,; \\ K_2^* &= \{(\{1,2,3\},1)\}\,. \end{aligned} \tag{3.6}$$

The reason for this parameterization and particular choice of labeling will become clear in Eq. 3.11 when we define the projection from the embedded picture onto this combinatorial description, where such a structure is natural. We will see that the graph levels correspond to projections of skeletal decompositions of our embedded state, with each vertex corresponding to a geometrically realized simplex of order d and simplicial volume ω_{α_d}.

For further insight into the structure, we note that if one were to remove the vertices at level 1 and instead let the roots continuously connect in an undirected fashion through the

structure prescribed by K_1^*, one would see that all vertices at level d can be be traced back to cliques (complete subgraphs wherein every vertex is connected to every other vertex in the subgraph) of order $(d+1)$ in the joined root graph. Referring back to our example state in Fig. 3.1, tracking back the highest vertex 1_2 yields the roots $\{1, 2, 3\}$, which would form a clique of order 3 between their connections via level 1. We note that not every clique one could form between the roots automatically induces a vertex in the full state, however, and it is this distinction that encodes many of the geometric defects in the embedded picture.

In addition to the defining properties of this parameterization, there are a host of combinatorial inequalities that must be enforced on the weights and edges to restrict to the state space we are interested in. These come in the form of embeddability restrictions and weight inequalities such that we admit the most general combinatorial structure that will still be compatible with the notions of volume and curvature that we will employ.

For a fixed K^* structure, there are determinant inequalities on the weight structures from Eq. 3.24a to insure that there exists some simplicial volume greater than ω_{α_0} provided a range of edge lengths, and inequalities that come from embeddability. The embeddability requirements are the most difficult to characterize. These dictate, for example, that for any closed $(m-1)$-surface A in an ambient m-space, every permutation of sums of the surface-weights with a single element $\hat{\alpha}$ removed must be greater than the weight of the removed element:

$$\Big(\sum_{\alpha_{m-1}\neq\hat{\alpha}_{m-1}\in K^*_{m-1}|_A} \omega_{\alpha_{m-1}}\Big) > \omega_{\hat{\alpha}_{m-1}} \,\forall\, \hat{\alpha}\,. \tag{3.7}$$

These include the higher dimensional closure inequalities on the weights for given simplexes by taking the surface to be a single element (like the triangle inequalities), but also extend to surfaces that live entirely in sub-dimensional hyperplanes. There are further constraints that are even harder to characterize: for example, given a vertex in 2 dimensions that is surrounded by simplically attached 2-simplexes except for a small deficit, one needs inequalities on the allowed 2-simplex that would only share the internal vertex and live in the remaining ambient 'wedge,' which is a highly nonlocal and nontrivial inequality.

Furthermore, the existence of combinatorial boundaries presents equality constraints on the allowed level-1 weights connecting boundary roots, which can be seen more clearly in the embedded picture as constraints due to the relative positioning of the fixed boundary structures.

We lastly enforce that if there is the right lower combinatorial and weight structure to admit a higher leveled node which can correspond with a properly embedded geometric realization of a simplex, then such a vertex is forced on the state. This is a model ansatz that is motivated from the drive for a dimensionally agnostic model wherein if there *can* be a geometrically realized structure, there is one. A relaxation of this ansatz into a larger space of states is considered in the investigations in Chapter 4.

A full understanding of when an abstract simplicial complex can be embedded in a fixed dimensional Euclidean ambient space with prescribed simplicial volumes is tractable for 1 dimension and possibly for 2 dimensions, but immediately becomes unwieldy for higher dimensional spaces.

3.2.2 An Embedded State

Having defined a combinatorial state, we now introduce a complementary embedded graph state that will be mapped onto our combinatorial space, providing us with a much more intuitive picture of the geometry at hand and a space that is easily samplable (although taking us a step away from our actual space of interest and thereby requiring care in understanding what physics we can rightfully gleam through the projection).

Let $g(V, E)$ be an simple undirected graph. Let $\chi_m : g \mapsto \tilde{g}_m$ be a fixed embedding of g into $\mathbb{R}^m$:

$$\begin{aligned} \chi_m(v \in V) &\mapsto p \in \mathbb{R}^m\,, \\ \chi_m((v_i, v_j) \in E) &\mapsto l_{[p_i,p_j]} \in \mathbb{R}^m\,, \end{aligned}$$

with the restrictions that $\chi_m(V(g))$ is injective such that we do not allow points to be degenerate, and $\chi_m(E(g))$ is the collection of unique geodesic line segments $l_{[p_i,p_j]}$ between

connected points p_i and p_j. The path lengths are thus given by the L_2 norm between the embedded point coordinates, inherited from the induced metric on the ambient space.

We consider $\tilde{g}_m = \tilde{g}_m(g, \chi_m)$ to be our parameterization of an embedded graph state.

In Fig. 3.2, we illustrate an example of such a state. This state, under the projection that we will define in Sec. 3.2.3, will have the same combinatorial data as our example in Fig. 3.1 for a specific choice of weights. That is, this simple graph state is equivalent to our constrained combinatorial picture as far as the combinatorial data is concerned.

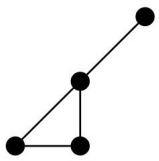

Figure 3.2: A Representative Embedded Graph State that Projects into the State Illustrated in Fig. 3.1

3.2.3 From Embeddings to Combinatorics

From $\tilde{g}_m$, we will explicitly construct the map μ that uniquely projects onto the combinatorial space.

First, given $\tilde{g}_m$, we can construct its ordered clique complex. Let a complete subgraph of order $(d+1)$ (a $(d+1)$-clique) in g be denoted $\alpha_d \equiv \{v_i \cdots v_j\}$, where α is a labeling on the set of complete subgraphs at fixed order and v_i are the constituent vertices. Every α_d is in bijection with a combinatorial simplex of order d. We form the ordered clique complex by taking the disjoint union of simplexes associated with each complete subgraph. That is, define the clique skeleton at order d to be the following:

$$K_d \equiv \sqcup_\alpha \alpha_d \,|\, \{\alpha \in [|K_d|]\}\,. \tag{3.8}$$

This complex is an embedded abstract simplicial complex. A traditional simplicial complex has stringent requirements on the intersections of its simplicies such that the intersection

of two simplicies occurs as a subset of the union of their boundaries that is also a lower dimensional simplex. An abstract embedded complex has no such restrictions. Additionally, not every complete subgraph in a simplicial complex actually forms a simplex, as opposed to a clique complex. Fig. 3.3 illustrates this difference.

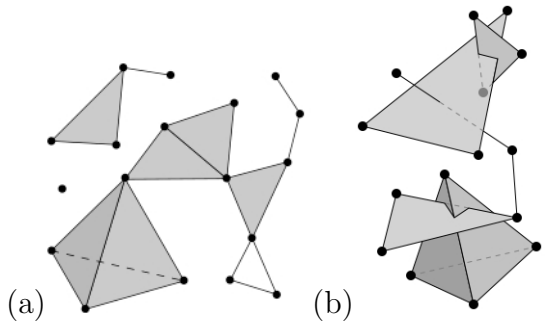

Figure 3.3: A Simplicial Complex (a) and a Clique Complex (b), both Embedded in $\mathbb{R}^3$

We introduce a map

$$\Omega : \tilde{\alpha}_d \to \mathbb{R}^+ \tag{3.9}$$

that computes simplicial d-volumes of embedded cliques $\tilde{\alpha}_d$. As discussed, the cliques may not have a well defined geometric realization under χ_m and as a result we are unable to generically define a proper volume for them. To rectify this, we generate a set of individually embedded cliques by restriction, compute the volumes in this isolated space where there is guaranteed to be such a proper notion, and map the combinatorial information back to the full state through coherent indexing. This is a formal trick we use in order to 'precompute' what the simplicial volumes would be if the elements were all geometrically realized. In practice, this step need not be numerically implemented in the algorithm, as our formulae for simplicial volumes are naturally insensitive to this concern and only depend on the embedded vertex points.

Let R_{α_d} be a restriction map such that

$$R_{\alpha_d}(g(V,E)) = g(\alpha_d, E|_{\alpha_d})\,. \tag{3.10}$$

Each individually embedded clique is simply

$$\begin{aligned} \chi_m(R_{\alpha_d}(g)) &\equiv \tilde{\alpha}_d = (\overbrace{p_i \cdots p_j}^{d+1}) \\ p_i &= \chi_m(v_i) \in \mathbb{R}^m \,, \end{aligned} \tag{3.11}$$

using the same indexing on α_d to carry the labeling data between the maps.

Now we can let $\omega_{\alpha_d} \equiv \Omega(\tilde{\alpha}_d)$.

Define the following structure as a skeletal subset:

$$K'_d \equiv \sqcup_\alpha \alpha_d \,|\, \{\, \omega_{\alpha_d} > 0\}. \tag{3.12}$$

This produces d-skeletons with elements that, when considered in isolation, have proper d-volume. That is, the embedded subgraphs do not span a lower-dimensional hyperplane due to rank deficiency, or on the contrary, contain too many vertices to be linearly independent given the ambient dimensionality m.

Now define a new map I based on intersection pruning such that any intersecting embedded cliques are removed from the skeleton. Rigorously, we define the map as follows for $d > 0$ and $d' < d$:

$$\begin{aligned} I \,:\, {K'}_d &\mapsto K^*_d \\ K^*_d &\equiv \sqcup_\alpha \alpha_d \,|\, \{\partial\alpha_d \in K^*_{d'} \,,\, \tilde{\alpha}_d \cap \tilde{\beta}_d = (\tilde{\gamma}_{d'} \vee \varnothing) \\ &\qquad\qquad \forall (\beta_d \neq \alpha_d) \in K'_d \,;\, \gamma_{d'} \in\ K'_{d'}\} \,, \end{aligned} \tag{3.13}$$

This map builds a quasi-convex simplicial complex out of the elements with volume, which is the most general simplicial complex that can be used with the definition of curvature that we require. In practice, I is a binary intersection test distributed over all cliques in a given skeleton with nonzero simplicial volume and uses fast and robust convex intersection algorithms. See Sec. 3.4.3 for details.

Given our suggestive notation, it should be apparent that each K^*_d, which we term a 'proper pruned skeleton,' along with the associated weights $\omega_{\alpha_d} \,\forall\, \alpha_d \in K^*_d$, make up precisely

the combinatorial data for the state ϕ_m that satisfies our set of constraints and embeddability requirements by construction, and can be used to form the structure we parameterized in Sec. 3.2.1.

We take the above sequence of maps to define the projection

$$\mu \,:\, \tilde{g}_m \mapsto \phi_m \,. \tag{3.14}$$

3.2.4 Embedding the Combinatorial Data

Just as $\mu(\tilde{g}_m) \mapsto \phi_m$, we can implicitly define a representative minimal embedding back from the combinatorial data into $\mathbb{R}^m$.

Out of the infinite family of embeddings that satisfy this property, let η_m be one representative fixed embedding in $\mathbb{R}^m$ such that

$$\phi_m = \mu \circ \eta_m \circ \phi_m \,. \tag{3.15}$$

We note that due to the noninjectivity of μ,

$$\eta_m(\phi_m) \neq \tilde{g}_m \tag{3.16}$$

in general, which is to say that μ is a left-inverse of η_m but μ itself does not have a uniquely defined inverse. Even after removing the vertex/root labels on both sides of the map, there are multiple states with different embedded intersection properties that can yield the same combinatorial data defining ϕ_m. However, for every pairing (g, χ_m) there exists a unique combinatorial state up to inherited gauge equivalence through μ.

For a discussion of some of the symmetries of this theory, see Sec. 3.9.1. An example of the equivalence classes under gauge that we are referring to would be those graphs equivalent up to isometry in the ambient embedding space, $\mathrm{ISO}(m)$, or up to vertex automorphism in their graph parameterization, $\mathrm{Aut}(g)$.

3.2.5 Physical Covering Space

We have constructed a map μ such that a combinatorial state ϕ_m can be parameterized by entirely by (g, χ_m).

A state $\tilde{g}_m$ lives in the unrestricted space of all possible embeddings of all possible graphs (of the type of graph/embedding pairing we consider). Denote this space $\tilde{G}'_m$. This space is dense in combinatorial states ϕ_m by construction under μ as a multi-cover into a combinatorial space we denote Ψ'_m. However, we are interested in the unique gauge-fixed equivalence classes of combinatorial states, the physical space Ψ_m.

Define the following quotient map as a projection onto the combinatorial gauge-fixed base space, identifying the multi-cover into unique equivalence classes:

$$Q \,:\, \Psi'_m/\!\sim \,\to \Psi_m \,. \tag{3.17}$$

We can formally define a pull-back of Q to the embedded space by using η_m such that the following diagram commutes:

$$\begin{array}{ccc} \tilde{G}'_m & \xrightarrow{\mu} & \Psi'_m \\ {\scriptstyle\exists}\big\downarrow{\scriptstyle\tilde{Q}} & & \big\downarrow{\scriptstyle Q} \\ \tilde{G}_m & \underset{\eta_m}{\overset{\mu}{\leftrightarrows}} & \Psi_m \end{array}$$

We note that no such gauge fixing is known to exist at the time of writing. As is often the case, we trade difficult to characterize rigid constraints in the combinatorial description for difficult to characterize inherited symmetries in the embedded description. Nevertheless, it is numerically easier to handle sampling redundancy than it is to sample the constrained space directly, and although computationally inefficient, we can tackle this issue with a well defined prescription.

3.2.6 Formal Path Integrals

In Sec. 3.9 we explicitly define the action $S(\phi_m)$ on the combinatorial space Ψ_m. Our action is decomposable into the combinatorial levels, and as a result, we can formally define a Euclidean path integral for our partition function as follows:

$$Z_m = \int \mathscr{D}\phi_m \, \exp \sum_{d=0}^{m} -S(K_d^*, \omega_{\alpha_d}) \tag{3.18}$$

Regarding numerical work, sampling the full space directly is difficult due to the constraints. Nevertheless, with the projection μ, we can now sample a proxy-space instead and be guaranteed to be sampling the entirely of our space of interest with the same action:

$$\tilde{Z}_m = \int \mathscr{D}\tilde{g}_m \, \exp\left(-S(\mu(g, \chi_m))\right) \tag{3.19}$$

We are not guaranteed, however, that a uniform sampling of $\tilde{G}'_m$ will have its distribution preserved under the map. Without further study, we cannot say that in the limit of a sufficiently well mixed Markov chain, the measure we intend to sample through a Metropolis filter on the embedding space is truly the stationary distribution we receive after we map to the combinatorial space, prohibiting a full quantum simulation of the combinatorial space of interest. An outstanding computation that would enable such a full sampling would be to demonstrate the convergence of the measures under μ such that

$$P[d_{TV}(\mathscr{D}\phi_m, \mu(\mathscr{D}\tilde{g}_m)) > \epsilon] < 1 - \delta \,, \tag{3.20}$$

for small parameters (ϵ, δ), uniform measures on the base spaces, and total variation distance between the measures d_{TV}. Such a proof is the object of current work.

Seeking the action minima, however, is entirely within our capabilities as they are trivially the same on both sides of the map, and a strongly driven optimization problem on the embedded side yields a combinatorial distribution highly peaked around classical states of interest. The majority of the following discussion will work in such a paradigm.

3.2.7 Boundaries

There exist special subsets of the states that are immutable in the state sum. These are deemed to be the state boundary, $\partial\tilde{g}_m$, wherein the embedded graph subset is unable to be altered in either its structure or embedding data, relative to the other vertices in the boundary. The combinatorial equivalent is given in terms of a minimal fixed K^* structure that cannot be altered (and induces a set of constraints on the weights at the nodes of that structure), plus an additional set of finite constraints on the weights associated with K_1^*.

In the embedded picture, a state boundary is characterized by its number of convex-hull disjoint path-components. That is, we can have a single closed boundary made of one path component, a 2-boundary system where the state sum is over bulk geometries between initial and final configurations, or a multi-boundary state given by n convex-hull disjoint components embedded in the same ambient space. Each component is assumed to have the same geometric realization structure encoded in the combinatorial equivalent, such that given a boundary component $B(g, \chi_m) \in \partial\tilde{g}_m$,

$$B(g, \chi_m)) \sim \eta_m \circ \mu(B(g, \chi_m)))\,, \tag{3.21}$$

where $\sim$ denotes equality under gauge. The initial embedding of the boundary data establishes the relative orientation of the substructures in the boundaries and any intrinsic length scales of the system, which are also represented in the set of combinatorial constraints. An example of a 2 path component boundary system initialization can be seen in Fig. 3.4.

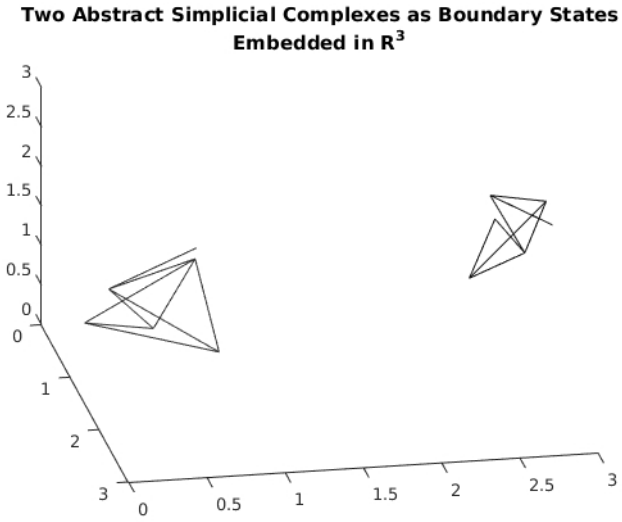

Figure 3.4: Example of an Initialized Boundary State

In addition to the protected nature of these boundaries under the Markov process, the intersection map I in Eq. 3.13 is also boundary preferential and is modified as follows:

$$K_d^* \equiv \sqcup_\alpha \alpha_d \begin{cases} \alpha_d \in \partial \tilde{g}_m \\ \partial \alpha_d \in K_{d'}^* \,,\; \tilde{\alpha}_d \cap \tilde{\beta}_d = (\tilde{\gamma}_{d'} \vee \varnothing) \,\forall \left\{ \alpha_d \notin \partial \tilde{g}_m ; (\beta_d \neq \alpha_d) \in K_d' \,;\; \gamma_{d'} \in \; K_{d'}' \right\}. \end{cases} \tag{3.13´}$$

In this way, our skeletal pruning is never destructive with respect to the boundaries.

3.3 Ambient Space

In order to probe emergent geometry, our discrete model must make contact with discretizations of manifolds. Although our model can be formally generalized to work with cellular decompositions of manifolds, we gain a robust computational toolkit with a restriction to convex/simplicial structures. With the simplicial approximation theorem in mind, we choose to work in a flat space and impose the geodesic embeddings of our graph edges in order to restrict to abstract simplicial complexes instead of abstract cellular complexes, without loss of generality for manifold approximation [31].

We avoid pathological flat ambient spaces, for if they cannot admit topologically 'reasonable' immersions of manifolds, then we have no hope to grow approximations to those structures. Lastly, we would like the ability to unambiguously define unique edge lengths without the use of an additional choice for periodically identified spaces, and we would like the full space available for an embedding as to avoid spaces with any singularities that could localize the graphs, establish extrinsic length scales, or otherwise impact the state geometry. As a result, we work in $\mathbb{R}^m$.

In the emergent network picture, we aim to explore the impact that the global embedding space has on stochastically grown networks between provided boundary states. From the combinatorial side, this is a restriction on the maximum number of levels m available in the combinatorial tree. Although we work at fixed embedding dimension, nothing in our construction is explicitly dependent on the ambient dimension—it is simply a constraint that can be taken to be infinite, or much larger than any intrinsic dimensionality of the boundary states. This control is important in the context of quantum gravity, as we would hope to allow for bulk states that may explore arbitrary dimensional configurations in the state sum. From a holography perspective, we can then ask questions like:

> Given a boundary state that is a triangulation of S^2 embedded in $\mathbb{R}^3$, is the optimal bulk state a triangulation of B^3 in the interior? If we embed in 4 or higher dimensions, does the high dimensional bulk data still lie in the vicinity of a much lower dimensional sub-triangulation?

The later opens up questions that breach the realm of probing the manifold learning hypothesis [21]. For computational purposes and to explore the effects of a finite embedding space on network growth with fixed boundary, we begin each investigation with the minimal embedding dimension that accommodates the boundary data in accordance with Eq. 3.21 and explore for asymptotic behavior in the large ambient limit.

3.4 Markov Process and Metropolis Algorithm

3.4.1 General Approach

Within the paradigm of optimization of the embedded networks, we now describe the finite horizon Markov process by which the network undergoes an evolutionary step. Although one could use a variety of optimization schemes, the nature of the space we sample lends itself nicely to an annealed Metropolis algorithm.

Broadly, the algorithm takes as an input the annealing parameters, embedded boundary states, and the free constants that are used to define the action. We then establish a random walk on the space of embedded graphs of the kind described in Sec. 3.2.2. After each step, we perform the projection described in Sec.3.2.3, evaluate the action to be used in the Metropolis filter, enact the annealed Metropolis accept/reject update, and after a finite horizon simulation, save the proposed classical state to disk. Due to the inherited symmetries of the projection, we must then postprocess our data to ensure our states are unique representatives of the combinatorial equivalence classes we aim to build our partition function with, which amounts to a numerical implementation of the map in Eq. 3.17. Finally, we can re-weight the data by the measure and compute relevant statistics. If one could guarantee a perfect optimizer, then this step would not be necessary as the only states saved to disk would be action-degenerate global minima, which we can use with a uniform measure for our observables. However, no optimizer is perfect, and re-weighting is necessary to further distance any sub-optimal minima. If the annealing is sufficiently slow, our saved samples should be localized to minimal neighborhoods in the action space, and the re-weighting will give some indication of the fluctuations about those minima, as opposed to a strict cutoff.

Due to the fact that we are performing an optimization as opposed to a full sampling, this algorithm lends itself nicely to massive parallelization with a multi-start heuristic. We furthermore do not have to worry about burn-in or autocorrelations at this stage. However, these concerns would most certainly need to be addressed when performing the full sampling through a nonannealed algorithm.

3.4.2 Random Walk

Let M_t be a set of available moves $m_i \in M_t$ indexed by i at step t in the evolution. The set of available moves have been chosen such that every move has an inverse, and is heuristically chosen such that the algorithm can freely sample across a large space of admissible states. We establish a minimal set of perturbations of g and χ_m that cover $\tilde{G}'_m$:

1. Nodal addition and subtraction

2. Edge addition and subtraction

3. Nodal perturbation in the ambient space

Under a finite number of the above moves, any bulk state $\tilde{g}_m$ can be accessed from any other bulk state $\tilde{g}'_m$, as can be easily seen through a deconstruct-reconstruct proof. Of course, the moves are restricted to respect the static boundaries and simplicity conditions imposed by our graph definition, as well as vertex injectivity. In practice, vertex injectivity is handled naturally by the machine precision of the embedding data, and simplicity is enforced by avoiding diagonal entries in the adjacency matrix of the graph parameterization. We also include more global moves to promote ergodicity and rapid mixing that alter both g and χ_m simultaneously, such as nodal splitting/recombining, edge splitting/recombining, and multiple simultaneous node additions/subtractions and edge additions/subtractions. See Fig. 3.5 for an example of such a nodal splitting/recombining move.

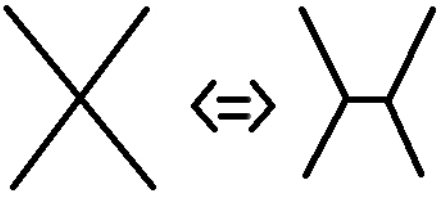

Figure 3.5: An Example Markov Move and its Inverse

In this way, our random walk is a kind of randomized Gibbs sampling, a subset of the Metropolis algorithms, due to any fixed subsets of the combinatorial representation under each iteration. Numerically, we handle the formally infinite ambient space and graph complexity using a bounding method: we restrict to an open ball of the ambient space that contains the boundaries and a maximal number of allowed bulk nodes, and perform simulations with progressively larger ambient volumes and allowed bulk nodes.

We take the Markov process to be a sequence $(g_1, \chi_m^1) \dots (g_n, \chi_m^n)$ of states where the maps from $(g_{i-1}, \chi_m^{i-1}) \mapsto (g_i, \chi_m^i)$ are the identity in the subspace untouched by the perturbation. Although we could select embeddings other than the identity that still preserve the full combinatorial data in the complementary subspace, we choose the identity for convenience. Picking such a particular embedding chain fixes some of the ambient gauge freedom.

Let p_t^i be the probability for performing move m_i:

$$p_t^i = \frac{1}{|M_t|} \forall\, i\,, \tag{3.22}$$

such that all moves that respect the state space have equal probability, and those moves that take the chain outside of the state space have zero probability.

3.4.3 Projection

The projection μ is accomplished by completing the various skeletal decompositions, volume computations, and intersection detections as outlined in Sec. 3.2.3. To form the clique complex, for example, every complete subgraph must be enumerated and stored. This amounts to an implementation of the clique problem, which is an NP-complete algorithm. Volume computations are then performed using Eq. 3.24a, and the set of cliques that do not satisfy the volume constraints are removed. The intersection detection on the remaining cliques are performed pairwise within the skeletons and use familiar algorithms from convex geometry such as solving a linear-programming problem on the convex hull of the Minkowki difference of the embedded simplexes being tested, or other specialized algorithms familiar to the computer graphics community for lower dimensional polytope intersection testing [4][48]. Once

we have the embedded descriptions of the proper pruned skeletons, we have all of the data necessary to compute the action.

3.4.4 Annealing and Acceptance

An annealing temperature $T_t \in \mathbb{R}^+$ and an annealing constant $\beta = (0, 1]$ are established at the start of an algorithm of annealed descent. As the simulation termination condition is a finite horizon corresponding to the completion of a finite number of steps, we set the annealing to be sensitive to the simulation horizon, $t_{max} \in \mathbb{N}$.

β controls how much of the simulation is in a deterministic decent regime with zero simulation temperature. We desire that large initial fluctuations allow for perturbations into a boundary-biased configuration, wherein thereafter the simulation begins to settle on a local branch minimum before it strictly descends to the optimal configuration of that branch. In this way we achieve the freeze-out sampling of minima of the state space to be used to build our desired ensemble as described above.

As is often the case with annealing algorithms, the precise annealing schedule and ideal annealing parameters are heuristically chosen as those that balance providing the deepest robust minima with fastest optimization times.

Each move is either accepted if the action is lowered and induces an update of the simulation variables, or conditionally accepted if the action increases, with rejections forcing a reversion of the state. This is accomplished with a conditional probability $\frac{\pi_{t+1}}{\pi_t}$ of the form

$$\frac{\pi_{t+1}}{\pi_t} = \exp \frac{-(S_{t+1} - S_t)}{T_t} \,. \tag{3.23}$$

where the action S_t is computed according to Eq. 3.28.

3.5 Combinatorial Gravity

Our goal is to understand the roll of gravity in emergent geometry from a combinatorial perspective, where our fundamental structures are as general as possible and we require the least amount of model assumptions based on anticipated macroscopic geometry. However,

our traditional notions of gravity are not well defined for a combinatorial framework. We have seen in Equations 2.7 and 2.8 the relationship between the Einstein Hilbert action and the Regge action for piecewise linear structures. We would like to understand what are the minimal prescriptions necessary to generate geometric structures that may resemble a triangulation discretization of an underlying space. To make contact with the nearest discrete gravitational formalism of Regge Calculus, we utilize combinatorial notions of volumes and curvatures that we can package in an effective combinatorial action. We do not have the rigid structures of even guaranteed simplicial complexes at our disposal, and as a result, we sought to carefully construct a 'network gravity' formalism that admits analogous structures in the appropriate limit, while maintaining agnosticism with respect to fundamental building blocks and attachment rules.

3.6 Proper Pruned Skeletons

In Sec. 3.2.3 we outlined explicitly the map from the embedded space to the combinatorial space, including the pruning and excision process that defined for us the K^* structure. From the embedded perspective alone, the states generically admit a large amount of geometric defects. This is a desired feature, for if the model aims to probe emergent discrete geometry at all scales, there should neither be constraints on the dimension of the building blocks nor their matings. Macroscopic consistency would only demand that in a regime where we expect general relativity to be applicable, the emergent description should be one that may approach a realized triangulation of an underlying manifold.

As we do not have a dimensional specification, we must allow for a description of a state that measures its near-triangulation structure at each simplicial level. Breaking down a generic embedded graph state into the K^*_d skeletons is precisely such a structure. Each skeleton alone is an embedded simplicial complex with geometric realization of all of its simplicial elements that can be used as a measure against a full triangulation, with the defects in the global state carried by the decomposition structure. The state is globally a superposition of abstract simplicial skeletons that each admit volumetric embeddings, where

the nongeometric data at each skeletal level only comes from lower-dimensional structures. For example as shown in Fig. 3.6, we may admit an embedding of a 2-simplex that has a 1-simplex in its interior, giving a 1-dimensional defect on the embedded 2-skeleton, but by construction there can be no nongeometric data of dimension 2 or higher paired with our 2-simplex.

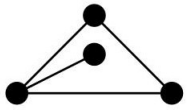

Figure 3.6: Admissible 1D Geometric Defect on a 2-Simplex Embedded in $\mathbb{R}^2$

Generic realizations that take abstract simplicial complexes to simplicial complexes do not have the embeddability and volume constraints that we impose [31]. We do not have the freedom to generically untangle the combinatorial network to force a geometric embedding of every element, or to find an embedding space of high enough dimension to admit a full realization, and instead turn to our in-place decomposition that admits a consistent graph structure for which we show that we can ascribe proper volumes and curvatures—essential tools for probing an effective gravitational action. For a simplicial structure, the K^* decomposition is the most general structure one could utilize that still meets the criterion necessary for the curvature and volume forms we employ.

3.7 Weightings

As mentioned, the weightings ω_{α_d} assigned to a state's complete subgraphs are based on the embedded simplicial volumes of those subgraphs. Our K^* structure guarantees that we can properly define a d-volume for each $(d+1)$-clique in bijection with a d-simplex.

3.7.1 Proper d-Skeleton Weights

K_1^* corresponds to the α-indexed list of 1-simplex edges in the embedded graph state. Each edge α_1 is then assigned a weight ω_{α_1} given by its L_2 coordinate length along the graph from the inherited metric of the ambient space.

This construction continues for all dimensional simplexes, with K_2^* associated with the disjoint union of 2-simplexes and weights ω_{α_2} given by their corresponding triangle areas, etc.

In general, the simplicial d-volume is given by the Cayley-Menger determinant, with the L_2 norm used to compute the edge lengths between the embedded nodes for each edge in the simplex [61]. We produce B_{α_d}, a symmetric off-diagonal matrix of squared edge lengths, by indexing over all embedded vertices $p_i \in \tilde{\alpha}_d$.

For $d > 0$:

$$\Omega(\tilde{\alpha}_d) = \sqrt{\frac{(-1)^{d+1}}{2^d d!^2} \det(\hat{B}_{\tilde{\alpha}_d})}\,; \tag{3.24a}$$

$$\hat{B}_{\tilde{\alpha}_d} = \begin{bmatrix} 0 & 1 & \cdots & 1 \\ 1 & & & \\ \vdots & & B_{\tilde{\alpha}_d} & \\ 1 & & & \end{bmatrix}, B_{\tilde{\alpha}_d} = \|p_i - p_j\|_2^2\,. \tag{3.24b}$$

Note that for $d > m$ or subgraphs spanning hyperplanes of dimension less than d, all ω_{α_d} will necessarily be zero as the coordinates cannot span the necessary vector space. We note that although the weights are derived from simplicial volumes, they are defined to be unitless. We simply take the magnitude of the simplicial volume as the combinatorial weight that respects the image of the volume map into $\mathbb{R}^+$.

3.7.2 0-Skeleton Weights

As the vertex set does not have any simplicial volume, we assign a single uniform weighting $\omega_{\alpha_0} \equiv \omega_0 \in \mathbb{R}^+$ to each node, as they are geometrically equivalent point objects. This marks the first free parameter of the theory, and its consequences will be discussed at length.

3.8 Curvatures

As we do not have a triangulation structure, we have no way of preassociating curvature to specific substructures, such as those found in the Regge case when employing deficit angles [47]. In this network formalism, we proceed with the intent that topological dimension itself is a true emergent observable and utilize a combinatorial curvature that generalizes to give a measure of discrete curvature over all simplicial scales.

3.8.1 Knill Curvature

An oft used curvature in network theory is the Knill curvature, defined for simple undirected networks g at a given node v by counting the number of complete subgraphs of order i attached to said node (here denoted $\#_v^i$) [67, 37].

$$R_v = \sum_{i=1}^{\infty} \frac{(-1)^{i+1}}{i} \#_v^i \,, \tag{3.25a}$$

$$\chi(g) = \sum_{v \in V} R_v \,. \tag{3.25b}$$

We see that when summed over the network, the Euler character is returned, which gives a discrete analog of the Gauss-Bonnet theorem for networks. We avoid using the Knill curvature for two reasons. Foremost, this curvature form is purely combinatorial and does not take into account relative weighting between complete graphs of different sizes. Although trivially diffeomorphism-invariant, this curvature is at odds with the notion of curvature we would like to associate with our model where intrinsic geometric data is accounted for. Secondly, while the Knill curvature as an Euler density appears similar to the Ricci curvature for 2 dimensions, this analogy clearly breaks down in higher dimensional Riemannian manifolds where the Ricci curvature is no longer a topological density. The Knill curvature is always measuring topological properties, and we seek a measure of curvature that is not strictly always an Euler density.

3.8.2 Forman Curvature

A combinatorial curvature associated with any cell of a quasi-convex cellular complex can be described by the dimensionless Forman scalar curvature derived from the Bochner-Weitzenbock decomposition of the combinatorial Laplace operator [23]. A regular CW complex is quasi-convex if for every pair of d-cells (α, α') and $(d-1)$-cell γ,

$$\gamma \subset (\bar{\alpha} \cap \bar{\alpha}') \Rightarrow (\bar{\alpha} \cap \bar{\alpha}') = \bar{\gamma}\,. \tag{3.26}$$

We note that a simplicial complex is a subset of this larger class, and that this scalar curvature can be applied to give a curvature measure on each $\alpha_d \in K_d^*$, as K^* satisfies quasi-convexity by construction with the map I in Eq. 3.13.

This definition of curvature is a weighted combinatorial curvature that depends on the near-nonlocal data of the $\alpha_{d\pm1}$ neighbors ($\alpha_d \subset \alpha_{d+1}$ or $\alpha_{d-1} \subset \alpha_d$) of the original simplex, and all of the associated weights. Formally, the list of weights is an arbitrary assignment into $\mathbb{R}^+$ inherited from an inner product on the cellular chain complex and can be provided by topological data, selected from some distribution, or set as a standard set of weights by taking them all to be unity. Here, we assert by model ansatz that the weights be precisely the embedded weights provided by the Ω map in Eq. 3.24a, which allows this measure of curvature to account for the relative sizes of the simplicial pieces, along with their connection data. Such an assignment was suggested by Forman as an approach to possibly connect the study of curvature on embedded combinatorial manifolds as cellular decompositions to their Riemannian analogues, imbuing the combinatorial structure with a sense of the intrinsic geometry of the cellular pieces [23].

For $d = 1$, the Forman curvature is strongly analogous in homological properties to the Riemannian Ricci curvature when the edges are considered as part of a cellular decomposition of a manifold, making them a good analog for gravitational curvature in this formalism. The higher curvature terms correspond to a generalization of the scalar curvature for the higher dimensional cells.

The Forman curvature is given as follows:

$$F(\alpha_d) = \omega_{\alpha_d} \left\{ \sum_{\alpha_{d+1} \supset \alpha_d} \frac{\omega_{\alpha_d}}{\omega_{\alpha_{d+1}}} + \sum_{\alpha_{d-1} \subset \alpha_d} \frac{\omega_{\alpha_{d-1}}}{\omega_{\alpha_d}} - \sum_{\tilde{\alpha}_d \neq \alpha_d} \left| \sum_{\substack{\alpha_{d+1} \supset \alpha_d \\ \alpha_{d+1} \supset \tilde{\alpha}_d}} \frac{\sqrt{\omega_{\alpha_d} \omega_{\tilde{\alpha}_d}}}{\omega_{\alpha_{d+1}}} - \sum_{\substack{\alpha_{d-1} \subset \alpha_d \\ \alpha_{d-1} \subset \tilde{\alpha}_d}} \frac{\omega_{\alpha_{d-1}}}{\sqrt{\omega_{\alpha_d} \omega_{\tilde{\alpha}_d}}} \right| \right\} . \tag{3.27}$$

We note that for a uniform point weight, $F(\alpha_0) = 0$. We also note that unlike the Riemannian case where there is no intrinsic curvature, nonzero Forman curvature can be ascribed to edges of a 1-dimensional triangulation. This is a known obstruction to having this curvature measure be more closely aligned with a smooth equivalent [23]. In our case, we can recover the right intrinsic curvature behavior in 1-D when the point volume is zero, however. This has led us to hypothesize that once the adjacency structure is set at a regulated value of ω_0, there may be a renormalization of the point volume back to the physical value that can be accomplished by an secondary annealing, holding K^* fixed. Investigations are forthcoming on this front.

3.9 Action

The action is an effective model based on the K_d^* slicing of the network. For each slicing, a Regge-like action is implemented, with the volume form given by the combinatorial map of the embedded simplicial weights, and the curvature form given by the Forman curvature. The action includes a sum over all possible proper pruned d-skeletons, and for a finite network, itself necessarily contains a finite number of terms.

$$S(\phi_m) = \sum_{d=0}^{m} \xi_d \sum_{\alpha_d \subset K_d^*} \omega_{\alpha_d} (F(\alpha_d) + \Lambda) \, . \tag{3.28}$$

Here, the ξ_d are coupling constants that differentially weight the slices of the network. These can be repackaged as a tower of coupling constants for each higher curvature term, similar to those found in a Lovelock theory of gravity where a sum over all Euler densities in d-dimensions constitutes the most general gravitational action [52]. There is no explicit constraint at this time that guides our couplings.

Uniform weighting over all d-skeletons occurs with $\xi_d = 1 \,\forall\, d$. This is the only the distribution we have found experimentally thus far that demonstrates the phenomenology we are interested in, and moreover, we suggest it is natural from a dimensionally agnostic perspective to avoid any dimensional bias of assigning nonuniform weights to the slices.

The cosmological constant term Λ is a dimensionless scalar offset to the Forman curvature representing a uniform background combinatorial curvature present over all skeletons. We will show at length the effect this term has on classical states.

3.9.1 Symmetries

In terms of inherited symmetries under μ from the embedded state, foremost the action is invariant under ISO(m). Additionally there is the group of symmetries that maintains the combinatorial weights and adjacency data but deforms the underlying coordinate space. This can be seen as a space of restricted diffeomorphism, where one can freely deform points (actively or passively) as long as edge lengths as measured from the induced metric on the ambient space are invariant between all *connected* nodes. An example would be the case of two 1-simplexes attached at a common node. Without changing the action, either end-node can be displaced by pivoting around the central node on some S^m with a radius of the embedded edge length (modulo degeneracy considerations). The same can be said for any structure with a higher dimensional 'pivot.' The number of free pivots characterize the continuous symmetry in the available ambient space and creates a large class of equivalent states under the action up to such coordinate displacements.

We also have symmetries of the graph state that are shared by the combinatorial state space alone. Writing down the state in an adjacency matrix sets an initial labeling, but we have vertex automorphisms AUT(g) that preserve the adjacency structure but permute the labels and give the same combinatorial data. More importantly, the combinatorial state is truly labeling independent. The number of weighted-cliques of a given order and how many neighbors they each have make up the data alone. A complete relabeling of the graph state can give the same data, and this symmetry is larger than just the vertex automorphisms.

3.10 Regulation

The action is intrinsically not positive-definite. As such, in the descent paradigm, the global minimum may be unbounded with network growth. Two of the free parameters we have introduced so far, the point volume and the cosmological term, act as regulators against such configurations.

3.10.1 Point Volume and Minimum Combinatorial Weight

As a simplicial volume, a natural choice from a geometric perspective may be to take $\omega_0 = 0$. However, the Forman curvature dictates that the weights must be strictly positive. If we were to force the situation of a zero point volume, we additionally find that there is an equivalence class of the action under the addition of disconnected points, where $\Delta S = 0$. This implies an identification between the absolute empty state and a state of infinite point density under the action.

While one solution to break this degeneracy would be to simply remove any disconnected points as 'nonparticipating' elements of the state, the geometric significance of a state that is infinitely dense with disconnected points is lost. Underneath the cover of points, a nontrivial network may have nonzero action due to the K_d^* slicing of the network. But in practice, there is no way to discern whether two points are connected in the infinitely dense sea, indicating that such an equivalence class is disfavored geometrically.

Pruning Modification

The presence of a positive definite point volume sets a minimum combinatorial length scale to the system. We assert that a combinatorial volume with $\omega_{\alpha_d} \leq \omega_0$ should not be able to be resolved, and require that our pruning procedure for determining geometric realization respect the point-volume as a lower combinatorial-volume bound. We modify Eq. 3.12 as follows:

$$K'_d \equiv \sqcup_\alpha \alpha_d \,|\, \{\, \omega_{\alpha_d} > \omega_0 \}. \tag{3.12´}$$

Analytical justification for this regulation is discussed in Sec. 3.10.3.

3.10.2 Cosmological Constant and Positive Definiteness

The cosmological constant term also gives rise to divergences with $\Lambda \leq 0$. Once we establish that $\omega_0 > 0$, it becomes immediate that $\Lambda < 0$ would also lead to a network evolution into a state that is infinitely dense in disconnected points and an action that is unbounded by below. Any trivial point addition would be admitted, with $\Delta S = -|\omega_0 \Lambda|$. For $\Lambda = 0$, disconnected point addition would cause again $\Delta S = 0$, as both curvature terms would be zero for the point volume contribution. We again argue as above that this is disallowed, and find that we are naturally restricted to $\Lambda > 0$ as a combinatorial regime that supports compact network growth. Alternatively, we can view the cosmological and point volume terms as regulators, wherein only positive-definite values can admit actions that may be bounded from below and split the point-degenerate equivalence classes of action.

3.10.3 Finite Probe Test for UV and IR Divergences

As a simple toy model to probe for bounded changes in the action under perturbations, we consider the addition of a single 1-simplex of weight ω_{1_1} with geometric attachment to an existing 1-simplex of weight ω_{2_1}. The fluctuation here is given by

$$\Delta S = \Lambda(\omega_0 + \omega_{1_1}) + 2\omega_0\omega_{1_1} - \frac{\omega_0(\omega_{2_1}^2 + \omega_{1_1}^2)}{\sqrt{\omega_{2_1}\omega_{1_1}}}\,. \tag{3.29}$$

In general, this expression has no definite sign.

UV

We can see that without the point volume regulator in the volumetric cutoff, a divergence to $-\infty$ would be present for an attachment of infinitesimal length, regardless of model parameters. With the cutoff, we forbid such a small length scale 'ultraviolet' divergence and

the change in action instead approaches the following:

$$\lim_{\omega_{1_1}\to\omega_0} \Delta S = 2\omega_0(\Lambda + \omega_0 - \frac{(\omega_{2_1}^2 + \omega_0^2)}{2\sqrt{\omega_{2_1}\omega_0}}) \,. \tag{3.30}$$

In the mutual limit that both $\omega_{(1,2)_1} \to \omega_0$, we see that we recover the action equivalent of the addition of two isolated points, which matches our geometric intuition as both the extent of the 1-simplex and the connectivity are combinatorially unresolvable from a point according to the weights.

All cases of vanishing simplex addition then yield finite changes in the action, with the sign dependent on the model parameters and simplex lengths.

IR

The limit

$$\lim_{\omega_{1_1}\to\infty} \Delta S \to -\infty \tag{3.31}$$

signals a large structure divergence in the 'infrared' regime of the theory. Regardless of model parameters, a large enough simplicial probe attached to a 1-simplex will always yield a negative change in the action, and unbounds the global minimum of the theory. Understanding the nature of this divergence is the issue of current work in the model, as any system can allow a temporary fluctuation to generate the existence of an isolated 1-simplex, and by sending an infinite 1-simplicial probe, will immediately drop the system to a global minimum of maximally extended polymer-like geometries regardless of the initial state configurations.

Bubble Divergences

This IR divergence is extremely similar in nature to naive bubble and spike divergences found in spinfoam theories of quantum gravity. As a largely simplified explanation, a trivially satisfied constraint equation on the allowed irreducible representation labels in a closed subgraph of the foam admits an unbounded sum over all possible labelings of edges by half-integer representations [7]. This causes an explicit divergence of terms in the partition

function. In such a case, a quantum-deformation of the gauge group can act to regulate the theory by restricting the number of good irreducible representations in the sum to a finite set and giving such a symmetry finite volume [64]. This deformation parameter is intrinsically tied to the existence of a positive definite cosmological constant.

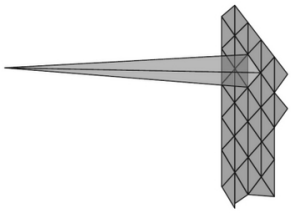

Figure 3.7: Cartoon Representation of a Spinfoam Spike Divergence [59]

Branching Universes

Even with a naive IR divergence uncontrolled, such a behavior does not entirely invalidate the formalism. As the network evolution is accomplished by a series of finite Markov moves, we can simply restrict to a set of local moves that, on average, prevent such a divergence from materializing in practice. We examine instead for minima that, divergent moves unconsidered, act as meta-stable optimization points in topology that can then be perturbed in volume to understand the local stability of the configuration. This is similar to the CDT handling of branching universes that would otherwise cause divergences in the state sum [2]. The tendency for an infinite simiplicial probe may be interpreted as the emergence of a branching universe, where localized boundaries give rise to the birth of new geometry grown extremely nonlocally. Seeing the same sort of divergence here may indicate that emergent geometry at the simplicial scale alone has such a property before we ever even consider a large geometry limit.

The causes of such divergences in a CDT have roots in Regge calculus, where residual diffeomorphism symmetry in the bulk manifests as unconstrained translations of triangulation vertices [24]. Here, without contact to diffeomorphisms through even discretized manifolds,

we still see such a divergence. Understanding our divergence as a possible manifestation of a kind of 'combinatorial diffeomorphism' is underway.

Nevertheless, unlike the typical characteristic of traditional Euclidean emergent geometry where the tension between the entropy of the state configuration plays against the unboundedness of the action to see a sharp phase change between either a crumpled or maximally extended state, we show that there exists tunable parameter regions where stable compact extended geometries can be still achieved as classical saddles [3].

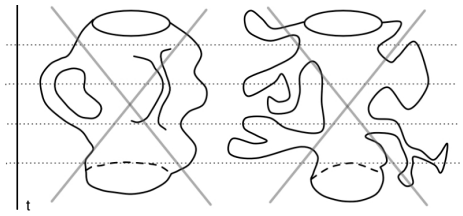

Figure 3.8: Cartoon Representation of Branching Universes in a CDT [42]

Λ *and Diffeomorphism Symmetry*

As mentioned, many of the naive infrared divergences in discrete emergent geometry models can be seen not as sicknesses, but as manifestations of residual diffeomorphisms on the vertices of a fixed triangulation. This gauge volume can be rendered finite by the existence of a positive cosmological term.

In a CDT, having a positive cosmological term corresponds to a maximum length scale through volume constraints. The topology is fixed to $S^3 \times S^1$, and as each slice of the triangulation is constrained to be a triangulation of S^3, the bare cosmological constant is, on-shell, directly translated to the compact volume of the space as they are conjugate in the discretized action [3]. There are only two volumes of 4-simplexes used in a 4-D CDT, and as an average 4-volume of a simplex can be defined and related to the 4-volume of the universe being simulated, the fixed topology gives a convenient bound on the maximum number of 4-simplexes through the action. As such, CDT's are simulated at fixed spacetime volume and

fixed topology, and the sampling is constrained to sampling over triangulations with different reaches and volume *distributions* (although an inverse Laplace transform can be used to relate the partition function to the variable volume case [1]). For a 3d spin foam formulation where the representation labels on the spin network edges correspond roughly to geometric edge lengths, the q-deformation cutoff can be reinterpreted geometrically proportionally to the finite maximum geodesic distance on a corresponding sphere of the same constant positive curvature [24]. Therefore, the gauge volume of residual diffeomorphisms as translations of spin network vertices giving an IR divergence is now finite. The symmetry is still present, but it at least has finite gauge volume that can be handled analytically.

In the network gravity formalism, we introduced a cosmological constant as a combinatorial offset strictly as a regular on the number of disconnected components. We witness a naive IR divergence in our model that is not naturally regulated by mere existence of the cosmological term. It is not universally true for Euclidean geometries that simply because one includes a positive cosmological term, there exists a maximal length scale. Only on-shell can we relate Λ and R directly through the Einstein equations, and the local nature of these equations prevents us from making claims about any global structure like total volume. Moreover, for the combinatorial action, we have yet to solve the equations of motion in closed form. Although there may be a way to interpret and regulate the divergence in the combinatorial model, without additional structure to understand the effect of a combinatorial cosmological term, such efforts may be independent of Λ.

At present, our simulation heuristics demonstrate that the intrinsic scales of the boundary set the locality regulator for our optimization. If the simulation is allowed to probe scales much larger than the boundary scales, any structure in the boundaries is dwarfed by the globally unconstrained behavior of a free combinatorial-bulk. If the simulation is allowed to perturb within a compact region of the ambient space localized to the boundary scales, the simulation respects the boundary geometry and finds bounded minima. Understanding the nature of this relationship is at the heart of ongoing work.

3.11 Simulation Results

We restrict our discussion to the case when the coupling constants ξ_i are all unity.

3.11.1 1-D Simulations and Cosmological Constant Driven Phase Transitions

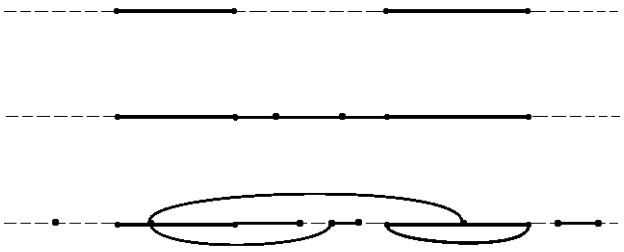

Figure 3.9: From top to bottom, we illustrate the 1-D boundary setup; show an example geometric solution with simplicial attachments; and give an example abstract solution with nonsimplicial attachments (shown with curved lines for illustrating overlap)

A 1-dimensional embedding space is the simplest abstract network situation in which we can anticipate a classical state due to the restricted types of building blocks and attachments. Consider two closed disjoint intervals of the real line. Triangulate each interval with a single 1-simplex with 0-simplex boundaries. These networks can represent a 2-boundary state that we would like to investigate.

A classical bulk network that connects these disjoint boundaries and represents a triangulation of an underlying manifold would be a series of 1-simplexes that connect the two segments in an embedded simplicial complex with nonoverlapping simplicial volumes. However, in the space of embedded abstract simplicial complexes, we may admit isolated point additions (both overlapping edges or disjoint), and 1-simplex additions as disjoint, point-connected, overlapping, or doubly-point connected. The situation is illustrated in Fig. 3.9.

Example optimal states for uniform coupling and positive point volume are shown in Figs. 3.10, 3.11, and 3.12. We see that for negative cosmological constant the system begins to fill all available space with nodes. This echoes our earlier analysis of evolution in the presence of a nonpositive cosmological constant. For a positive cosmological term with a value less than a particular critical value Λ_c, the simulation demonstrates a geometric complex solution we would anticipate as a minima of the action, with fully realized skeletons. Lastly, when probing the system for $\Lambda > \Lambda_c$, we see that no realizable network is favored to grow as the system began in its global minimum. The system is perturbed into a highly connected state, but as keeping or removing intersecting geometries are equivalent under this parameter set, we are left with an over-connected graph state on the original set of nodes. The critical value Λ_c was found through numerical investigation, and does not yet have an analytical justification; nevertheless, Λ acts as a clear parameter for controlling the phases between very different states of stochastic network growth, focused on either the network connectivity or abundance of structural elements. This indicates the importance of the cosmological term as a regulator of nondegenerate state growth with respect to fixed boundaries.

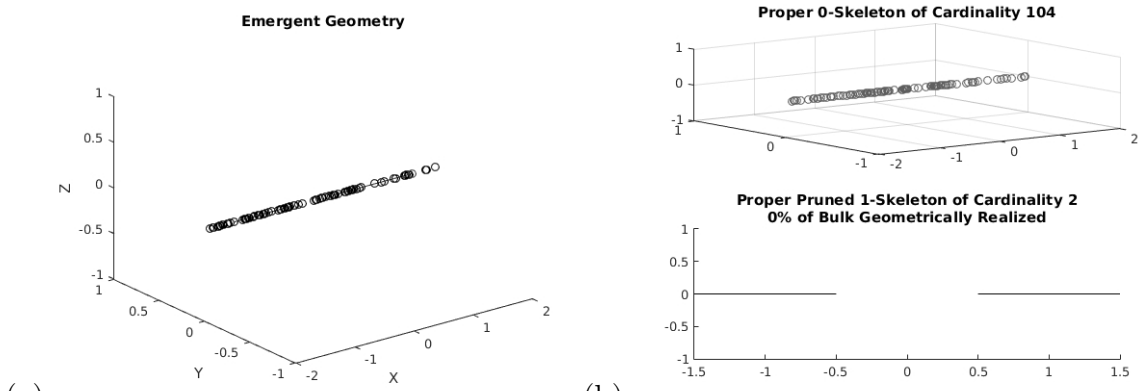

(a) (b)

Figure 3.10: $\Lambda < 0$ Optimal State (a) and K^* Decomposition (b).

The network growth fills all available space with nodes and does not produce fully geometrically realized images, with isolated nodes and overlaps in edges.

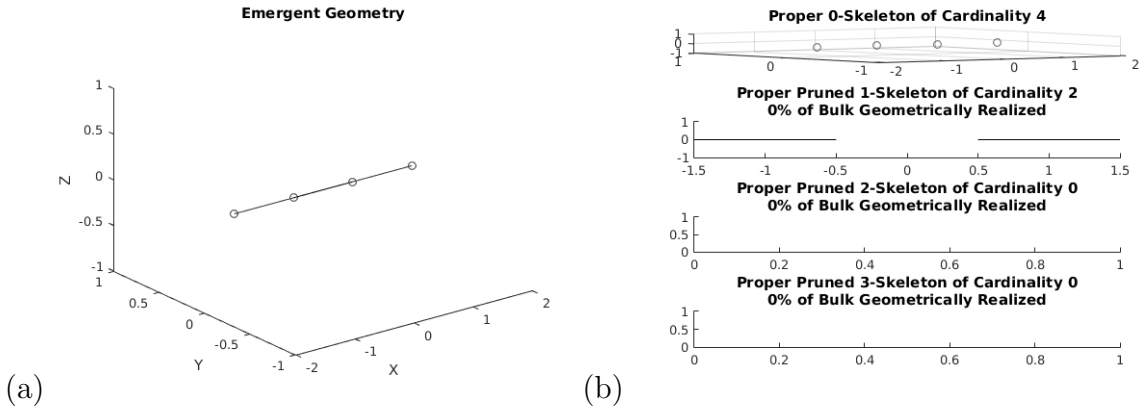

(a) (b)

Figure 3.11: $\Lambda > \Lambda_c$ Optimal State (a) and K^* Decomposition (b).

We see that no geometric network emerges—the action began in its global minimum with the boundary configuration, and lateral translations into degenerate configurations induce an over-connected graph state.

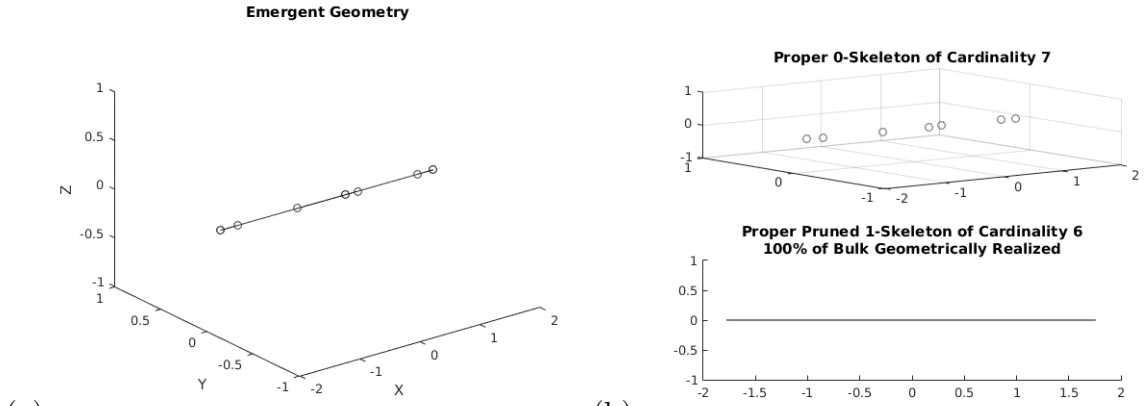

(a) (b)

Figure 3.12: $0 < \Lambda < \Lambda_c$ Optimal State (a) and K^* Decomposition (b).

We see the minimum in the action appears with the emergence of simplicial attachments that have proper geometric embeddings admitting a perfect skeletal decomposition that lacks any unrealized or disconnected geometries.

3.11.2 Higher Dimensional Simulations

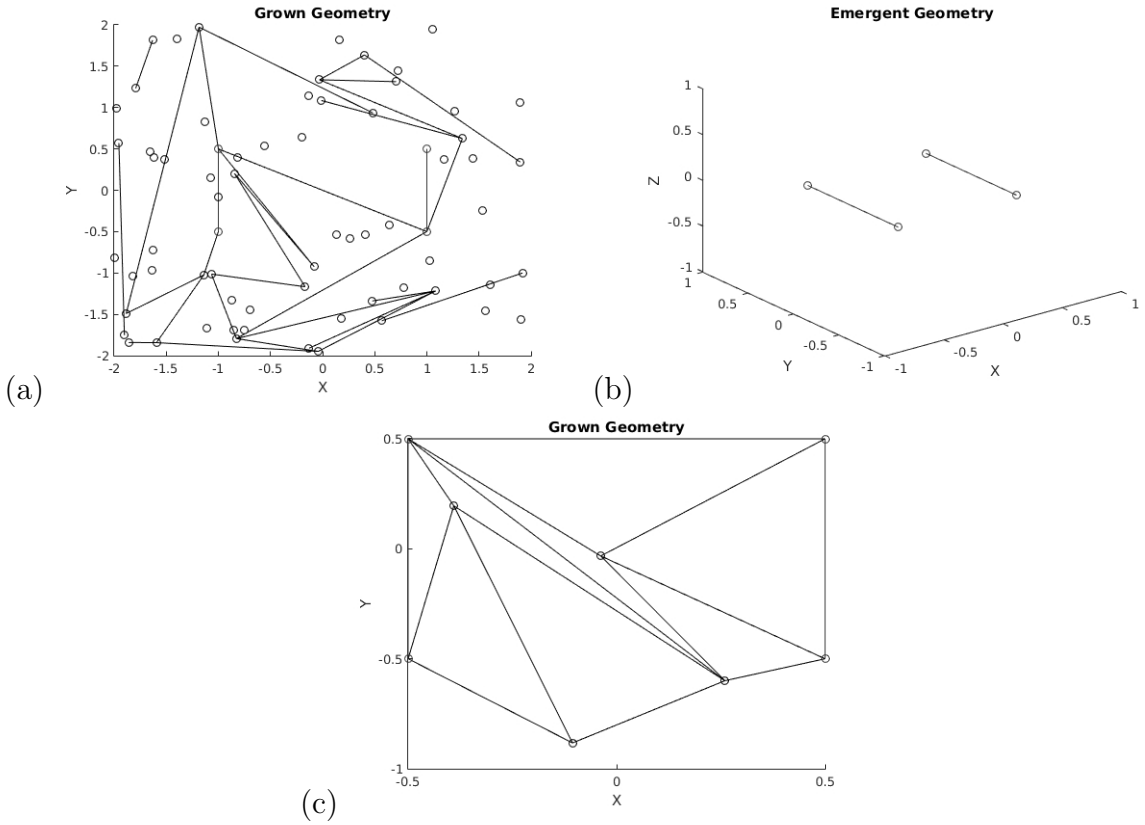

(a) (b) (c)

Figure 3.13: Geometry Restricted to $\mathbb{R}^2$ with Boundary States of Two Finite 1-Simplexes

In Fig. 3.13 we see the characteristic phases of negative (a) or super-critical (b) cosmological growth, with either chaotic elements with disconnected regions or no network growth at all, respectively; in c), we see realized growth for the geometric cosmological range, forming a completely realized 2-triangulation of some finite strip.

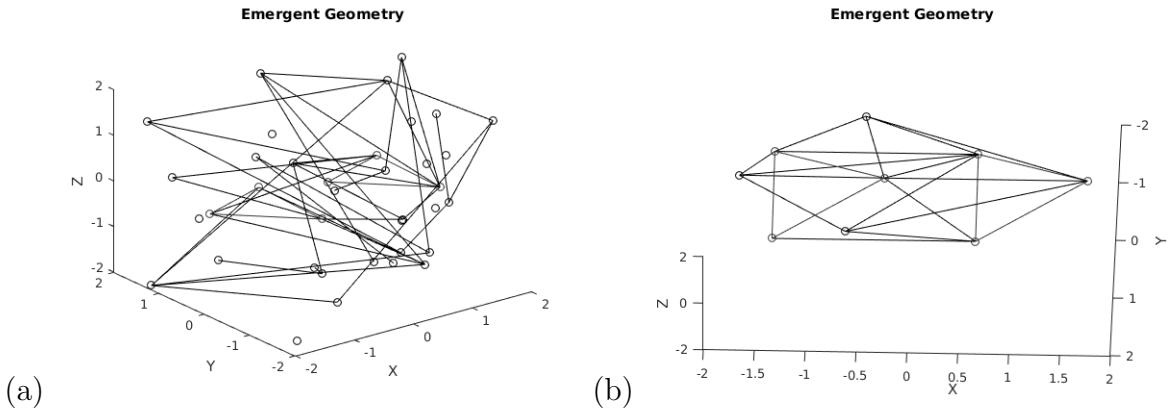

(a) (b)

Figure 3.14: Identical 2-Simplex Boundaries and their Network Growth for Negative (a) and Geometric Cosmological Parameters (b) in $\mathbb{R}^3$

Fig. 3.14 clearly shows the disconnected and disordered network of the negative cosmological simulation starkly contrasting with the positive-subcritical simulation.

Although the presented simulation results do not yet provide detailed statistics, these examples do demonstrate that the action and growth procedure are capable of investigating the emergence of realized geometries without preassigning attachment rules or dimensional assumptions. In the generic space of abstract simplicial complexes, it is a highly nontrivial goal to find a phase of stochastic growth with geometric realization and compact yet voluminous extent. Although there is certainly further work to be done, that the model can naturally demonstrate precisely such a phase, and even generate genuine partial triangulations as classical minima, is strongly encouraging as a base framework. Systematic investigation into geometric phases is underway.

3.12 Additional Model Properties

3.12.1 Action-Flat Network Dynamics

We restrict ourselves now to the case of model interest, where $(\omega_0, \Lambda) > 0$.

In this regime, we ask whether there are equivalence classes under the action for various states. To begin our analysis and simplify the investigation, we restrict to first probe independent regular simplicial building blocks. This provides us with a 3-dimensional configuration space of variables: ω_0, Λ, and ω denoting the uniform edge length.

We can now easily generalize to the case of an arbitrary regular n-simplex of side-length ω, and find the action in closed form:

$$\begin{aligned}
\omega_d &= \frac{\omega^d}{d!}\sqrt{\frac{d+1}{2^d}}(1+\delta_0^d(\omega_0-1)) \qquad (3.32)\\
S_n &= \sum_{d=0}^{n}\binom{n+1}{d+1}\omega_d\left\{\Lambda+(1-\delta_0^d)\right.\\
&\times\ \omega_d\left((n-d)\frac{\omega_d}{\omega_{d+1}}+(d+1)\frac{\omega_{d-1}}{\omega_d}\right.\\
&-\ \left.\left.((n-d)\binom{d+1}{d})\Theta(n-d-1)|\frac{\omega_d}{\omega_{d+1}}-\frac{\omega_{d-1}}{\omega_d}|\right)\right\}
\end{aligned}$$

Here, the $\delta^{\cdot}_{\cdot}$ is the Kronecker delta, and $\Theta(\cdot)$ is the Heaviside function with the imposition that $\Theta(0) = 1$.

We study the level-sets of this function, solving for the roots of this action as an example. We see that for progressively higher n simplexes, the solution space has larger forbidden regions in the parameter space, and even discontinuous regions, but nevertheless the space of solutions does not appear to become discrete or vanish.

2-Simplex The regular 1-simplex action has a single isolated point as level sets and is uninteresting. We look toward the 2-simplex action, which takes the more complicated

form:

$$\begin{aligned} S &= 3\omega_0\Lambda + \frac{\sqrt{3}}{4}\omega^2(3\omega + \Lambda) \\ &+ \omega(4\sqrt{3} + 6\omega_0 + 3\Lambda - 2\omega|\frac{4\sqrt{3} - 3\omega_0}{\omega}|)\,. \end{aligned} \tag{3.33}$$

We can see in Fig. 3.15 that there does exist a solution set for $S = 0$ and $\Lambda > 0$ (this plot extends to both $\pm\Lambda$ in the interest in seeing the structure). Thus, certain values of cosmological and point volume terms admit the spontaneous emergence of 2-simplexes for even a purely classical action descent. Furthermore, we see that ω appears cubically in the above equation, allowing for the possibility of a multivalued solution. This indicates that a spontaneous transition between regular 2-simplexes of varying size is admitted by the action as well, for particular regions of the free parameter space.

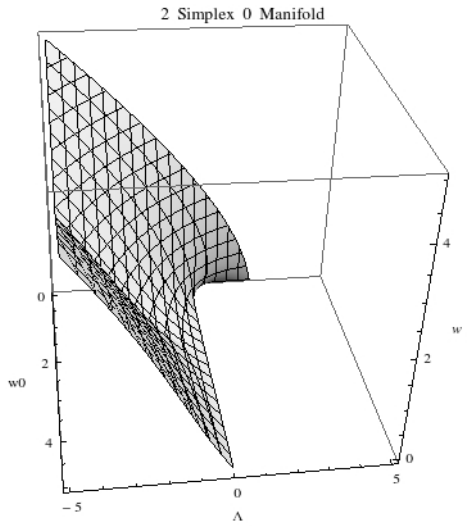

Figure 3.15: $S = 0$ manifold as a function of $(\omega, \omega_0, \Lambda)$ for an isolated 2-simplex, with the first indications of multi-valued behavior in ω for fixed model parameters

n-Simplex We have continued to probe higher regular simplex structures for their flat manifolds with respect to the configuration space, and can report a similar behavior.

We provide an example in Fig. 3.16 of a regular 20-simplex $S = 0$ manifold for evidence of multivalued behavior for some parameter regimes, as well as large regions where there is clearly no such degenerate behavior.

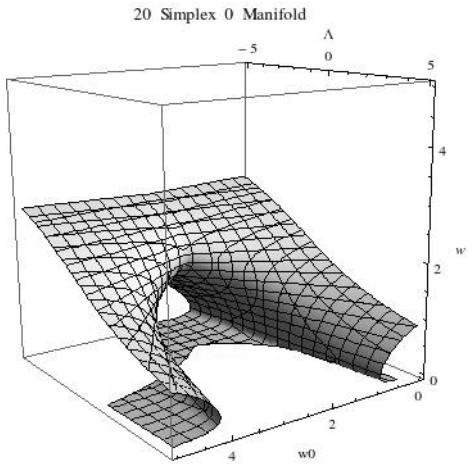

Figure 3.16: $S = 0$ manifold as a function of $(\omega, \omega_0, \Lambda)$ for an isolated 20-simplex, clearly showing a rich parameter space of multivalued solutions

The existence of these manifolds suggests equivalence classes of networks under the action, where the network dynamics may translate laterally along these flat directions before jumping into a new region of the state space. The states themselves are currently treated as distinct elements in the state space. However, for the purposes of numerical simulation, the possibility for a network to deform along a flat parameter manifold before jumping into a state with a radically different action compared to the primary state introduces a new level of complexity. The system can be prone to large fluctuations in the action, and sampling efficiently can be difficult with nonisolated degeneracies and potential domain walls.

It should be noted that, for a given simulation, the parameters of ω_0 and Λ are nondynamical. We also clearly do not expect only regular isolated simplexes to constitute the states,

and it may be the immense symmetry of these special states that admits these transitions. Nevertheless, it is still unknown whether the properties seen in this restricted numerical investigation will be present in the general state case, or whether the flat manifold degeneracies are split into a sufficiently discrete space upon breaking the symmetries.

The proof of existence and study of behavior of action-degenerate general networks is underway.

3.12.2 Refinement and a Classical Limit

Refining and coarse graining for topological triangulations are often used to achieve macroscopic results, and in the context of simplicial gravity, even macroscopic time evolution may be understood as refinement [19]. For our construction, however, there is no sense in which we can explicitly take the number of simplexes to be very large or edge lengths to become small, given a fixed boundary. The states are distinguished by the number of simplicies and their geometric embeddings, so refining generated by ambient diffeomorphisms which displace nodes on top of another (or their inverse) to reduce (increase) the number of nodal degrees of freedom are not purely gauge equivalent descriptions of the same triangulations. Especially since we are probing structures that may not be related to triangulations in the far nonclassical limit, we cannot use any assumptions applied from traditional discretizations.

Therefore, we do not look to this model to necessarily generate a macroscopically smooth structure at any scale, but to understand the emergence of microgeometry and its defects. The states in this theory should not be taken to be complete geometries that can describe a universe, for example. Instead, they are local patches. This is immediately evident from the simplicial closure constraints, which are flat. In a fixed flat ambient space of dimension d, any d-dimensional triangulation that may emerge as a classical state is necessarily a flat patch given our embedding restrictions. States that have extrinsic curvature from their embeddings in a higher dimensional space are admitted, and states that span lower dimensional subspaces can have intrinsic curvature based on deficit angles that one may compute from a new triangulation imposed globally over the state (for example, a state that looks like a sphere

can have a triangulation with nontrivial deficit angles mapped onto it), but such global structure should only be taken as indicators of topological observables, not geometric. A classical state in this restricted model should be the emergence of what may be a local tangent space to a global geometry.

With this in mind, we can achieve a local refinement by exploiting the property demonstrated in Sec. 3.12.1 by translating laterally in action-space through refined configurations. An example of a transform that could generate such an orbit through the configuration space would be a conformal rescaling followed by barycentric subdivision (BSD). Unlike a triangulation where Pachner moves can be used to admit refinements or coarsening limits, due to our intersection pruning, such moves would not grant us a refining limit. For example, the $1-3$ Pachner move on a 2-simplex would actually result in no 2-simplexes under μ due to the outer triangle containing the inner triangles. This exemplifies the meaning of the pruning in our state space, and interplay between the adjacency structure and possible geometric realization. The $1-3$ Pachner move in 2-dimensions creates the adjacency structure of a flat tetrahedon. Our model selects against such degenerate geometries by enforcing that if such a structure is to exist, it either must be realized in a higher dimensional space or none of the surfaces exist due to their embedding conflict, and the only structure that is admissible is the 1-skeleton. Applying a Pachner move such as this would be further inappropriate for our model, as they operate on fixed dimensional simplicies whereas our model should be dimension agnostic.

A complete barycentric subdivision, however, provides the right nodal structure to be nondestructive under μ up to the minimal length scale, provided the initial state is geometric, as geometric realization is preserved under BSD [31]. It consists of adding a new node at the barycenter of each simplex in the complex regardless of dimension, and re-connecting the structure based on the original simplicial containment data. See Fig. 3.17 for an illustration of this procedure.

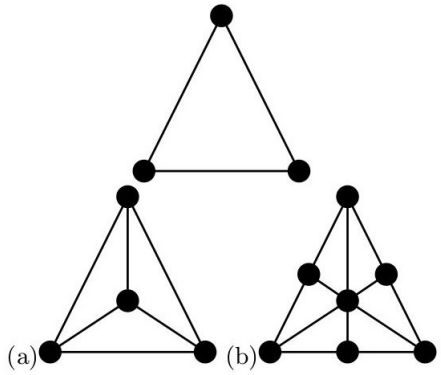

Figure 3.17: Refinement Example Under $1-3$ Pachner Move (a) vs Barycentric Subdivision (b)

Preliminary results suggest that a barycentric subdivision almost surely decreases the action for physical states. Without the point-volume UV cutoff, this would unbound the action from below and the classical minima would be any nonempty state under infinite barycentric subdivision, emphasizing the role of the point-volume as a UV cutoff again. The minimal volumes also highlight the need for the conformal dilations to ensure the constraint is satisfied. We conjecture that provided a state that is a global minima of the action (or at least a sufficiently well separated local minima), this refinement process of a global conformal dilation followed by a uniform barycentric subdivision can maintain such a solution as a stable fixed point, and in this way, generate a progressively larger selfsimilar structure. As a result, we can induce a kind of renormalization of the combinatorial scale in the bulk (which is only set by the point volume) through such a process.

This also invites the possibility to understand time evolution as flow along the orbit generated by the transformation. Each transform gives a discrete timestep, where a granular affine parameter indicating the number of transforms plays the roll of a granular time. In this picture, our notion of time has a global directionality due to the fact that there are only a finite number of inverse BSDs allowed until a kernal geometric state is reached, but locally we can translate freely backward and forward. To make this concept rigorous, we would

need to classify this type of transform as playing the roll of 'combinatorial diffeomorphisms,' giving a dynamical notion to the emergence of large classical spaces from the local kernal patches. Imposing such a symmetry would require delicate handling of the state sum and a new gauge fixing, as in current implementations such orbits are considered inequivalent states.

3.12.3 Observables

Other than the statistics of the Forman curvatures and weights over the skeletal structures, additional observables that can be considered are either purely topological or reference global properties. For example, $|K_d^*|$ or the number of path components π_0 can be calculated. An understanding of when a particular abstract complex is 'approaching' a geometric complex can be gained from these observables. One method to measure this limit is to consider whether a particular complex can be reduced to a fully realized complex (even of uniform building blocks in the sense of a triangulation) in a finite number of additional pruning moves.

Of particular interest is the emergent dimensionality of the state, grown under various conditions (valence or embedding dimension restrictions), between various boundaries. One measure of dimension we aim to employ is the spectral dimension, mentioned in Eq. 2.9. We can also compute the Euler character to gain insight into the topology statistics.

Taking the space of optimal embedded graphs as an ensemble itself, we can compute a different set of observables that can rely on local embedding data, such as the percentage of geometrically realized simplexes of a given order. These observables and the space of optimal graphs are interesting in their own right independent of the combinatorial space, as they have a more dense space of intersecting geometries to study and have an explicitly fully broken diffeomorphism symmetry, allowing us to probe observables such as Hausdorff dimensions averaged over ensemble embeddings.

3.13 Discussion

The study of emergent complex networks is a largely active field in which a variety of network growth paradigms are investigated for behavior that can be mapped onto physical problems of interest *a posteriori*. Rules that govern network growth in a given model are often selected without a motivating principle, as it is difficult to gain a thorough understanding of the emergent properties of the model without fully running the stochastic growth.

We have presented an emergent network formalism with strong analytic handles that can be used to investigate the nature of network interactions and probe emergent geometry considerations as mapped onto a combinatorial state space of interest. In building a gravitationally motivated model to study outstanding questions in simplicial emergent geometry, we allowed for a stochastic Markov process to generate a bulk network state between fixed boundary configurations, sampling for the stable minima of the semi-classical state space through an annealed Metropolis algorithm in order to probe our combinatorial measure. The metric against which we evaluated the network growth is an action principle in the space of abstract simplicial complexes, utilizing a decomposition of the embedded state into a superposition of proper skeletons consisting of geometrically realizable simplexes with nonempty simplicial volumes. Using the Forman cellular curvature with combinatorial weights provided by simplicial volumes, we showed that a Regge-like network action demonstrates distinct phases of stochastic geometric growth driven by the cosmological constant without preassigning the dimension of the simplicial building blocks, attachment rules, or dedicated embedding dimension. With fewer constraints imposed by hand, we connected the qualitative behavior of the model to existing frameworks for emergent geometry and aspects of discrete quantum gravity, and illustrated numerical and analytic justifications for a positive-definite cosmological constant and minimum combinatorial length scale.

Upcoming work aims to answer some of the many questions this construction poses, and begin to systematically compute observables for a wide variety of configurations in addition to demonstrating analytical proofs for the tractable sectors of the combinatorial space.

We would lastly like to mention that in addition to studying geometric embeddings from combinatorial structures, this formalism may be able to be used to model a variety of other types of network dynamics. For example, a study of optimal social networks, neural networks, or networks related to commerce can be mapped onto this formalism.

There is a rich landscape to study, and the framework presents a numerical 'petri-dish' of emergent combinatorial geometry to probe.

Chapter 4

EXACT PROBES IN THE NETWORK GRAVITY MODEL

4.1 Introduction

One of the primary open questions of our model lies within the full combinatorial state space. Can we find a way of probing this space directly, and if so, what can be learned about the full partition function? Will our results from the semi-classical ensembles be stable under perturbations and with respect to the entropic multiplicities of the full state space at finite temperature, and furthermore, can we open channels to studying other regimes of the state space? To address these questions, we will illustrate some particular regimes of the theory that admit direct numerical simulation in the combinatorial space without the use of the covering space. There, we will study the vacuum fluctuations and attempt to gather insight into the other regions of the space through a study of the state sum and topological observables. An additional advancement presented is the characterization of two distinct pseudo-metrics on the space of states, which we introduce in order to characterize fluctuations and autocorrelations.

We make special note of the additional model constraint imposed in the original construction: that if the combinatorial structure admits a simplex of a certain volume and this object is embeddable, then such a simplex is forced to be present in the state—the minimal "If it can exist, it does" assumption. This implies that the states can be entirely characterized by an adjacency matrix and an embedding map, as (if all simplexes can be embedded) the topological nature is encoded directly in the edge skeleton. This is the key assumption that allowed us to create the covering space in which we sampled our classical states. However, for a fixed number of roots n, sampling the space of all abstract simplicial complexes C_n, weights excluded, is a larger combinatorial space where higher dimensional simplexes may or

may not be included based on the edge data regardless of embedding properties. Considering such a space would be an enlargement of our original state space, and exploring such a space may provide indications as to the necessity of this restraint. In the phases we present with the following probes, we consider both the original state space and the enlarged version as they are equally samplable in the limits we examine.

4.2 Metrics on the Combinatorial Space

Foremost, in order to have an additional handle to measure the autocorrelations and fluctuations of the samples and observables on our state space when performing our Metropolis algorithm, we introduce two independent metrics: one as an induced pseudo-metric from the action through a 'Reproducing Kernel Hilbert Space' (RKHS), and the other is a pseudo-metric directly on the combinatorial space itself. These metrics provide new tools for measuring distances in the state space and allow us to better characterize our sampler.

We recall for completeness the definition of a metric $d(\phi', \phi'')$ on a set Ψ for all $\phi', \phi'' \in \Psi$.

$$\begin{aligned} \Psi \times \Psi &\rightarrow [0, \infty) \\ d(\phi', \phi'') &\mapsto r \end{aligned} \tag{4.1}$$

such that d has the following properties

1. d is symmetric

2. d is positive definite

3. d satisfies a triangle inequality $d(\phi', \phi''') \leq d(\phi', \phi'') + d(\phi'', \phi''')$

4. d satisfies the identity of indiscernables $d(\phi', \phi'') = 0 \Leftrightarrow \phi' = \phi''$

For our purposes, we desire that the metric measure differences in both the weightings on each combinatorial node and the differences in the combinatorial structure itself. It should be uniformly sensitive to all combinatorial levels, and insensitive to combinatorial gauge.

4.2.1 Induced Metric Through a RKHS

Let Ψ be any nonempty set of interest. A symmetric function $K : \Psi \times \Psi \to \mathbb{R}$ is a positive definite kernal on Ψ if

$$\sum_{i,j=1}^{n} c_i c_j K(\phi_i, \phi_j) \geq 0 \quad \forall \quad n \in \mathbb{N}, \phi_i \in \Psi, c_i \in \mathbb{R} \tag{4.2}$$

Let $K_\phi = K(\phi, \cdot)$ be a symmetric positive-definite kernal, and define H_0 to be its linear span for all combinatorial states $\phi \in \Psi$. Define an inner product on this function space by

$$\langle \sum_{j=1}^{n} b_j K_{\phi'_j}, \sum_{i=1}^{m} a_i K_{\phi_i} \rangle = \sum_{i=1}^{m} \sum_{j=1}^{n} a_i b_j K(\phi'_j, \phi_i) \,|\, (n, m) \in \mathbb{Z}^+, (a_i, b_j) \in \mathbb{R} \tag{4.3}$$

Let H be the completion of H_0 with respect to the inner product such that

$$f \in H \Leftrightarrow f(\phi) = \{ \sum_{i=1}^{\infty} a_i K_{\phi'_i}(\phi) \,|\, \sum_{i=1}^{\infty} a_i^2 K(\phi'_i, \phi'_i) < \infty \quad \forall \quad (\phi, \phi') \in \Psi_n \} \tag{4.4}$$

H is the unique RKHS associated with the kernal and the set, and an inner product on the set can be naturally induced by the inner product on H [10].

In our case, it is natural to chose the Gibbs measure as the kernal with a symmetrizing modification. This is known as the Abel kernal, and is given as

$$K(x, y) = e^{-\alpha |x-y|} \,|\, (x, y) \in \mathbb{R}\,,\, \alpha > 0 \tag{4.5}$$

For our case, we take $x = S(\phi)$, $y = S(\phi')$, and $\alpha = \frac{1}{T}$, $T > 0$. This provides an inner product on our combinatorial space as

$$\langle \phi, \phi' \rangle = K(\phi, \phi') = e^{\frac{-|S(\phi) - S(\phi')|}{T}} \tag{4.6}$$

Note, K is naturally normalized such that $\langle \phi, \phi \rangle = 1 \, \forall \, \phi$.

Finally, we use this inner product to define a pseudo-metric on Ψ:

$$d_K(\phi, \phi') = \frac{\|K_\phi - K_{\phi'}\|_H^2}{2} = 1 - K(\phi, \phi') \tag{4.7}$$

$$d(\phi, \phi) = 0 \tag{4.8}$$

$$\sup_{\phi' \in \Psi} d(\phi, \phi') = 1 \tag{4.9}$$

The triangle inequality naturally follows from Cauchy-Schwarz. However, the metric is a pseudo-metric due to the fact that there exists action-degenerate states, and the identity of indiscernables fails. Learning more about the nature of the degeneracies will help further characterize this metric.

We have been intentionally dropping the combinatorial level label on the states, as the induced metric only depends on the action, and we can freely compare states with different maximum combinatorial levels with impunity.

4.2.2 Direct Metric

We can introduce a countably infinite family of pseudo-metrics induced through integer p-norms directly through the combinatorial description itself. Our candidate metric η is the following:

$$\eta(\phi_m(\sqcup_{d=0}^{m}(\omega_{\alpha_d}, K_d^*)), \phi'_n(\sqcup_{d=0}^{n}(\omega'_{\alpha_d}, K_d'^*))) \equiv \sum_{d=0}^{\max(n,m)} \min_{\pi(\alpha_d^>)} \|\omega_{\alpha_d^>} - \omega_{\tilde{\alpha}_d^<}\|_p \,, \tag{4.10}$$

where $\pi(\cdot)$ is the permutation group acting on the combinatorial node indexes $\alpha^>$ or $\tilde{\alpha}^<$ at level d, which are defined as follows:

$$\alpha_d^> \equiv \text{argmax}(|\alpha_d|, |\alpha'_d|) \tag{4.11}$$

$$\alpha_d^< \equiv \text{argmin}(|\alpha_d|, |\alpha'_d|) = [\alpha_d, \alpha'_d] \setminus \alpha_d^> \tag{4.12}$$

$$\tilde{\alpha}_d^< \equiv \{\alpha_d^<, \underbrace{\varnothing, \ldots, \varnothing}_{|\alpha_d^> - \alpha_d^<|}\} \,|\, \omega_\varnothing = 0 \tag{4.13}$$

In words, $\alpha_d^>$ is the set of indexes at level d that is longer (has more nodes), while the tilde complement is the shorter index array padded with 0-weight nodes such that it has the same length as the greater index array.

The permutations allow for the closest possible distance between objects at level d while removing any labeling freedom between relative relabeling of the combinatorial data in each

state. The states are finite by definition, and have finite nodel weights with a positive lower bound, so our usage of a minimization is well defined and the metric will always constitute a sum over a finite number of terms.

In this way, any differences in the combinatorial structure are picked up by the full weights factor of the differing pieces, and any mappable pieces are minimized with respect to their weight differences regardless of their use in the higher/lower structure. As an example, under the 1-norm, the metric distance between an equilateral 2-simplex and 3 1-simplexes of the same length would simply be $3\omega_0 + \omega_2$, accounting for the extra three nodes in the unconnected graph and the 2 simplex in the connected one.

Due to the definition of the p-norm, the metric is clearly a non-negative function that maps into the reals. Each α_d is defined through the K_d^* structure, so we use the shorthand on the indexing labels alone to talk about the induced connectivity differences.

The p-norm is naturally symmetric, and the minimum can be symmetrically taken over either interior label holding the other fixed. Therefore, the outer sum is symmetric with respect to its arguments, making our proposed metric symmetric overall.

We illustrate a proof of the triangle inequality:

$$
\begin{aligned}
\eta(\phi_n, \phi'_m) + \eta(\phi'_m, \phi''_l) &= \sum_{d=0}^{\max(n,m)} \min_{\pi(\alpha_d^{>})} \|\omega_{\alpha_d^{>}} - \omega'_{\tilde{\alpha}_d^{<}}\|_p + \sum_{t=0}^{\max(m,l)} \min_{\pi(\tilde{\alpha}_t^{<})} \|\omega'_{\alpha_t^{>}} - \omega''_{\tilde{\alpha}_t^{<}}\|_p \\
&= \sum_{d=0}^{\max(n,m,l)} \min_{\pi(\alpha_d^{>})} \|\omega_{\alpha_d^{>}} - \omega'_{\tilde{\alpha}_d^{<}}\|_p + \min_{\pi(\tilde{\alpha}_d^{<})} \|\omega'_{\alpha_d^{>}} - \omega''_{\tilde{\alpha}_d^{<}}\|_p \\
&= \sum_{d=0}^{\max(n,m,l)} \min_{\pi(\alpha_d^{>}),\, \pi(\tilde{\alpha}_d''^{<})} \|\omega_{\alpha_d^{>}} - \omega'_{\tilde{\alpha}_d^{<}}\|_p + \|\omega'_{\alpha_d^{>}} - \omega''_{\tilde{\alpha}_d^{<}}\|_p \\
&\geq \sum_{d=0}^{\max(n,m,l)} \min_{\pi(\alpha_d^{>}),\, \pi(\tilde{\alpha}_d''^{<})} \|\omega_{\alpha_d^{>}} - \omega'_{\tilde{\alpha}_d^{<}} + \omega'_{\alpha_d^{>}} - \omega''_{\tilde{\alpha}_d^{<}}\|_p \\
&= \sum_{d=0}^{\max(n,m,l)} \min_{\pi(\alpha_d^{>}),\, \pi(\tilde{\alpha}_d^{<})} \|\omega_{\alpha_d^{>}} - \omega''_{\tilde{\alpha}_d^{<}}\|_p \\
&= \sum_{d=0}^{\max(n,l)} \min_{\pi(\alpha_d^{>})} \|\omega_{\alpha_d^{>}} - \omega''_{\tilde{\alpha}_d^{<}}\|_p \\
&= \eta(\phi_n, \phi''_l)
\end{aligned}
$$

In the first line, we've used primes to denote the relative weights belonging to each state, but the correspondence between which prime sits on which $(>, <)$ indexed weight vector is arbitrary. We have also selected the outer two weight vectors to permute, but this choice is also arbitrary and a similar proof can be performed for any other choice. We then extend all vectors into the largest space at each level where the sum can extend to the highest dimension as the other vectors will be padded into that space. We can pull the minimization to the front and perform it simultaneously over both permutation vectors, as the arguments are independent. Extra primes are used to help distinguish which permutation correspond to which weight vectors. We exploit the p-norm inequality, and then use the fact that the padded weight vectors on the primed states are identical and drop out. As one permutation is sufficient for the minimization now, we can drop the other minimization and relabel the highest dimension of our sum (and drop any extra padding on the weight vectors, if we so choose), and return to our definition of the metric again.

We will often use the familiar 2-norm or the 1-"Taxicab"-norm for our metrics of choice.

For $\eta = 0$, it must be true that $\omega_{\alpha_d^>} - \omega_{\tilde{\alpha}_d^<} = 0 \,\forall\, \alpha_d \,, \forall\, d$. Although this is a strong condition on the weight vectors at each level, beyond 3 roots there exists configurations that are topologically distinct due to their loop structure but have the same weight vector representation under these admissible level permutations. An example of this is a closed square made out of uniform edges compared with the boundary of an equilateral triangle plus an extra equal-length edge dangling from a vertex (similar to that shown in Fig. 3.2). Thus, we do not have the identity of indiscernables and only have a pseudometric on spaces of complexes with more than 3 nodes. However, the Forman curvature would measure the differences of these structures. As a result, our RKHS metric could provide a nonzero measure of distance between configurations that are degenerate on the combinatorial metric, and as the combinatorial metric is sensitive to scale, it would provide a nonzero measure of distance on the most common mode of action-degenerate configurations that hinder the RKHS metric. Since the sum of two pseudometrics is also a pseudometric, we can use both of them in conjunction to provide what is likely a metric over the full space minus a nearly vanishing set where both contributions fail the identity of indiscerables simultaneously.

These metrics provide a way of measuring state differences directly in the combinatorial space, giving a means to characterize fluctuations, state locality, and autocorrelations in the full quantum Markov chain.

4.3 Reduced Models for Quantum Probes

The driving force behind the numerical semi-classical analysis presented in our previous work was the combinatorial and constraint complexity of the state space that our configurations reside in. We developed an embedded state-generating procedure to probe restrictions of this state space to fixed dimensional embeddings that were amenable to optimization algorithms for sampling ensembles of local action minima. However, without formal justification for the measure densities on the new space, we could not be confident about the distribution of the states with respect to the entropic contributions under the projection of the partition function into the physical state space beyond a semi-classical analysis. Instead of continuing

to work in the covering space, in this chapter we examine what analysis can be done in the natural combinatorial space itself. To that end, we will introduce some toy models that *can* be directly sampled. In these models, we can attempt to draw conclusions about the full quantum partition function, and furthermore show that some models map exactly onto restricted regimes of our space of interest.

First, we intend to sample on the space of a fixed number of roots, unlike our initial simulations that allowed variable bulk roots. As larger roots spaces contain the smaller ones, we do not allow root removals, and instead can look at action values across different root simulations in the same parameter regimes to determine asymptotic behavior of classical configurations in the large root limit.

Broadly, if we intend to sample the combinatorial space itself, our algorithms will require a mixing of topology by sampling through the combinatorial graph states in C_n, followed by an assignment of weights on the combinatorial nodes corresponding to a sample of admissible simplicial volumes for that configuration.

We do not include any boundary structures (unless one were to consider the fixed nodes as boundaries with displacement freedom in the ambient space—the original boundary definition provided above in Chapter 3 requires fixed embeddings, so this would be an alternative to that definition). In this way, we are sampling the space of perturbations around the absolute empty state. As each point (the minimal geometric addition) carries with it a positive and gapped action contribution, we are examining the perturbations away from the empty state as a function of multiples of the minimal geometric gap. The space C_∞ contains the full topological sector of the theory.

4.3.1 Restrictions

In order to sample directly on the space of interest without the use of the ambient cover, certain constraints must be lifted. Foremost, the embeddability restraints corresponding to the labeled weights are the hardest to enforce, as there is no reasonably computable oracle for testing whether a particular abstract simplicial complex with prescribed volumes

may be geometrically realized in a fixed dimensional ambient space. Neither can we freely sample from within the space of embeddable complexes using a Markov chain as there is no algorithmic way to generate an arbitrary representative complex by construction. As a result, these simulations necessarily work in the regime where we let the ambient dimension go to infinity. Here, we are guaranteed embeddability and no longer have this set of constraints. We decouple the highest combinatorial level from the embedding dimension, and gain a new dial on admissible simplicial dimensions instead. We can then freely sample over the full space of all possible topologies without any embeddability constraints.

Although we have guaranteed embeddability, we have not guaranteed simpliciality constraints. As a result, we next face two different sets of constraints: simplicicial closure, and simplicial volume. The simplicial closure constraints are the general triangle inequalities, while the simplicial volume constraints ensure the proper volumes are prescribed by the edges alone. Each of these presents a computational challenge, and in different models, can be relaxed to provide a regime in which we can sample the space of interest.

For the rest of this chapter, we shift our level indexing to agree with the algorithm development described in Chapter 5, such that the roots lie at level 1.

Level-2 Models

If we restrict to level 2 structures only (highest dimensional simplexes are 1 simplexes), the volumes are only the edge lengths, the closures are trivial, and we can therefore sample the full space of interest directly. Due to our algorithm setup on sampling C_n, this would be a very limited state space where we can solve the path integral directly and would also overlap with our previous simulations. One could take a $C_{n\gg 2}$ state with level truncations in order to accommodate more structure, but this is not the approach we have examined at this time.

Level-3 Models

In the next highest level, we can work nearly exactly. The topology will place restrictions on the admissible edge lengths that correspond to a set of linear inequality constraints: a

minimum volume is set by the point volume, a maximum volume can be imposed by a computational IR cutoff, and the triangle inequalities are linear inequalities. This prescribes a convex polytope for the space of admissible weights. We can sample from this space to give the combinatorial nodes their weights. Although the topolgicial space was discrete, this polytope is continuous and can be sampled within using standard methods of sampling within convex bodies [45]. However, we risk including triangle areas that are less than the point volume or greater than the IR cutoff, as the polytope is only defined based on the edge inequalities and triangle area restrictions are nonlinear. As a result, we must work in the limit where we have 'soft' UV/IR cutoffs on the edges alone, or where the point volume goes to 0 and the IR cutoff tends to ∞. This is not feasible computationally, for as we take these limits, we know to expect divergences in the curvatures as the edge lengths tend toward 0 that would induce numerical instabilities. Although there are means of at least attempting simulations in such a space, we have set aside this probe for later investigations.

Level-$(n > 3)$ *Models*

Past level 3, the volume and closure constraints can't be simultaneously satisfied in linear algorithms. On the edge set, the constraints for closures become nonlinear with respect to tetrahedra (and higher dimensional simplexes), and so we will not be able to solve the constraints exactly to give an admissible weight polytope to optimize over. Additionally, prescribing weights from the highest node downward would be solving an inverse-volume problem for the lower structures (nonlinear and nonunique), while starting from the edges would require already knowing the full solution that would satisfy the existences of the higher dimensional structures.

As an attempt to study nonregular spaces with higher dimensional simplicial structure, we can linearize the model to relax the simplicial volume constraints and the closure constraints. Another way of enforcing the simplicial closure at level d is by the set of linear inequalities at level $(d-1)$. These are the equivalent inequalities as the lower dimensional triangle inequalities, as opposed to the description of the constraints using the edge set alone that

become nonlinear past the 2-simplex. We can enforce simplicial closure level-by-level using these inequalities. If we were to pick a set of weights from this polytopes prescribed by these inequalities, however, we would not have the freedom to satisfy the inequalities of the next level unless we already knew they were satisfied initially. Thus, this model must also break simplicial volume restrictions. That is, we ensure that each level has a set of weights that satisfies the linear closure constraints based on the topology restrictions of the level above, but the following level is agnostic to those volumes, and the process starts anew. In terms of volume alone, this is equivalent to moving from a simplicial structure to a cellular structure. For example, although the three edges constituting the boundary of a 2-simplex would be forced to satisfy a triangular closure, the subsequent triangular volume may be greater or less than the simplicial one induced by the edges (corresponding to a spherical or hyperbolic deformation of the triangle area). Furthermore, this does not guarantee global simpliciality. Ensuring an edge set closes to form a particular triangle set, and the triangle set closes to form a particular tetrahedral set, does not guarantee that the original edges closed to form the tetrahedra, and we can not bootstrap our way into global simplicial closure. Ultimately, we result in a type of deformed cellular extension of the original model, with closure enforced only to linear order. If we see strong geometric behavior out of simulations in this relaxation, it implies that the original constraints were not necessary ingredients for our construction and even broader classes of complexes with entirely foreign notions of curvature and defects also naturally form the emergent structures we are interested in. If we do not see such behavior, we must do more work to carefully understand whether the constraints are necessary or whether this model is simply too distant from the original space of interest.

We emphasize again that all of these models only map onto a regime of the physical space that has high enough dimension sufficient for admitting any geometric embedding of the underlying combinatorial data. It may be the case that the dimensional restriction or localized boundary data are key properties for seeing emergent triangulations of lower dimensional structures, which may play a role in shaping our view of emergent dimensionality.

We anticipate that the above relaxation is too strong to see the geometric properties we

expect. Without the simplicial constraints, there is no longer any geometric penalty in highly connected states to have arbitrary simplicial volumes, and as a result, the curvatures alone will be extremized, derailing the balance between volume and curvature that demonstrated the geometric phenomenology we hope to study. Confirming the hypothesis of this probe is the object of current work.

Regular Symmetric Models

If we restrict to complexes built from uniform edge lengths (a regular abstract complex), we can immediately sample freely. The edge weights are fixed as a parameter, all higher volumes are known immediately by the closed form volume expression for regular simplexes, closure is guaranteed, and the point volume and optional IR cutoff will be the only parameters that can cut off combinatorial levels as weight restrictions. On the fixed space of n roots, the most complex structure one can build is the regular $(n-1)$-simplex. As a result, this corresponds to sampling the topological space consisting of all regular subcomplexes of such a simplex—a highly symmetric space, but an interesting one where we also have a lot of analytical control due to the regularity property. Simulating this regime now only requires a topology sampler with a dilation parameter for the overall scale, and a study of the emergent topologies as a function of cosmological term and point volume. A sampler on the raw space of abstract simplicial complexes is akin to sampling on a space of monotone boolean functions, for which we developed two algorithms discussed in Chapter 5.

We can additionally let the uniform edge length become a dynamic parameter, coupling two Markov chains (one on the topology space and one on the line segment of UV/IR admissible edge weights). At the cost of computational complexity and acceptance rates, this will give us a window in the full statistics of regular abstract complexes, and this is the approach we have taken for our investigation.

4.3.2 Gauge Freedoms

In practice for the full numerical simulations, the issue of gauge fixing does not influence the partition function due to the double precision on the weight space. We do not expect to ever sample gauge equivalent states except in the case of the fixed boundary data that can impose constraints on the weight space and induce gauge equivalent samples through fixed relative coordinate data on the roots. Additionally, the ability to add or remove roots would be the next largest source for gauge equivalent states, and this is explicitly forbidden in the above regimes we intend to study. However, in the fixed and uniform edge length space, the weight space is already induced from the topological space, and as a result, we can admit gauge equivalent configurations with measurable probability in general. To fix this freedom, we would have to either perform gauge fixing after simulation through data reduction, searching though our samples and reducing them to single representatives, or divide out by the gauge volume of the symmetry upon calculating our partition function observables. The gauge volume is set by the cardinality of the fixed-weight graph isomorphism class, and analytical forms are unknown [62]. Explicit computations are also too computationally expensive to perform, and have not been done in general past complexes with 7 elements. We do know, however, that the space of equivalent configurations becomes a small fraction of the total space as the number of roots increases. For complexes with a small number of elements, there can be many equivalent configurations (although even less for our fixed root case considered in our simulation construction), but as the number of elements increases, the number of inequivalent configurations that have no symmetries grows dramatically. Therefore, in our effort to know about the large root behavior, we can be confident in our multiplicities sampled by the algorithm, and in the low root number regime, we can analyze the state data for perturbations around the classical minimum and explicitly examine whether these states happen to be those that have topological gauge. Our simulation results indicate that the dominate states are those with a single representative and a large action gap between the nearest energy state, and as a result, we can be reasonably confident with the long-horizon

distribution of our sampler at low temperature in this sector as well.

The regular complex simulation with dynamic edge lengths is a probe that nearly avoids this problem. Although it is possible for a state to avoid an edge length transition while making a topologically isomorphic transition, these cases will be exceedingly rare in the ensemble due to the joint probability of the coupled Markov chains and the fact that these isomorphisms are already sparse, as mentioned. As a result, our sampler will travel gauge orbits with extremely small probability.

4.3.3 Sampling on Subcomplexes of a Regular Simplex

Constrained Space

In this section, we examine topological properties as a function of the number of available roots, using the original space that necessitated the existence of a simplex if its topological and geometric constraints were met. We computed topological observables such as the number of connected components, Euler character, and maximal simplicial level, plotting heatmaps to illustrate the stark phases present when the parameters are varied. We plot the metric fluctuations from the classical state using the combinatorial pseudo-metric, which due to its apparent uniformity throughout the bulk phases and deviations near the phase boundaries, demonstrates both the stability of the phases and that the metric is a strong indicator for topological phase boundaries as measured by simplicial structure. The percentage triangulation plot takes the largest simplicial dimension in a given configuration, and asks what percentage of components are a part of this structure. For example, a 2D tesselation of the plane would yield 1, while the same structure with errant 1-simplexes unconnected as a part of the triangulation (either as disjoint pieces or simply as not a member of a participating 2-simplex) would have a percentage measure less than 1. Disconnected pieces do not contribute as triangulations, explaining the strong correlation between the number of connected components and the percentage triangulation plots. However, this strong correlation also suggests that simplicial uniformity is the most likely feature, and we do not expect lower

dimensional structures that are not a part of an existing higher dimensional triangulation. This informs us that our previous classical 2D simulations that sometimes terminated with 'hanging edges' not a part of the emergent triangulation are fluctuations from deeper classical minima and are signals that the optimization had not yet converged as opposed to minima themselves. The minimal action is presented here as well, although this quantity is more relevant for the length-varying simulations as those occur at fixed parameters and as such require the action plot to better understand the classical phases.

In the highest-level plot, red numbers are used to indicate when new degrees of freedom (higher simplicial levels) become accessible due to the varying point volume cutoff. Level 2 (edges) are always accessible by parameter choice, and higher levels become accessible as the point volume is lowered until the maximum is reached on the given number of roots.

In the following plots, we fix all edge lengths to be 2, and impose no IR regulator or level restrictions. We sample at unit combinatorial temperature. We vary the point volume parameter through its applicable range of $(0, 2]$, and vary the cosmological term Λ within an order of magnitude surrounding 0.

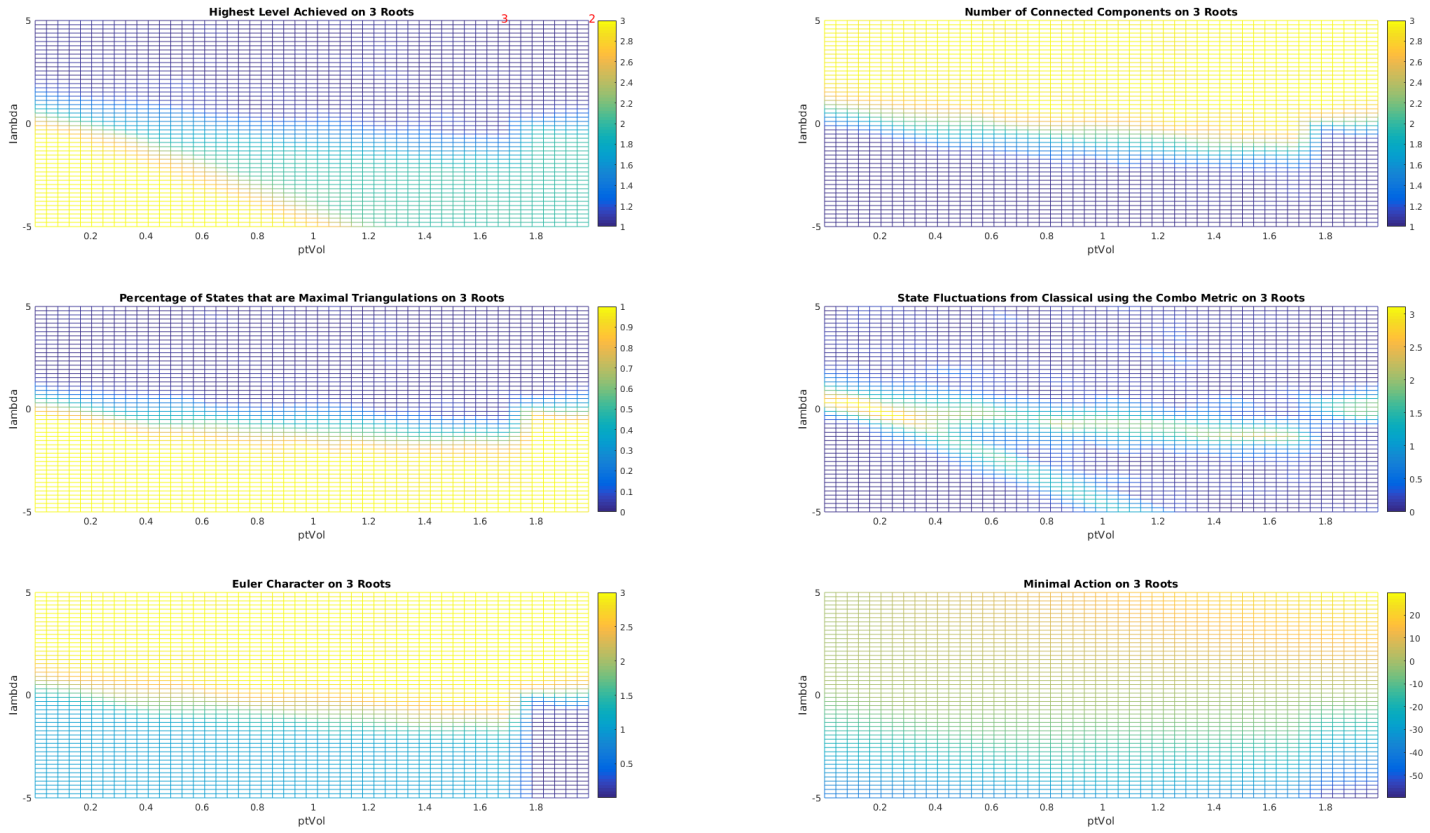

Figure 4.1: Unrestricted Fixed Scale 3 Root Simulation Space.

On 3 roots, we see four distinct topologies. There is a region of large Λ wherein no structures are formed, echoing our results of the classical simulations at large lambda. Instead, we yield 3 disconnected roots. For small or negative Λ and point volume less than 1, we have a full 2-simplex. There is a region to the right of this that shares the same Euler character, but does not achieve the same simplicial dimension, indicating that the structure is the simplicial join of two line segments. Lastly, we have the large point volume and large negative lambda regime where we have an un-filled 2-simplex that must arise because the combinatorial weight was less than the point volume.

In Figure 4.1, we provide an example analysis of the phase behavior that we witness for these simulations. Figs. 4.2 and 4.3 show the simulation results for 5 and 6 root systems, which carry much of the same qualitative behavior. Smaller point volumes allow for higher simplicial degrees of freedom to be accessible, and the smaller the cosmological term is, the more likely the system is to take advantage of those degrees of freedom. Within the same parameter window by 6 roots, it is evident that the phase patterns that emerge are generated in the bottom left region, and propagate towards the upper right corner of the plots, indicating that larger lambda values would be necessary to see the full (but similar) picture as in the 5 root case. We see that simplicial dimension does not jump to the largest available structure when the degrees of freedom are immediately accessible. In fact in the strictly positive cosmological regime, the largest dimensional structures are not accessed for a fixed number of roots. Increasing the number of roots, however, shows a comparable increase in simplicial dimension at the same parameter points, indicating that for an arbitrary number of roots, one might expect maximal complexes.

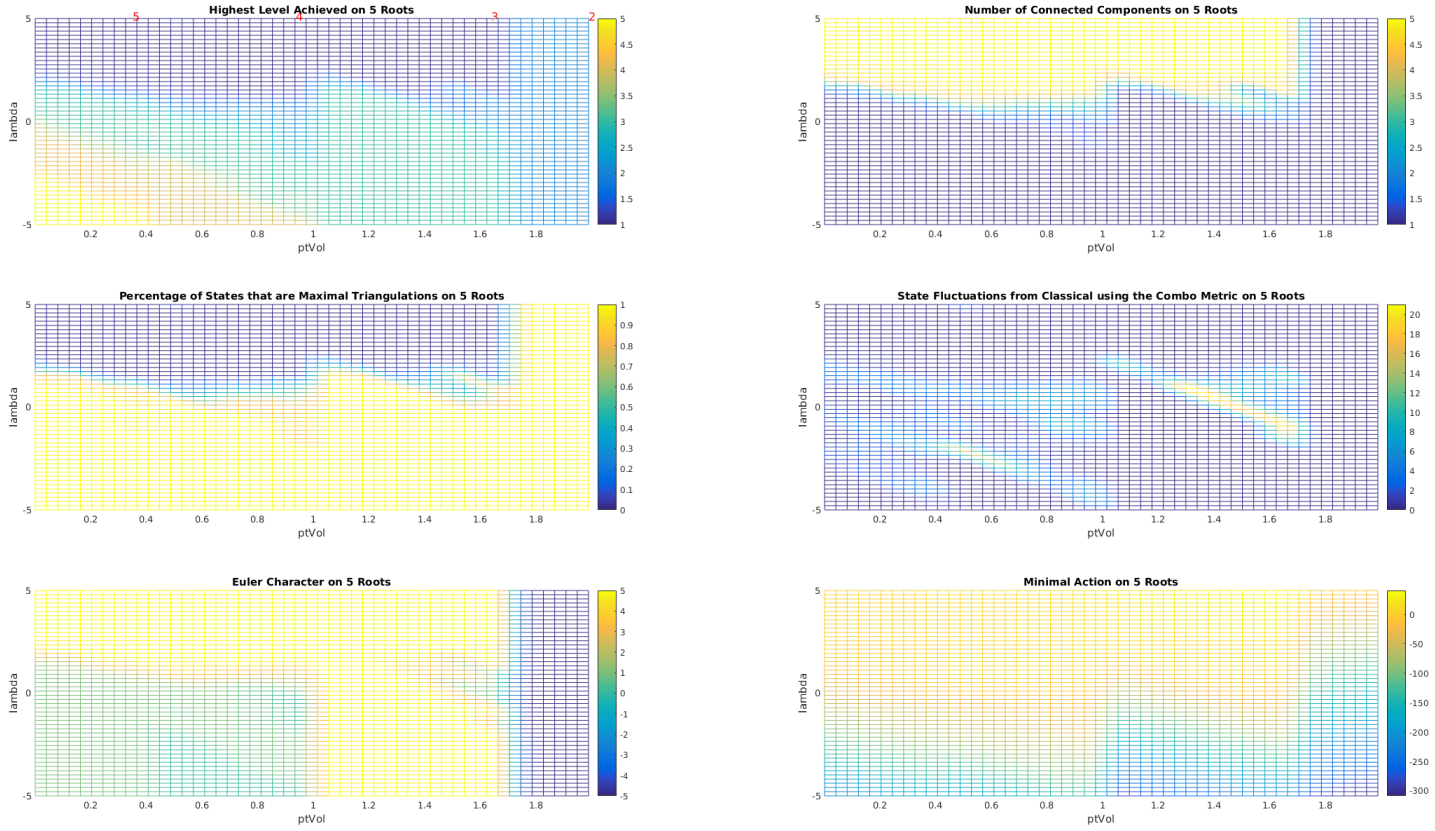

Figure 4.2: Unrestricted Fixed Scale 5 Root Simulation Space

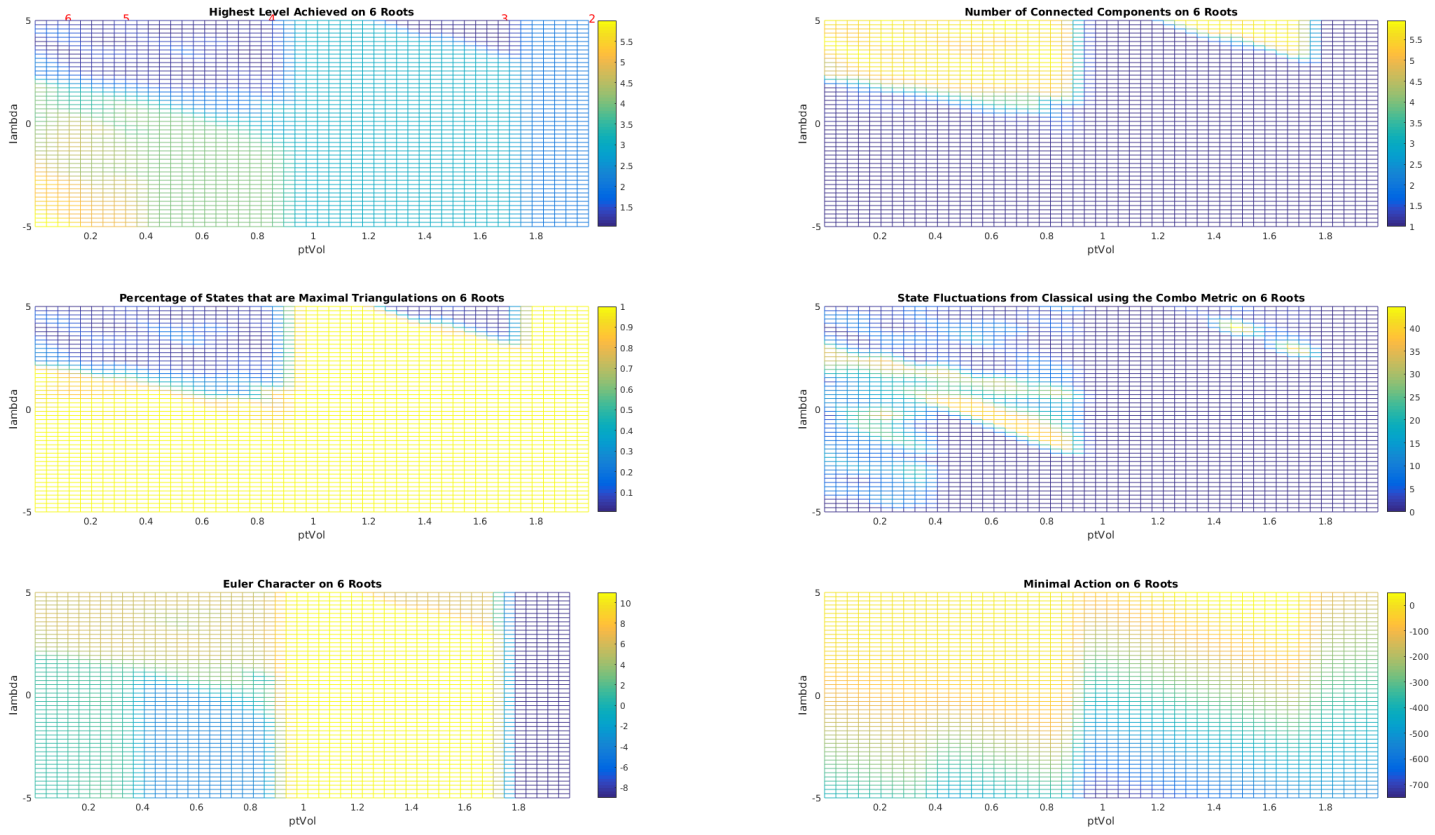

Figure 4.3: Unrestricted Fixed Scale 6 Root Simulation Space

Looking at the other regions, the topology echoes this maximal complex behavior. We can align the maximal dimension along with the connectivity data and the Euler character to determine that the structures are often complete graphs on the number of roots. As the point volume is lowered for small/negative Λ, the skeleton begins to fill in, level by level, filling all available boundary holes with the full dimensional simplex. The classical structure appears to be the complete 2-skeleton on the roots, which gradually fills with higher dimensional pieces until it forms the largest simplex possible. This indicates an ultra-local behavior, where every point is connected to every other, and all simplicial dimensions are accessed

maximally.

The reasoning for this is likely due to the fact that we have lifted the restrictions of the ambient space. Without a fixed dimension, all simplicial structures are possible and at fixed edge length there is no geometric penalty to connecting all structures as every node can live in its own subspace independent from the others, insuring that there are no geometric intersections. In such a space, every point can be arbitrarily close to every other without embedding considerations of the larger simplexes, and with a completely connected 2-skeleton, one could still geometrically realize all possible higher dimensional simplexes that contain the 2-skeleton up to the maximal simplex on the fixed number of roots. This seems to indicate the importance of the geometric embedding restrictions to the original model and the classical simulations. A fixed dimensional ambient space would not only cap the highest dimensional simplex, but would also restrict the connectivity of the structures due to their geometric intersections in the restricted subspaces, leading to the conclusion that a fixed ambient space may be essential to see emergent geometry that does not exhibit ultra-local behavior.

Looking instead at a point volume slice at $\omega_0 = .001$, an infinite IR regulator, and varying over positive Λ and the fixed uniform edge length, we examine the expectation of the largest simplicial dimensions achieved as well as the action map to indicate the flow of the fixed structure toward a given scaling within a particular phase. For simulations on 3 and 5 roots shown in Figs. 4.4 and 4.5, we see a distinct minimum in the action at an edge length around 1.25. We also see that despite being in the positive cosmological regime, we can achieve maximal simplicial dimension for the right edge lengths. This indicates that the simulations performed at a fixed edge length were only accessing a slice of the possible configurations, and the phases are not globally stable once perturbations to the combinatorial weights are included. This also suggests the importance of fixed boundary structures, as they set additional length scales that, for a fixed number of free bulk points, may constrain the classical states enough to avoid the ultra-local and maximal simplex behavior. For the use of this paradigm in understanding optimal networks between existing network structures, this

provides reasonable plausibility that the global minimum will not always be the structure of maximally connected nodes.

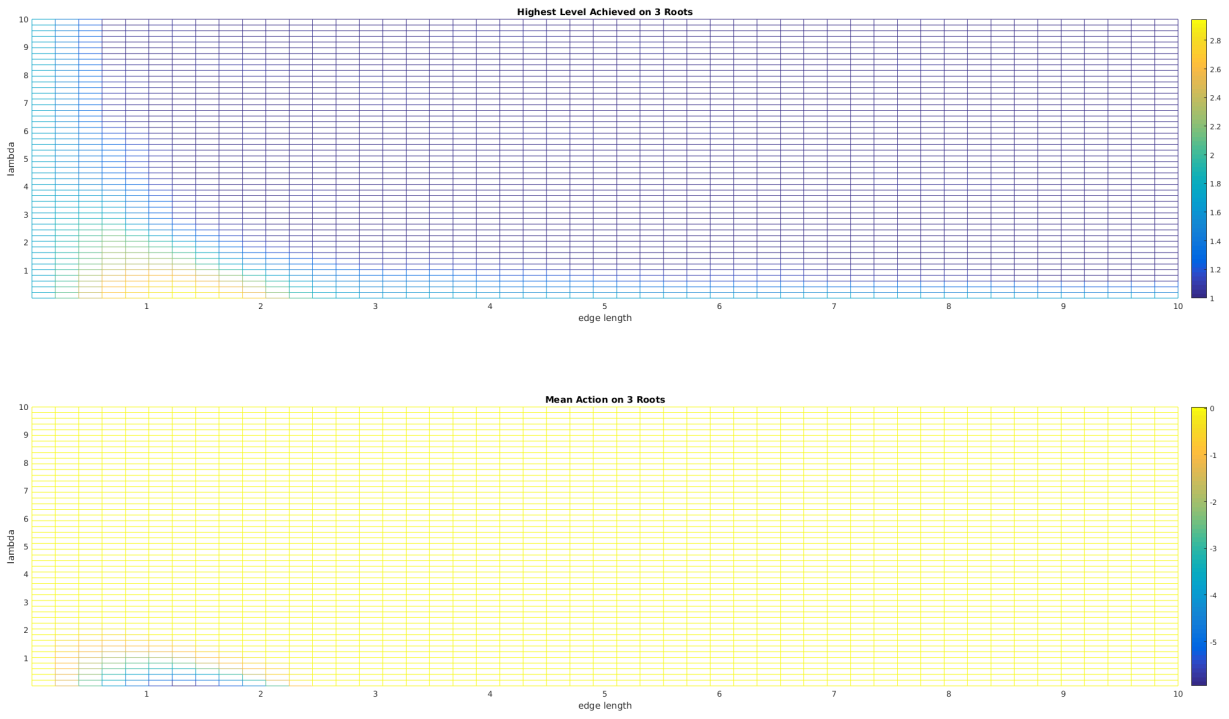

Figure 4.4: Unconstrained Variable Scale for a Fixed Point Volume 3 Root Simulation Space

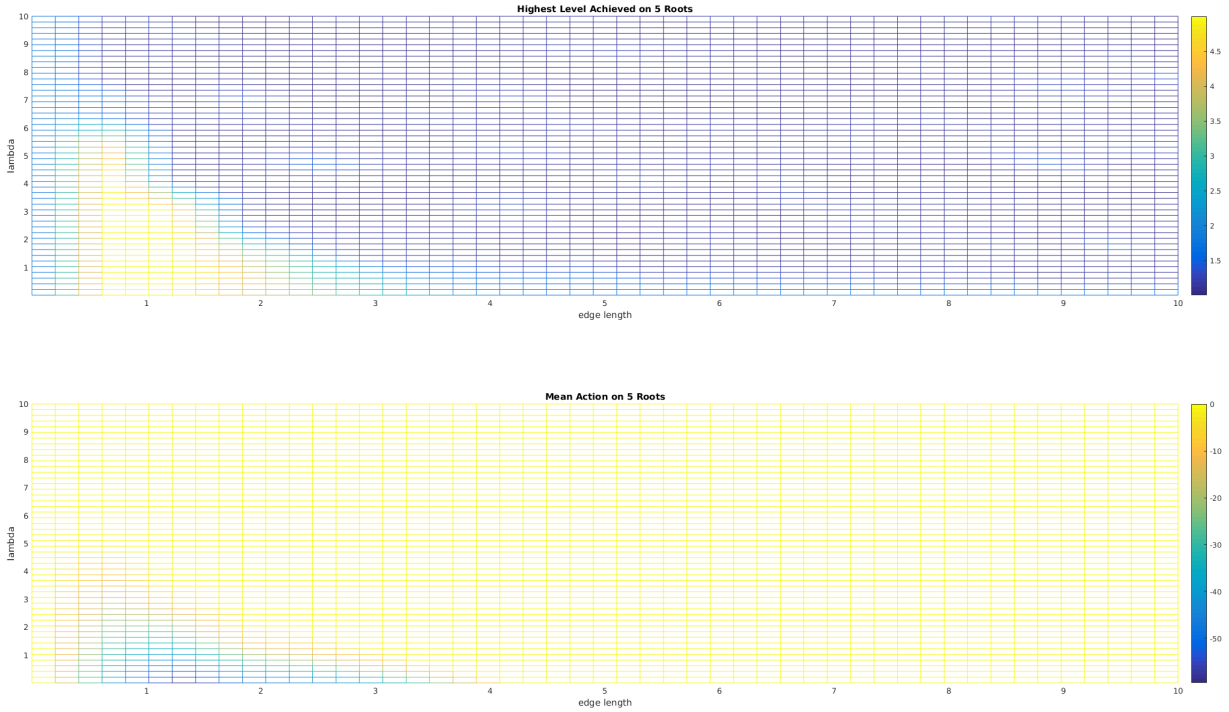

Figure 4.5: Unconstrained Variable Scale for a Fixed Point Volume 5 Root Simulation Space

Furthermore, we notice that for these uniform and highly symmetric structures, there is no evidence for the IR divergence. The classical scale is fixed to be many orders larger than the point volume, but still a finite size. This is confirmed by direct analytical solution for regular simplex scalings and shown in Fig. 4.6.

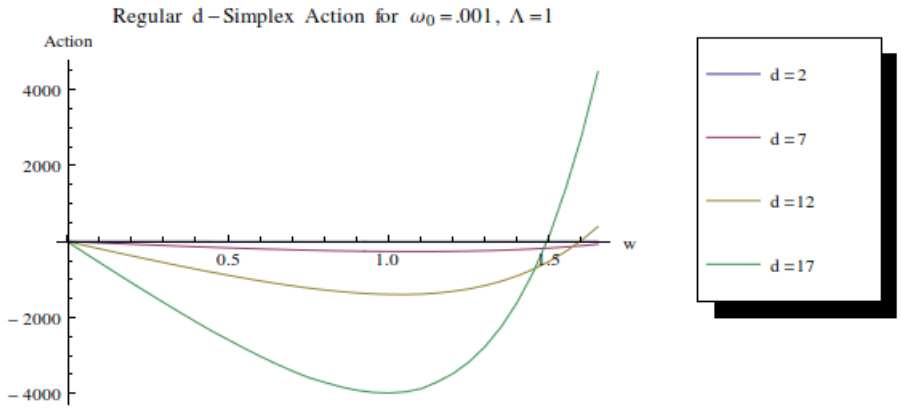

Figure 4.6: Action Scaling for Some Regular d-Simplexes at $\Lambda = 1, \omega_0 = .001$

Moving away from the sliced simulations and utilizing a Markov chain that includes scale transitions, we can examine the full space at once. We look at the 5-root space where Λ is positive, as this is the interesting sector of our model. Fig. 4.7 shows various observables as before, while Fig. 4.8 shows the average regular scale over the parameter ranges. We note that the low Λ low ω_0 regime exhibits the behavior we see in our sliced simulations, with the topology maximized while the edge length is bounded. Increasing Λ pushes the topology lower in level, as our classical results echo. The well separated topological regions are no longer prominent in these figures, as the fixed edge length simulations on regular structures induce a tight correlation between accessed levels and admissible levels due to the point volume cutoff. With a dynamic edge length, the scale is continuously adjusted between topology phases and we see a smearing of the transitions.

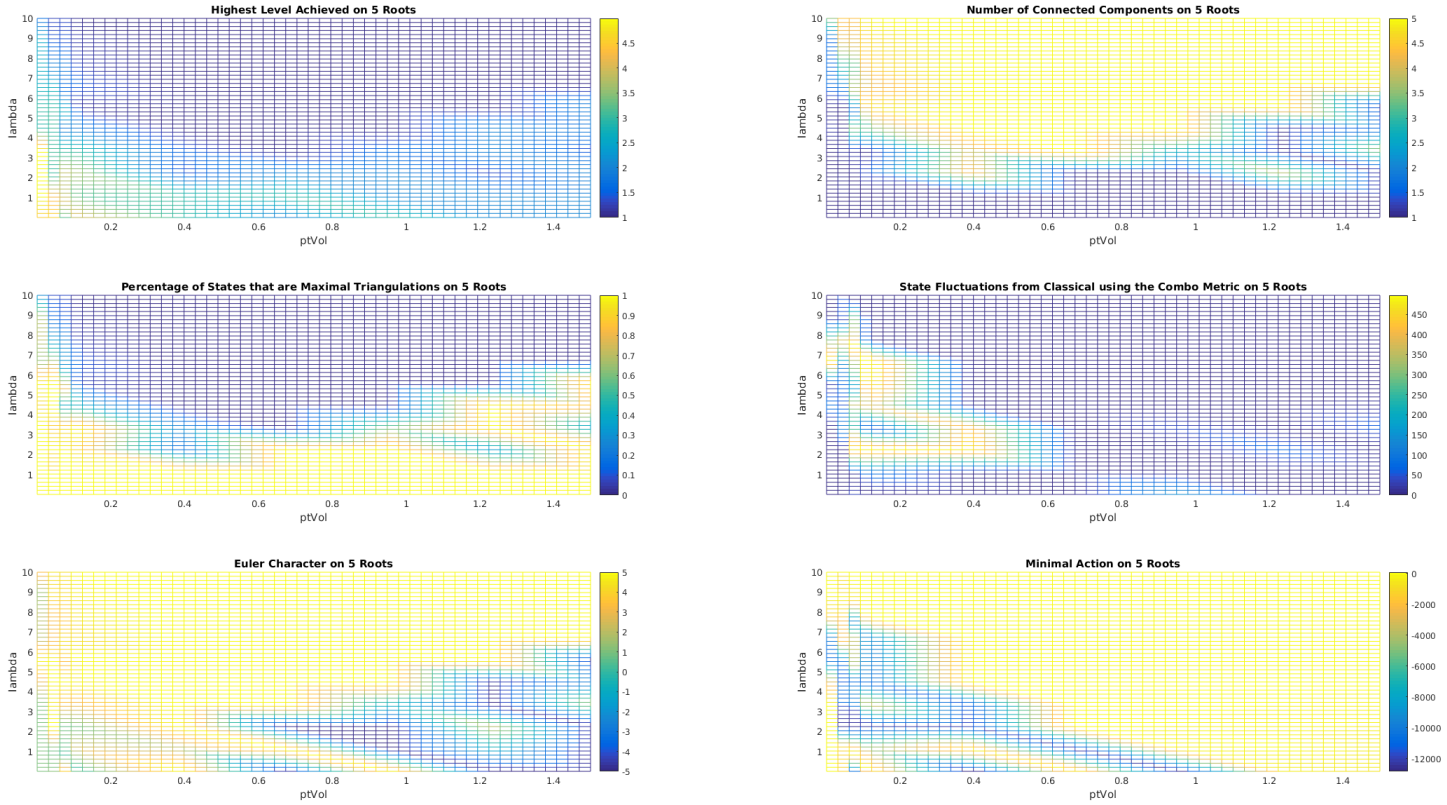

Figure 4.7: Unconstrained Dynamic Scale for a Fixed Point Volume 5 Root Simulation Space, with an IR cutoff at $\omega = 10$

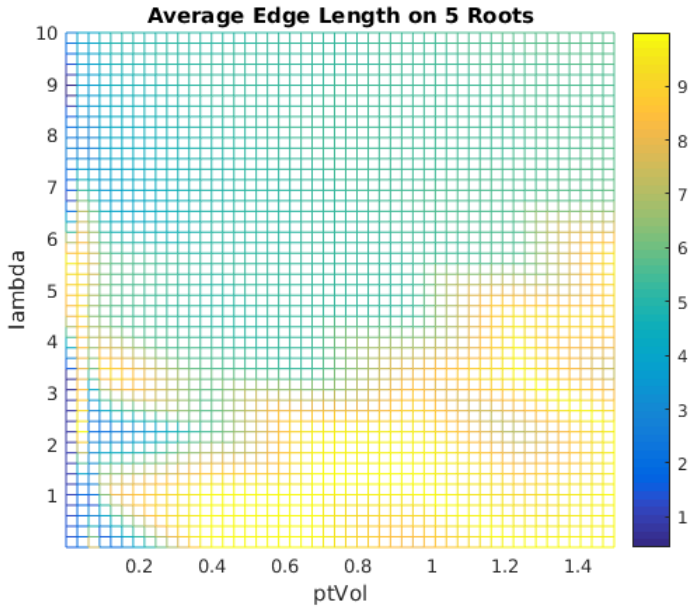

Figure 4.8: Unconstrained Dynamic Scale for a Fixed Point Volume 5 Root Average Scale Plot, with an IR cutoff at $\omega = 10$

Extended Space

In these simulations, we lift the restriction imposed in the classical simulations on the existence of a simplex provided its edge structure exists and there are no geometric/intersection related prunings. As mentioned, this is a much larger state space, but may also aid in the maximal simplex divergence issue as such as structure is no longer required given the proper 2-skeleton. This is a relaxation of a constraint, but the above simulations are contained within this one. If the above minima are global in the full space, we would see the same results with some potentially larger fluctuations due to the additional degrees of freedom. However, we do not see such a result. Instead, we find a new landscape.

The following figures are the same parameter range heat maps with the simplex forcing lifted. In particular, Fig. 4.9 gives a detailed breakdown of the features of the heat maps that can be then applied to the higher root figures.

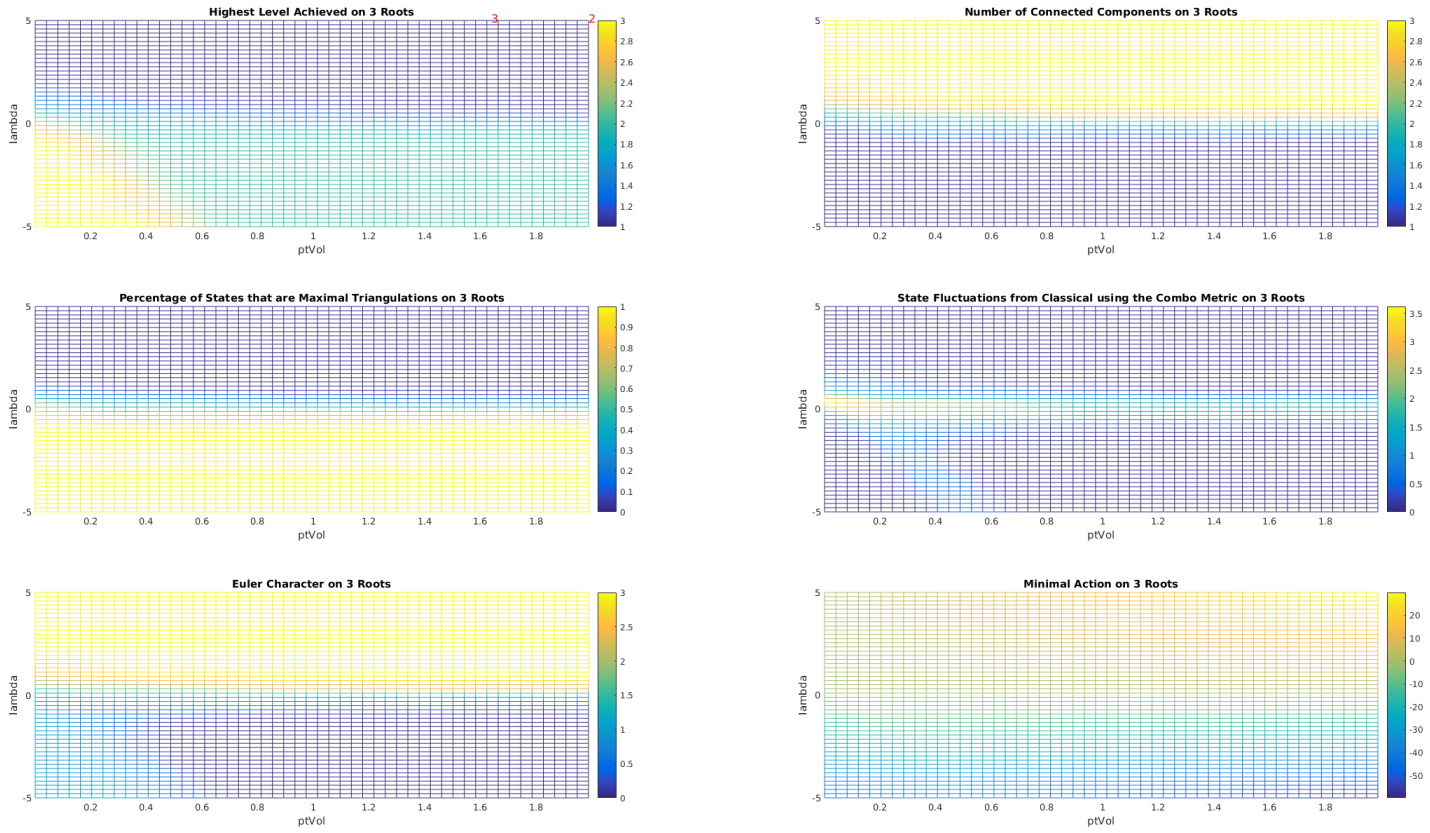

Figure 4.9: C_3 Fixed Scale Simulation Space.

On 3 roots, we see a very similar structure as before, but with the phase in the bottom right corner taking over the bulk of the low cosmological regime. Previously, this was due to the forcing requirement generating a 2-simplex, but the minimal combinatorial weight removing the face of that simplex until accessible, after which it was forced to be present. Now, the classical solution is to not include the face at all for a much larger parameter space, eliminating the former phase entirely that had the simplical join of 2 edges in favor of an empty 2-simplex. The full 2-simplex regime resumes in the lower left, as before.

As seen in the higher root simulations in Figs. 4.10, 4.11, and 4.12, over the same parame-

ter range as the constrained space, we no longer see the emergence of the highest dimensional simplexes for positive cosmological regime. In fact, the highest dimensional building block is fixed to be the 2-simplex. This is in extreme contrast to the earlier simulations that ran toward arbitrarily high dimensional simplexes provided enough roots. The topological properties, however, are similar in that the structure is still ultra-local. The Euler character, along with the other topological observables, informs us that the states peak around the complete 2-skeleton on the fixed number of roots as the classical topology. This provides more evidence to the necessity of the embedding restrictions if one desires an extended body. Although we no longer have maximal simplexes, in this arbitrary dimensional ambient space, there is no penalty to maximally connecting the edge structure. However, this structure is still very interesting in that it has the topology of joins of spatial 2-spheres. Each of the highest accessed nodes on level 3 is a member of the boundary of 3-balls and the global structure is the maximal simplicial fusion of these spheres, giving the structure of a spatial foam. We can hypothesize that with the additional constraints of a fixed embedding dimension, some of these connections must either be broken—leaving a partial triangulation for which our discussed evidence suggests is not the expected structure—or the structure may simply 'unfold' into the available space, producing less than the maximal number of possible 2-simplexes while maximizing the number of spheres. Restricted to a 3-D ambient space, this has the potential to create a 3D spatial foam of topological bubbles with local connections to neighboring bubbles at their boundaries, and a minimal number of nonlocal bubbles as ultra-local defects between spatial points.

One way to test this hypothesis would be to again look at the classical simulations and examine the minima, at least, for such behavior, once we expand the state space to be compatible with the above relaxation. Our 2D simulation should still show a triangulation of the ambient space as we have found previously. However, once we move to the 3D ambient simulation, the signal of having a minimal realization of possible 3-simplexes with a proliferation of 2-simplexes in topological spheres would be strong evidence to confirm our hypothesis.

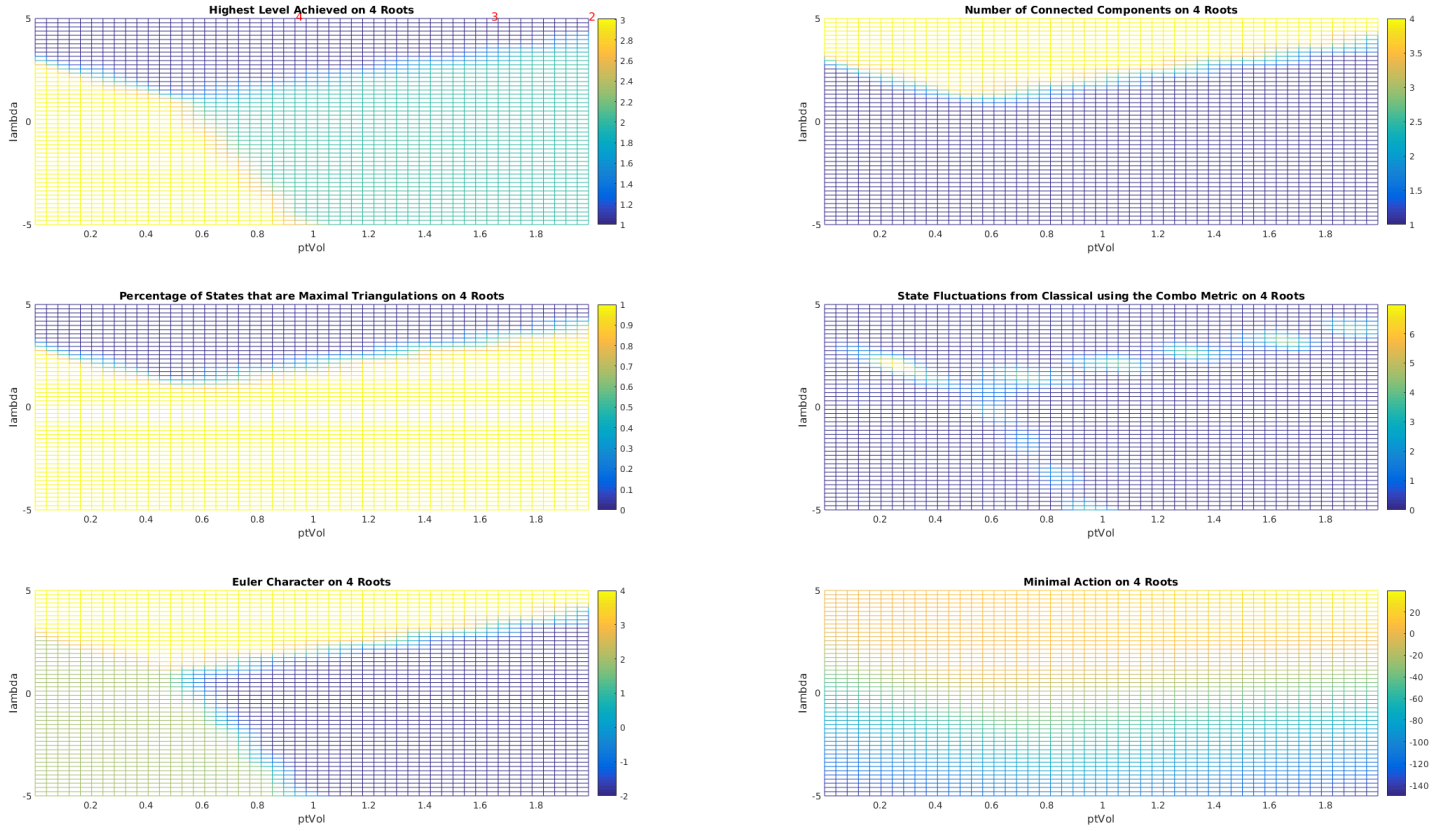

Figure 4.10: C_4 Fixed Scale Simulation Space

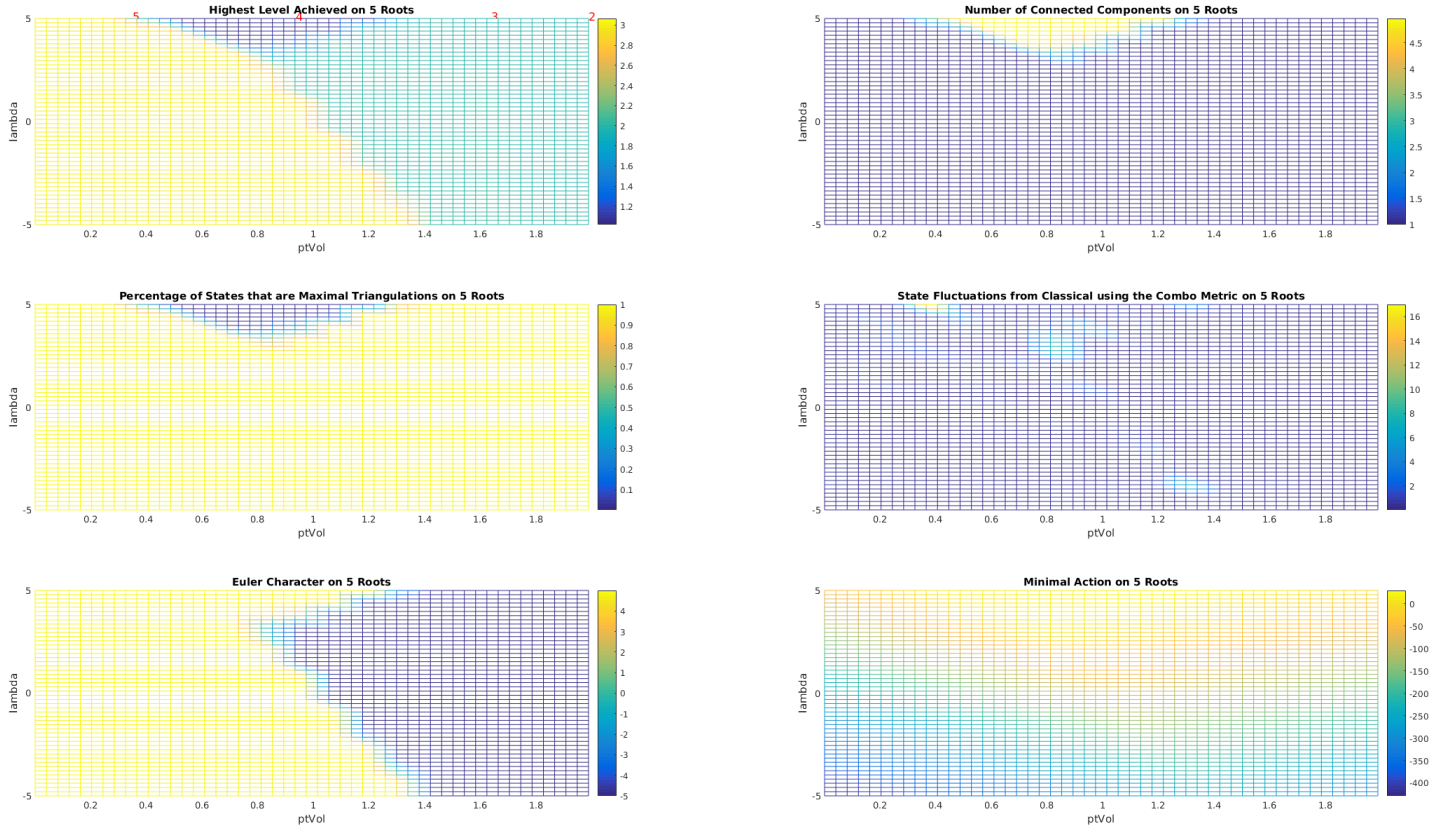

Figure 4.11: C_5 Fixed Scale Simulation Space

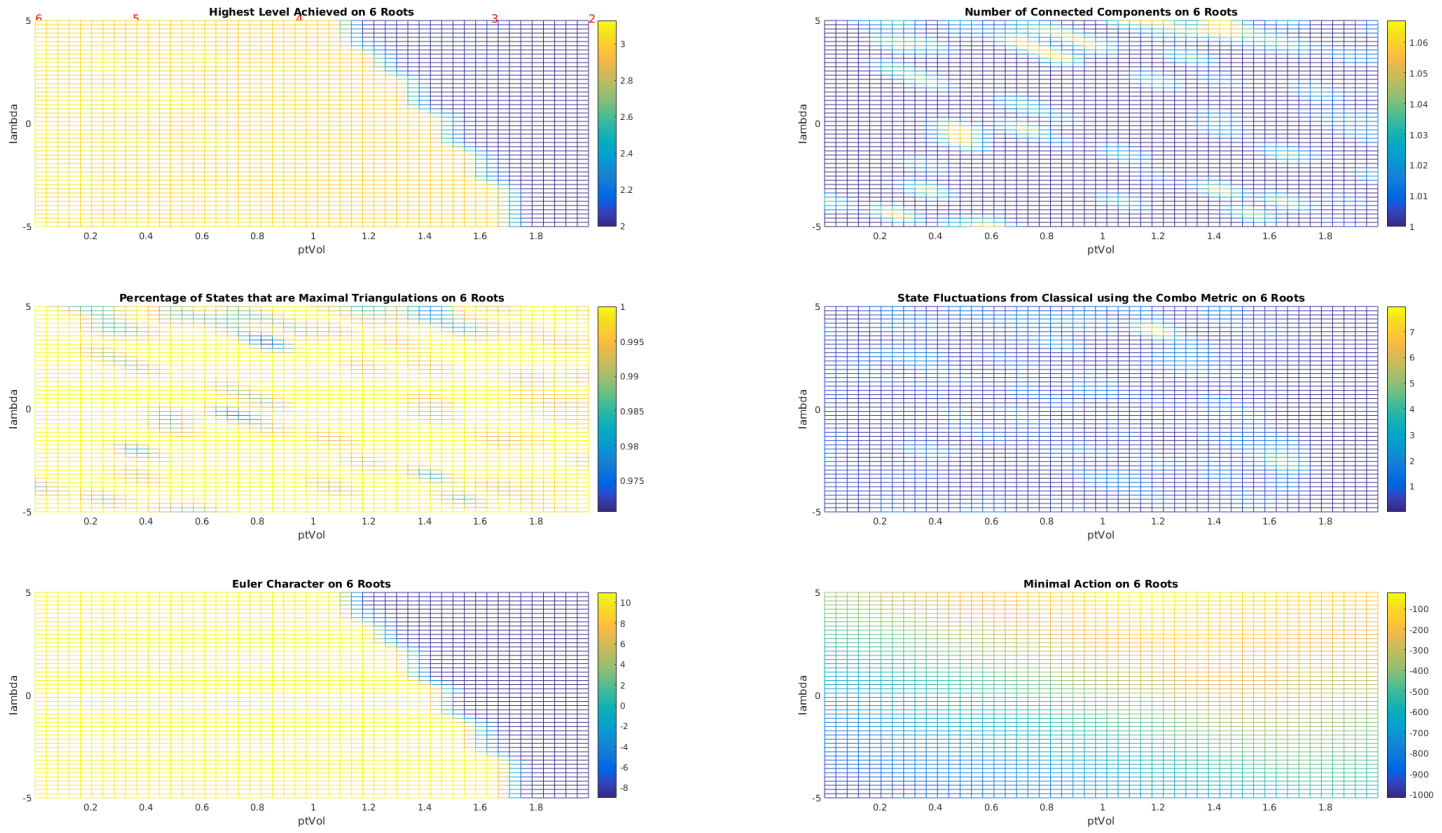

Figure 4.12: C_6 Fixed Scale Simulation Space

We note that in the negative cosmological regime for sufficiently low Λ as shown in the extended Fig. 4.13, we do access higher simplicial structures. This provides more evidence that the $\Lambda > 0$ regime can support the interesting emergent geometry, while the negative regime includes geometric divergences.

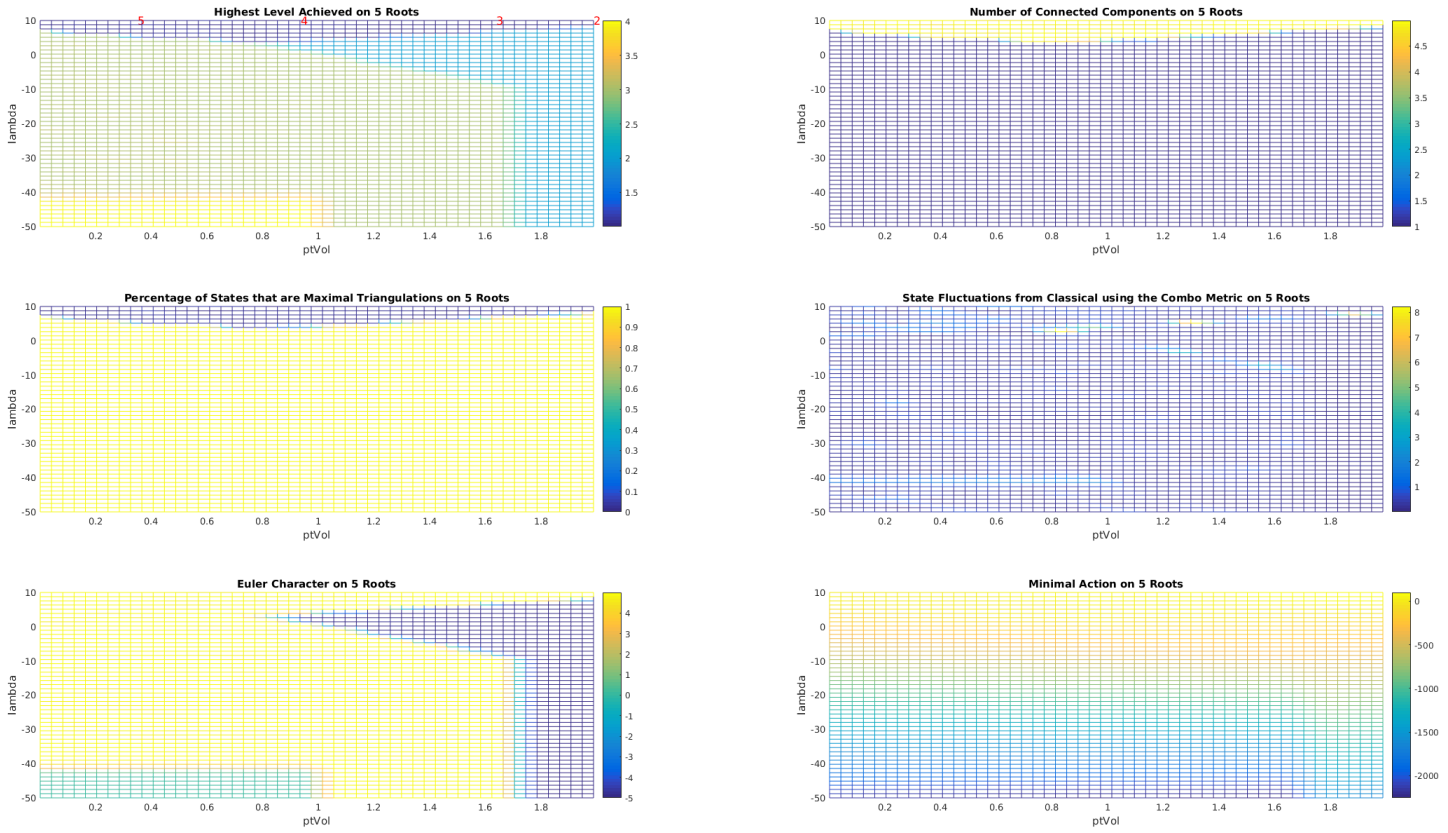

Figure 4.13: C_5 Fixed Scale Simulation Space, Extended Λ Sweep

We now continue our comparison to the constrained space and vary the fixed edge length instead, as before. However, the results are again very different. As seen in Figs. 4.14 and 4.15, we still see that higher simplicial dimensions may be accessed in a narrow window of fixed edge lengths, which may be mitigated against by boundary structures as discussed above. More importantly, the action plot indicates that unlike the previous case wherein the higher structures held the classical states and caused a geometric flow toward those solutions, here the flow is *away* from those states. The 3-root case shared the earlier behavior exactly, but beyond 3 roots, we see the IR divergence manifest wherein the classical flow involves

states that grow monotonically without bound as we increase the number of roots for fixed lambda. This is also confirmed through direct analytical analysis of the action shown in Fig. 4.16.

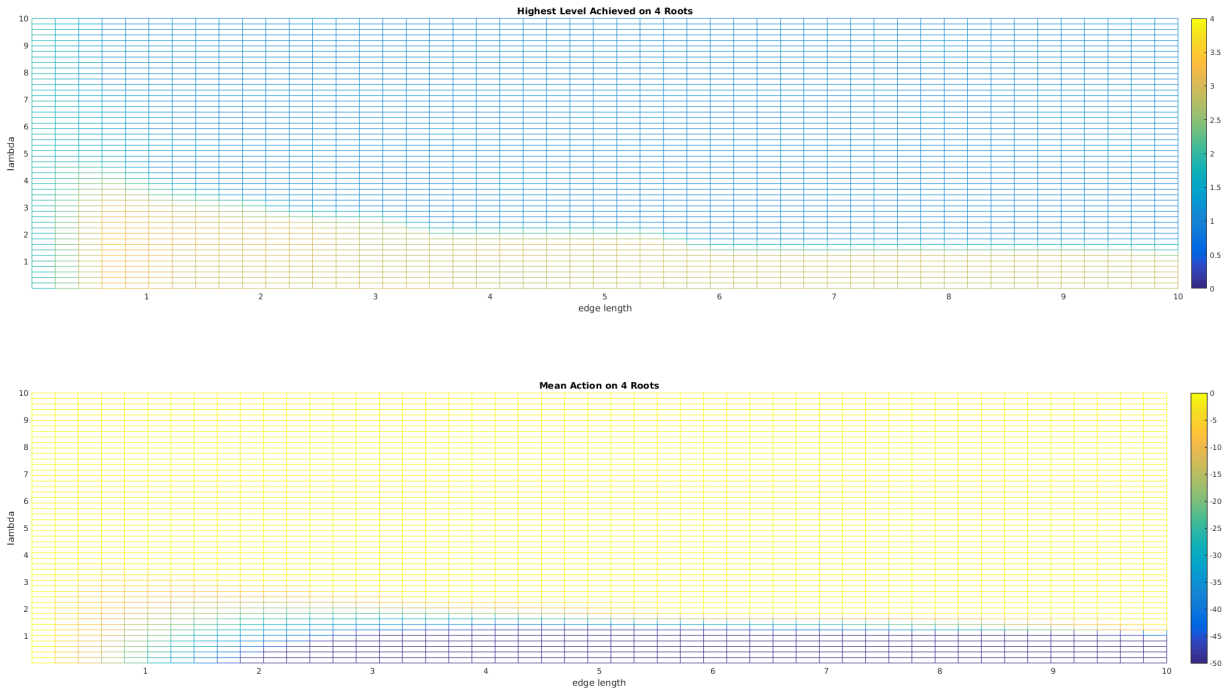

Figure 4.14: C_4 Variable Scale for a Fixed Point Volume Simulation Space

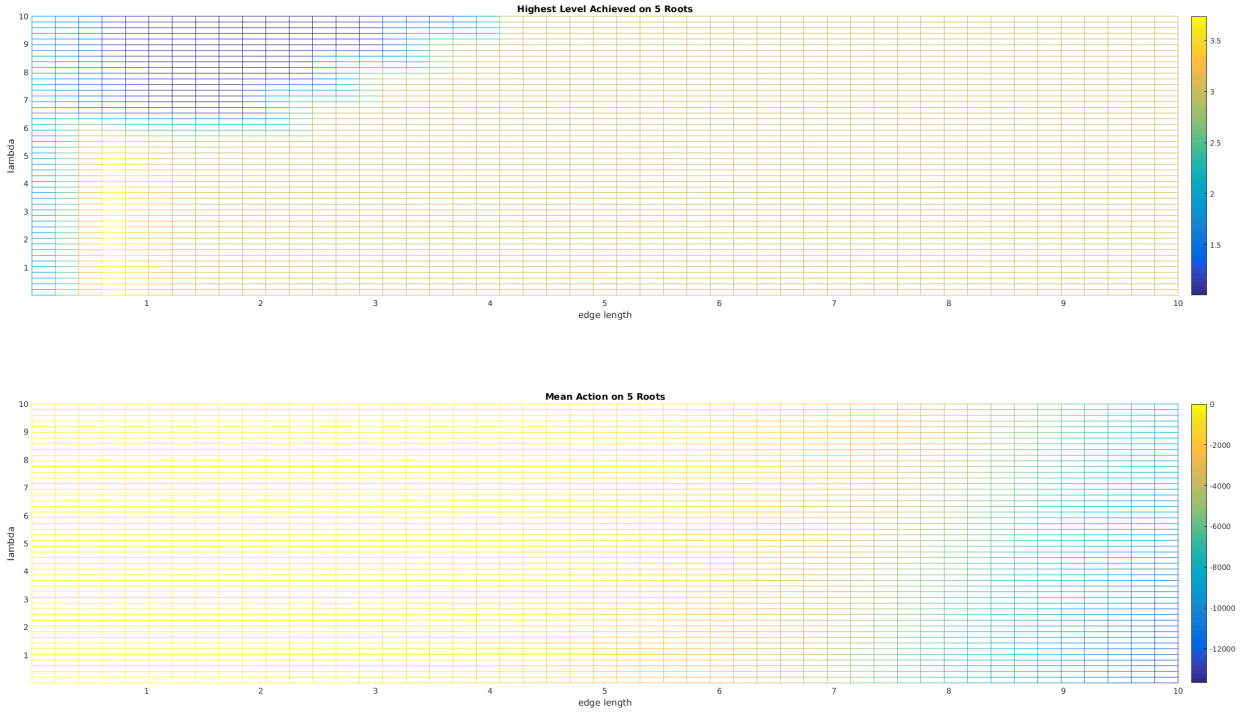

Figure 4.15: C_5 Variable Scale for a Fixed Point Volume Simulation Space

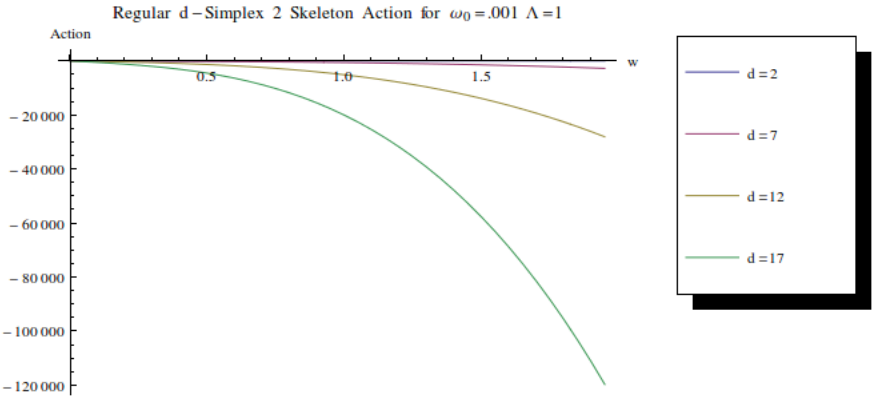

Figure 4.16: Action Scaling for the 2-Skeleton of Regular d-Simplexes at $\Lambda = 1, \omega_0 = .001$

In probing this divergence for higher root structures, however, we actually find a new transition in combinatorial level. Although the measure appeared to concentrate over the 2-skeletons even through a 5 root system, by 6 roots with sufficiently large enough scale factors (which were not accessed during our sliced simulation), we see the emergence of a phase that peaks around the 3-skeleton on level 4 with IR divergent scale. Both a low point-volume sliced simulation shown in Fig. 4.17 and the full dynamic edge length simulations shown in Figs. 4.18 and 4.19 demonstrate this behavior. To better understand this structure, we examine these phases analytically in the next section.

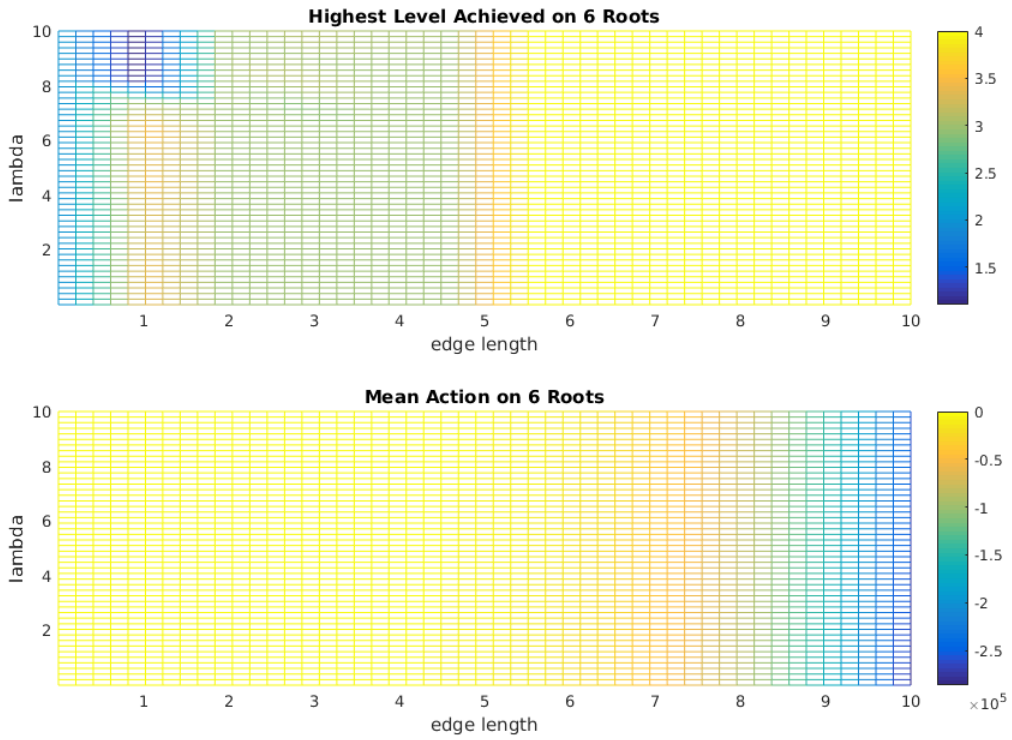

Figure 4.17: C_6 Variable Scale for a Fixed Point Volume Simulation Space

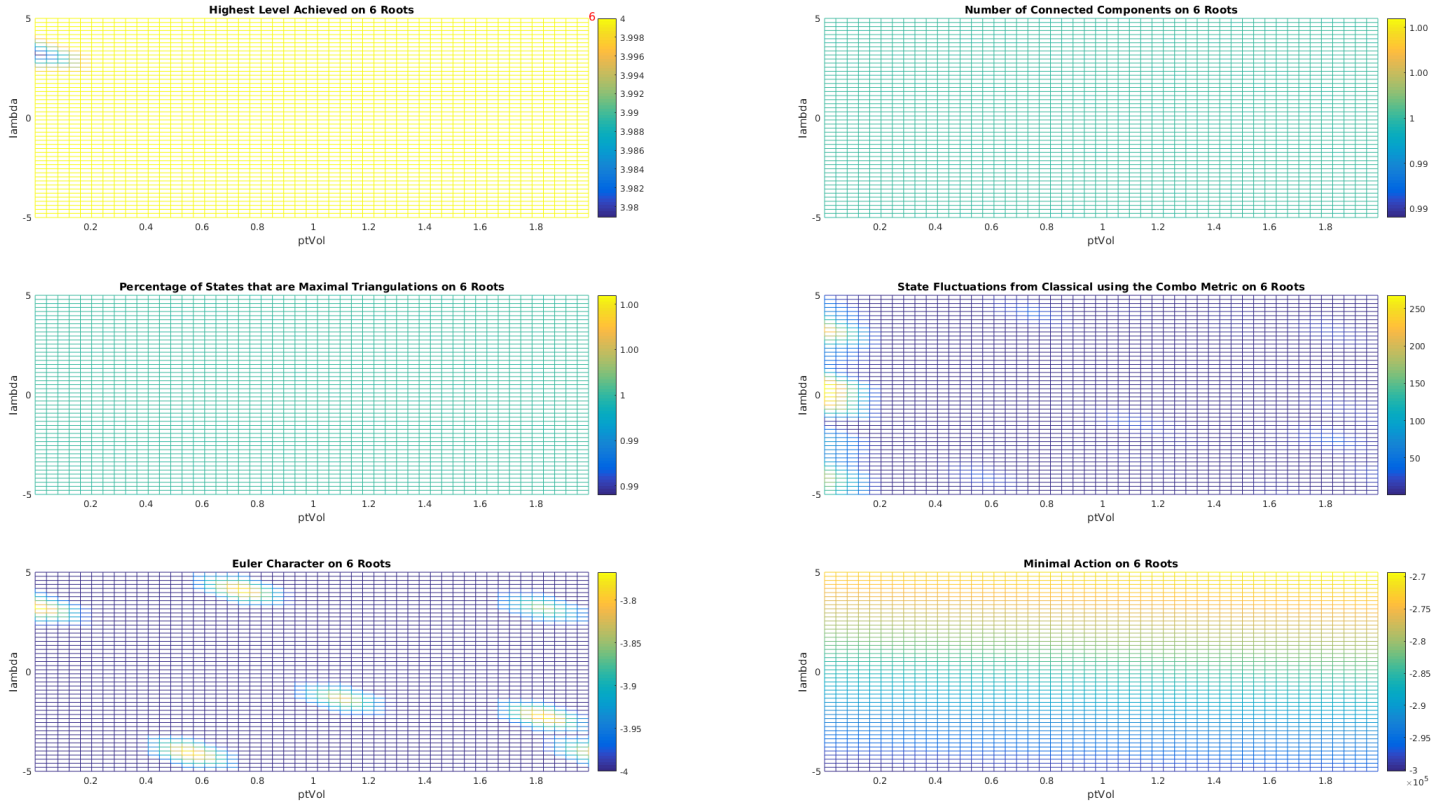

Figure 4.18: C_6 Dynamic Scale Simulation Space, with an IR cutoff at $\omega = 10$

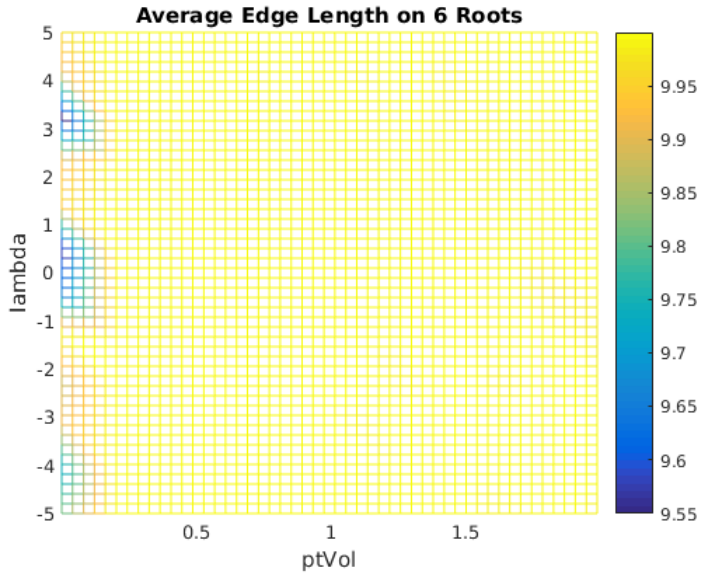

Figure 4.19: C_6 Dynamic Scale Average Scale Plot, with an IR cutoff at $\omega = 10$

4.4 Simulated False Vacua and Analytic Rectification

In an effort to more firmly determine on what topological structure the measure concentrates for the unrestricted space, we can now turn to analytics as the action of a complete n-skeleton of a regular simplex can be computed exactly. We note that these configurations have no gauge equivalences for fixed root labeling, and also have no entropic multiplicities, so examining the energy contribution alone is a reasonable approach for studying the partition function given that our simulations seem to indicate the measure concentrating on these structures.

We examine from the 5-root ($d = 4$) structures onward, and confirming our simulations, we find that the 2-skeleton configuration is not stable as a function of the regular edge length for fixed cosmological and point volume parameters. We witness a false vacuum, illustrated in Fig. 4.20. Our assumption that the point volume was setting simulation scale and that examining over many orders of magnitude larger than $\omega_0 \ll 1$ would be sufficient for probing the space on that slice was proven not to be true. In fact, with only slightly larger length

scalings at higher root systems, we would see that this vacuum tips over into higher skeletal structures, shown in Fig. 4.21. Analytical results indicate that instead of the 2-skeleton, one can always find a large enough scaling for a given regular d-simplex such that the measure concentrates on the $(d-2)$-skeleton for $d \geq 4$. This is still interesting behavior, as not all possible simplexes participate in the state. However, it is a far cry from the spatial foam we had hoped to find when the measure appeared to be concentrated on structures with maximal simplicial dimension independent of the ambient dimension and the available simplicial dimensions.

One may ask whether the IR divergence is driving this new vacuum, as evidenced by the increase in scale required and the action scaling monotonically with length as shown in our sliced simulations above. Assuming we are treating the physics correctly, we can at least confirm that given our action, a fixed $\omega_0 \ll 1$, and a sufficiently high number of roots, we can always tip the 2-skeleton vacuum into a higher simplicial state provided a variation in volume scale. Fig. 4.22 illustrates this, where we examine the same $\omega = 1.8$ scaling as in Fig. 4.20 where we witness the false vacuum, but simply crank up the available roots to the 20-simplex. Thus, in an infinite dimensional ambient space with no geometric restrictions and an arbitrary number of roots for the regular $\lim_{d\to\infty} d-$simplex, the measure is ultimately concentrated on the divergent geometric structure of the $\lim_{d\to\infty}(d-2)$ skeleton. However, the relationship between states connected by the scale and complexity transformations discussed both in Sec. 3.12.1 and Sec. 3.12.2 open the possibility that we should be enforcing a symmetry of states induced under these 'combinatorial diffeomorphisms,' and thus vacuum solutions that admit an arbitrary number of free nodes or unbounded scales may be in some way spurious. Understanding the mechanism behind the transition between the false vacuum and the global state will aid our ability to distinguish this physics. Promoting the currently unfixed symmetry and properly accounting for it in the partition function may resolve the divergence seen here and elsewhere in our model.

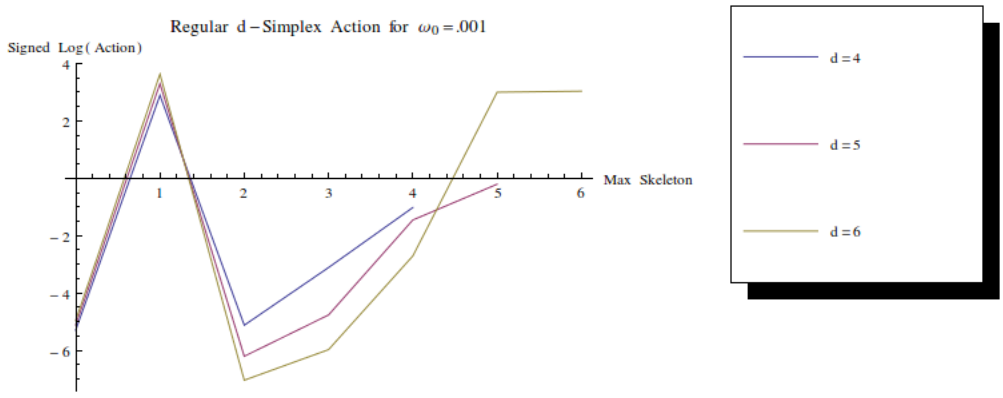

Figure 4.20: Action Scaling for the n-Skeleton of Regular d-Simplexes at $\Lambda = 1, \omega_0 = .001, \omega = 1.8$

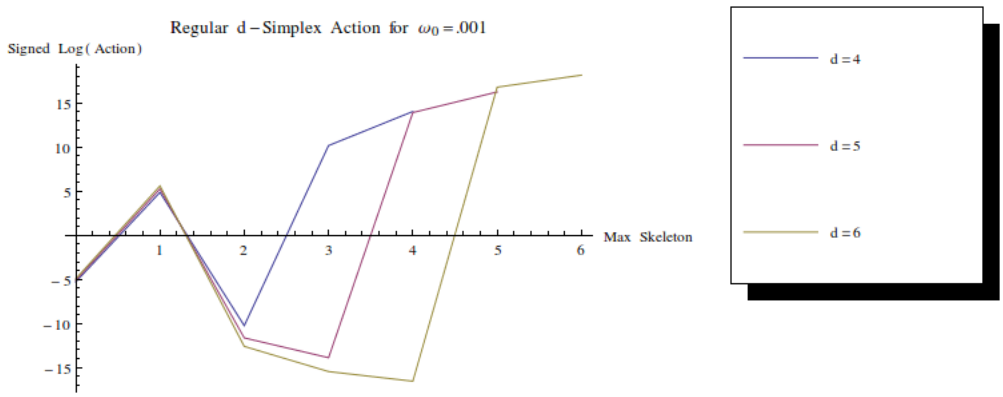

Figure 4.21: Action Scaling for the n-Skeleton of Regular d-Simplexes at $\Lambda = 1, \omega_0 = .001, \omega = 13$

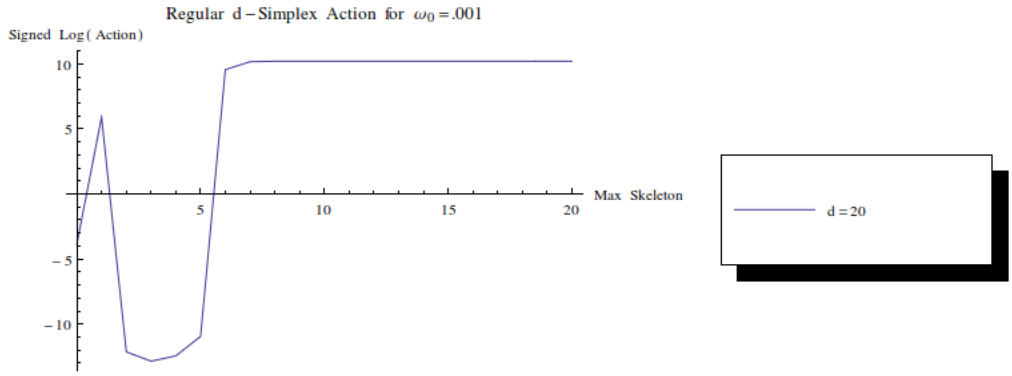

Figure 4.22: Action Scaling for the n-Skeleton of a Regular 20-Simplex at $\Lambda = 1, \omega_0 = .001, \omega = 1.8$

4.5 Future Directions and Remaining Questions

Our goal was to investigate a regime where the full partition function could be studied numerically exactly instead of simply looking at the classical saddles through an optimization scheme with a projection map onto a feasible computational space. We identified the space of regular complexes on a fixed number of roots in an infinite dimensional ambient space as providing such a playground, and developed new pseudo-metrics and Markov chains in order to sample the state space. We discovered that the original formulation has a curious feature of IR stability in volume scale, but combinatorial divergence in topological complexity, where the measure concentrates on the highest available simplex with a compact scale for small ω_0 and small positive Λ. In stark contrast, the relaxed model with a wider state space on the full space of abstract simplicial complexes initially exhibited stability in topological complexity but a divergence in the IR length scale, where the measure appeared to be concentrated on the 2-skeleton of a maximal simplex with flow towards large volumes. In an effort to understand the scale divergence, we used the simulations as guidance and turned back toward a numerical analysis of the action directly. There, we discovered that the simulations were probing a false vacuum, and for sufficiently high root structures, the measure will instead concentrate on

the $(d-2)$-skeleton of the maximal simplex. Thus this regime appears doubly divergent in both scale and topology unless elevating and enforcing our refinement procedure as a genuine gauge symmetry renders these solutions unphysical and maps the divergent results back into low dimensional geometric states.

Furthermore, we learned that in either paradigm, lifting the embedding restrictions and allowing for an infinite dimensional ambient space results in an emergent structure that is ultra-local in edge lengths. An open question remains on how these results carry over to the finite dimensional models where the embedding restriction holds, or when we have nontrivial boundary states.

We still have a wide scope of open questions, both those yet unanswered from our first investigation and also a new interest in the embedded simulations for low ambient dimensions to better understand how the results from the infinite dimensional symmetric case may or may not carry over. We also have a heightened sense of necessity for better interpreting and addressing the IR divergence and its connection with refinement along new gauge orbits, which this latest probe has shed light on.

Chapter 5

ALGORITHM DEVELOPMENTS

5.1 Introduction to the Space and Use of Abstract Simplicial Complexes

Whether used to model information theoretic phenomena like social networks or to study the combinatorial properties of fundamental structures in understanding emergent geometry, abstract simplicial complexes have a rich history of applications and are increasingly used in physics as powerful tools with extensive mathematical structures [46]. Unlike 1-dimensional graphs which only convey connectivity data between nodes, abstract simplicial complexes (ASCs) are generalizations that can allow representations of data through higher-dimensional geometric structures, such a surfaces and volumes in the form of combinatorial triangles and tetrahedra (and their higher dimensional equivalents). Informally, an ASC is the combinatorial abstraction of a geometric simplicial complex encoding the downward closure property. Unlike a geometric simplicial complex where the intersections of any two simplicies in the complex must also be a simplex in the complex that is in the union of the boundaries of the intersecting simplicies, ASCs only require that any boundary of a simplex is also a simplex in the complex. For example, the clique complex of a graph—the set of all complete subgraphs—is an abstract simplicial complex on the vertices. For a graphical picture of the differences of an ASC with a geometric simplicial complex when embedded into an ambient space, see Fig. 3.3.

This structure allows one to model more complex association data that may not be captured by the limited degrees of freedom in a traditional graph or directed graph. Many models that involve these structures are generative, which is to say that one has a well defined way of prescribing a constructive growth paradigm and studying the complex emergent properties of the resulting states [67]. However, statistical physics models on the space of simplicial

complexes and ASCs with certain structures are becoming more popular [11]. Although work continues to formally understand the topological properties of this space, finding descriptive algorithms with known probability distributions still requires concentrated effort—especially for models that would be computational feasible [14].

5.2 Challenges and Solutions in Sampling Abstract Complexes

In the course of our work developing a combinatorial space for studying emergent geometry, we faced the challenge of developing algorithms to efficiently sample on this space for our numerical probes. In Chapter 3, we introduced our combinatorial state space as a type of weighted ASC. Efforts to understand the full measure concentration of our model as presented in Chapter 4 required a way of generating samples from this space using some form of ergodic and reversible random walk to be used in a Metropolis Algorithm.

Our goal in this chapter is to introduce a new sampling algorithm that we developed that is both generative and descriptive on the ASC space C_n with a fixed number of nodes n that can then be used for sampling within algorithms that require random walks on this space, such as the oft used Metropolis Algorithms within Markov Chain Monte-Carlo methods employed throughout computational physics. Due to the combinatorial explosion, the cardinality of this space becomes very large very quickly with increasing n. Richard Dedekind in 1897 was the first to count the number of such configurations, as labeled ASCs are related to monotone boolean functions [17]. Dedekind numbers, which count the number of ASCs with m elements, are only known for $m \leq 8$; however, asymptotic formulas are also known for large m. For the purposes of sampling the unique (nonisomorphic) configurations in the space, we need to remove the labeling that introduces equivalence classes of states under label automorphisms. The inequivalent state cardinalities (and their asymptotic forms) are known only for $m \leq 7$, and grow to be on the order of 5×10^6 by $m = 7$ [62]. We note that these numbers provide an upper bound on $|C_n|$, as they also include nodal removal. Nevertheless, efficiently sampling such a high dimensional space, especially given the equivalence classes, is a challenge. Since there is not yet a general way to know the cardinalities

of the isomorphism classes of simplicial complexes on n nodes, we can do little to tune our algorithm to accommodate this directly. Furthermore, designing either a reversible walk or a sampler with known transition probabilities on such a constrained space is an additional challenge that we face.

In the sections to follow, we introduce two new algorithms for sampling on C_n. We design some basic guiding principles that we show analytically yield a non-local uncorrelated fully ergodic sampler that exhibits extremely strong sampling properties. We numerically illustrate its fast and wide sampling capabilities in comparison to a benchmark model. We also design a local ergodic random walk with known transition probabilities that, at the cost of autocorrelation, samples even more efficiently. We characterize the autocorrelation of the walk, and numerically test it against our sampler.

5.3 Notation and State Visualization

As there are a variety of ways to encode the data of a state $C \in C_n$, we take the opportunity to clarify for the reader the representation we will work with.

Definition 1 (Digraph Representation G)**.** *A state $C \in C_n$ is expressed in a leveled digraph representation $G[C]$ if each node α_d in the digraph at level d represents a $(d-1)$-simplex in C, with α as a member of the indexing set on level d, $\alpha \in [1, |\{\alpha_d\}|]$. Defining the set $\{\alpha_1\}$ to the be 'roots' of the graph with no incoming edges, the directed adjacency structure is constrained such that the following conditions are satisfied:*

1. *Directed edges exist only between levels $d \to (d+1)$*
2. *The number of parents of node $\alpha_{d>1}$ must be d*
3. *The number of roots corresponding to the union of the heads of all dipaths leading to α_d must be d*

The last condition guarantees simplicial closure, such that for each simplex, its boundary set are also nodes in the graph state with the proper completeness. There can be at most

$\binom{n}{d}$ nodes in a level, corresponding to the ASC that is the complete clique complex on n nodes. Similarly, the maximum level is $d = n$.

This graph representation encodes an ASC uniquely up to α labeling. We denote the *geometric* state as one in which the labeling has been removed. For an example of a labeled state with a canonical ordering, we illustrate in Fig. 5.1 the complete state on 3 roots corresponding to a 2-simplex.

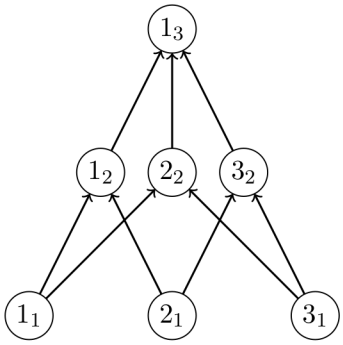

Figure 5.1: A Representative Graph State Corresponding to a 2-simplex

The convenience of this representation allows us to repackage the boundary closure constraints into the adjacency structure of this digraph, with the directed nature proving useful for easily identifying branching subgraphs affected by said closure.

Let the complete state on n nodes be denoted C_n^*. Define $F : C_n^* \mapsto C$ as a boolean function that assigns $0 \vee 1$ to each $\alpha_d \in C_n^*$ such that the conditions 1 are satisfied, with $\alpha_d = 1$ indicating existence of node α_d and $\alpha_d = 0$ indicating removal of said node.

It is trivial to see that the space of all such functions $\mathbb{F} \ni F$ covers C_n. F provides an arbitrary labeled ASC in the graph representation $G[C]$. Isomorphic states are related by boolean functions equivalent up to subset permutations preserving the constraints.

On C_3 for example, using a representation of F as a vector with elements mapped to graph nodes in their level-canonical order starting at the roots, the masks [1111100] and [1111010] correspond to the same geometric state and can be shown to be equivalent through the

allowed subset permutation on the elements corresponding to level $d = 2$.

5.4 Kahle's Inductive Construction

Kahle recently introduced a construction for generating random ASCs [36]. We describe some of its properties here, using our above notation.

Definition 2 (Kahle's Model)**.** *Kahle's multi-parameter model* $\Delta(n, p_2, \ldots, p_n)$ *builds an ASC inductively, starting at the edge set with* $d = 2$*. For every* α_d*, include the simplex with probability* p_d *provided it satisfies the boundary conditions in Def. 1.*

The full state is built level by level, with constraints on the allowable set of nodes one can include at a given level due to the boundary existence requirements induced by the lower levels.

Let $|\alpha'_d|$ indicate the number of included simplicies at level d and $|\alpha^*_d|$ indicate the number of possible simplicies given the $(d-1)$ structure:

$$|\alpha'_d| \leq |\alpha^*_d| \leq \binom{n}{d}. \tag{5.1}$$

A labeled state $G[C]$ is generated with probability P_Δ given by the following:

$$P_\Delta(C) = \prod_{d=2}^{n} {p_d}^{|\alpha'_d|}(1-p_d)^{|\alpha^*_d|-|\alpha'_d|}. \tag{5.2}$$

As shown by Zuev *et al.*, Kahle's model is an Exponential Random Simplicial Complex, implying that it generates a maximum entropy ensemble for an expected number of simplicies in the skeletal structures (directly constrained by the probability parameters) [68].

We note that the probability of achieving a particular state decreases as a binomial power in the number of total nodes in $G[C]$. Even under a nonuniform probability weighting of the levels, it can be easily seen that the combinatorial multiplicities of nodes in each level create a sampling that is highly peaked around states with a given maximum level for large n—either one that terminates early at the lower levels leaving no higher structures, one that does the opposite, or one that samples toward the 'half-graph' state with $\approx \lceil n/2 \rceil$ levels in

the case when we take the probabilities to be coin flips. Precise fine tuning would be needed to allow for sampling across a stretch of widely differing geometries, and the power behavior for finding a particular state will still not be mitigated. Additionally, the isomorphism classes of geometric states will be sampled from with additional probability based on their sizes. As the number density of labeled states concentrates toward those that terminate at the central level, we will take the model $\Delta(n, \frac{1}{2}, \ldots, \frac{1}{2}) \equiv \Delta_{\frac{1}{2}}$ to benchmark against. Such an algorithm has a probability lower bound at the complete state as follows:

$$\tilde{P}_{\frac{1}{2}} \equiv \min_{C \in C_n} P_{\frac{1}{2}}(C) = P_{\frac{1}{2}}(C_n^*) = (\frac{1}{2})^{\sum_{d=2}^{n} \binom{n}{d}} = (\frac{1}{2})^{2^n - n - 1}. \tag{5.3}$$

We note Kahle's construction was never claimed to be useful as a fast and broad sampler on C_n. However, from the class of both descriptive and generative algorithms, and as a producer of a maximum entropy ensemble, it is an incredibly simple and natural inductive construction that we feel would serve as a reasonable baseline to compare against our random sampler on this space with the goal of rounding small probability sets in mind.

5.5 The Balanced Algorithm

Our goal is to sample across geometrically inequivalent states with better mixing than the $\Delta_{\frac{1}{2}}$ model. To this end, we define three key properties that we wish our model to satisfy as heuristics that we intuitively suggest would promote more rapid and broad sampling.

1. Any isolated node such that $|\alpha_d^*| = 1$ should be given a probability of appearance of $p_d = \frac{1}{2}$. At this level in the induction, there are only two possible states that can be selected as the rest of the structure is already fixed. Each state should be given equal probability, as from the vantage of the current step in the algorithm, there is no differentiating property of either state that would induce a bias in the probability. For example, the highest dimension simplex should always have $p_n = \frac{1}{2}$.

2. The power law behavior of binomials in the probabilities should be avoided, which may also aid the associated issue in over-selecting multiple isomorphic states.

3. The completely disconnected state on n nodes, C_n^o, should have the same probability of occurrence as C_n^*. This heuristic aims to re-balance the combinatorial effects of the intimate coupling between nodes at different levels due to simplicial closure, since not including any nodes at $d = 2$ generates C_n^o, while in a construction like Δ, all nodes in $G[C]$ must be independently kept to generate C_n^*, regardless of what probabilities are assigned to each level or even each individual simplex.

To accomplish this, we first note that we will work inversely from Kahle's inductive constructive model and instead consider an equivalent inductive destructive model. Instead of starting from C_n^o, we start from C_n^* and remove nodes starting at $d = 2$ and work upwards in level. This is equivalent to sampling on the space $\mathbb{F}$, inductively building the boolean mask starting from the all-ones vector. This is computationally easier, as instead of checking the complicated closure conditions at each node we would like to place, we only have to solve for the complete graph state once (which involves finding all complete subgraphs on n nodes, the NP-complete clique problem), save this state to disk, and reference it at will. To retain the simpliciality, upon removing node α_d, one simply removes the unique directed tree associated with α_d as a starting node, which is a linear-time computation. In practice, this amounts to inductively applying a logical AND between the active masking function F and the logical vector NOT[IN TREE] for the removed head node.

Theorem 1. *Let* $\vec{P}_d = [P_{d_0}, P_{d_1}, \ldots, P_{d_{\binom{n}{d}-\hat{d}}}]$ *be a probability vector such that* $\|\vec{P}_d\|_1 = 1$ *with* P_{d_i} *denoting the probability that* i *nodes are chosen uniformly at random and removed from level* d*, and* $\hat{d}$ *indicating the number of nodes already removed from level* d *due to directed tree pruning from lower level removals.*

$$\begin{aligned} P_{d_{i\neq 0}} &\equiv P_d = \frac{1}{1 + \sum_{k=d}^{n} \binom{n}{k} - \hat{k}} \\ P_{d_0} &= 1 - (\binom{n}{d} - \hat{d}) P_d \end{aligned} \tag{5.4}$$

satisfies all properties of conditions 1, 2 and 3.

Proof. We first note that $0 < P_d \leq \frac{1}{2} \forall\, d$, as the total node set is positive, finite, and the maximum is achieved in condition 1 as proven below. Additionally, $\hat{d}$ is defined such that $\binom{n}{d} - \hat{d} \in \mathbb{N}$. We need to show that $0 < P_{d_0} < 1$ to conclude that this is a valid probability vector element.

We only seek to show that $(\binom{n}{d} - \hat{d})P_d < 1$, as we already know this quantity is strictly positive due to above arguments. It should be clear that P_d is inversely proportional to the total number of nodes left in the state $G[C]$ at step d in the inductive construction (+1). The combinatorial prefactor is simply the total number of nodes remaining on level d, which must be less than or equal to the total number of nodes in the state. Hence, our claim is justified.

Lastly, we can safely conclude that $\|\vec{P}_d\|_1 = 1$ by our construction of $P_{d_0} = 1 - (\binom{n}{d} - \hat{d})P_d$.

To show that this distribution satisfies the condition 1, it can be seen from the definitions that

$$|\alpha_d^*| = 1 \Leftrightarrow \hat{k} = \begin{cases} \binom{n}{d} - 1 & k = d \\ \binom{n}{k} & k > d \end{cases}.$$

Hence,

$$\begin{aligned} P_d|_{|\alpha_d^*|=1} &= \frac{1}{1 + \binom{n}{d} - \binom{n}{d} + 1 + \sum_{k=d+1}^{n} (\binom{n}{k} - \binom{n}{k})} \\ &= \frac{1}{2}\,; \\ P_{d_0} &= 1 - P_d = \frac{1}{2}\,. \end{aligned} \tag{5.5}$$

Condition 2 is satisfied by algorithmic construction. In choosing groups of i nodes uniformly at random to remove from level d, we trade the power-binomial behavior in the probabilities that grow with the number of total nodes in $G[C]$ for a polynomial-binomial behavior that grows with the number of *levels* instead. Additionally, the Δ model will always pick out a specific labeled $G[C]$ insensitive to the number of isomorphic reachable graphs. In the balanced model, we select from a class of graphs with a certain number of simplicial elements. Although there can also be many such graphs that are not isomorphic but have

the same number of elements of given dimensions, we sample the number of elements per level uniformly instead of with product probabilities, giving a key advantage in sets of small probability measure as will be seen exactly in the case of $n = 3$ shown in Section 5.6.

Satisfying condition 3 requires that the removal of all nodes at the edge level have the same probability as removing no nodes at any level:

$$P_2 = \prod_{d=2}^{n} P_{d_0} \,. \tag{5.6}$$

On the left-hand side,

$$\begin{aligned} P_2 &= \frac{1}{1 + \sum_{k=2}^{n} \binom{n}{k} - \hat{k}} |_{\hat{k}=0} \\ &= \frac{1}{1 + \sum_{k=2}^{n} \binom{n}{k}} \\ &= \frac{1}{2^n - n} \,. \end{aligned} \tag{5.7}$$

On the right-hand side,

$$\begin{aligned} \prod_{d=2}^{n} P_{d_0} &= \prod_{d=2}^{n} (1 - (\binom{n}{d} - \hat{d}) P_d) |_{\hat{d}=0} \\ &= \prod_{d=2}^{n} (1 - \frac{\binom{n}{d}}{1 + \sum_{k=d}^{n} \binom{n}{k}}) \\ &= \prod_{d=2}^{n} \frac{1 + \sum_{k=d}^{n} \binom{n}{k} - \binom{n}{d}}{1 + \sum_{k=d}^{n} \binom{n}{k}} \\ &= \prod_{d=2}^{n} \frac{1 + \sum_{k=d+1}^{n} \binom{n}{k}}{1 + \sum_{k=d}^{n} \binom{n}{k}} \\ &= \frac{1}{1 + \sum_{k=2}^{n} \binom{n}{k}} \\ &= \frac{1}{2^n - n} \,. \end{aligned} \tag{5.8}$$

Comparing Eq. 5.7 and 5.8 demonstrates equality.

□

We mention that the existence of such a solution to these constraints is very nontrivial. For example, the balancing condition 3 can be shown to have no solution for the $\Delta_{\frac{1}{2}}$ construction for $n > 2$ as equal probability of removal and acceptance would clearly require a solution to an equation of the form

$$\begin{aligned} x &= xy \\ \text{s.t.} \qquad & 0 < \{x, y\} < 1\,. \end{aligned} \tag{5.9}$$

Since $n = 2$ doesn't admit more than one probability level (equivalently let $y = 1$), the conditions admit the trivial solution $x = \frac{1}{2}$.

For any constant probability model Δ_x on n roots enforcing the balancing condition 3 and condition 1 requires the probabilities to be roots of polynomials of the form

$$\begin{aligned} x^{\frac{n(n-1)}{2}} &= \frac{1}{2}(1-x)^{2^n-n-2} \\ \text{s.t.} \qquad & 0 < x < 1\,. \end{aligned} \tag{5.10}$$

The computer algebra package Mathematica suggests that this equation does not have any rational solutions for x with $n > 2$, indicating that there is likely no natural combinatorial factor that can be attributed to the probability weighting for this model, and relaxing condition 1 does not help.

For any a generic $\Delta(n, p_2, \ldots, p_n)$ model, our constraints require parameters that satisfy the following equation:

$$\begin{aligned} p_2^{\binom{n}{2}} &= \frac{1}{2}\prod_{d=2}^{n-1}(1-p_d)^{\binom{n}{d}} \\ \text{s.t.} \qquad & 0 < p_d < 1\,. \end{aligned} \tag{5.11}$$

In the generic case with independent level probabilities, rational solutions only appear to exist if we remove condition 1; however, this may lead to an large imbalance in the state probabilities for states that are otherwise inductively identical—taking us further from our goal of uniformly sampling the geometric states. It is clear that although possible in theory

to balance this algorithm, it requires finding numerical roots at each order and tuning the probabilities to best counteract the power behavior in the sampling, unlike the version we have presented that has closed-form analytic balancing and naturally handles the power structure.

We conclude this section with the probability of finding a given labeled state using this algorithm. As mentioned, this algorithm samples from classes of complexes with certain numbers of objects per skeletal level. In order to relate these probabilities to a specific geometric state, one must know how these classes decompose into nonisomorphic graphs, as well as the relative sizes of the equivalence classes, introducing an additional combinatorial factor.

Let the set of all graph isomorphisms between representations G of a geometric state C be denoted $\mathrm{ISO}(G[C])$ such that the cardinality of this set gives the number of equivalent ways of representing C under Def. 1.

At each inductive step, let i_d nodes be removed from level d out of the total number of available nodes.

The fraction given by the number of labeled ways the selection can be made, weighted by the number of equivalent states at that level, yields the leveled combinatorial factor. Multiplying these factors over the full induction yields the resulting combinatorial factor $\xi(C)$ for achieving a particular geometric state:

$$\xi(C) = |\mathrm{ISO}(G[C])| \prod_{d=2}^{n} \frac{1}{\binom{\binom{n}{d}-\hat{d}}{i_d}} \,. \tag{5.12}$$

However, since $|\mathrm{ISO}(G[C])|$ is not known in advance, we can only compute probabilities analytically for labeled states as this breaks the symmetry factor. Thus, the combinatorial factor becomes

$$\xi_L(C) = \prod_{d=2}^{n} \frac{1}{\binom{\binom{n}{d}-\hat{d}}{i_d}} \,. \tag{5.13}$$

It is this quantity that we will use in our comparisons to the Δ model, as they both consider specific labeled states. In practice, the geometric probabilities are larger, with the

labeled probabilities providing a lower bound.

Let $\{j\}$ be a boolean sequence representing whether any nodes were masked from C_n^*, with $j_d \equiv \{j\}_d = 0$ as an indicator that no nodes were removed from level d. In terms of our boolean function F, the elements correspond to a NOT[ALL[F_d]] operation over the level subsets $F_d \subset F$. The probability of finding a labeled state is given by the following expression:

$$P(C) = \xi_L(C) \prod_{d=2}^{n} (P^d)^{\delta^1_{j_d}} (P_0^d)^{\delta^0_{j_d}} , \tag{5.14}$$

where δ^a_b is the Kronecker delta.

5.6 Properties of the Balanced Algorithm and Simulation Results

This algorithm samples across a weighted space of paths for inductively building a given state, as opposed to building a specific state itself. In the case where each such path yields a unique state up to relabeling, this algorithm will produce the uniform distribution on the space of complexes. Such a condition is only true for $n = \{2, 3\}$ where $\xi(C) = 1 \, \forall \, C \in C_{\{2,3\}}$, and is illustrated in a direct comparison with the $\Delta_{\frac{1}{2}}$ benchmark in Fig. 5.2. This graph bins the multiplicities for which each geometric state was sampled, subtracted by the mean multiplicity to give residuals, and normalized by the total number of samples. The bins themselves do not match to the same geometric state between the two algorithms, but map to the first encountered representative of a given state. One can clearly see the uniform sampling from the balanced algorithm, although given the number of total samples, both algorithms find all 5 geometric states. All simulations were performed using MATLAB.

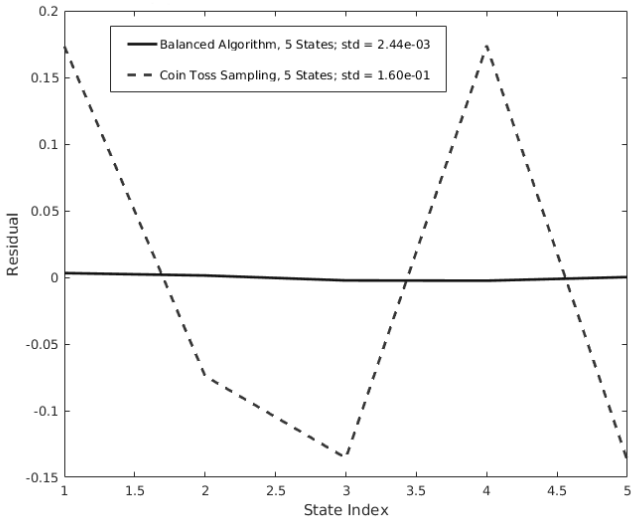

Figure 5.2: Multiplicities Residuals of Unique Geometric States on 10000 Samples Drawn From C_3, Linearly Interpolated

However, for $n = 4$ and higher, there exist nonisomorphic graphs with the same number of simplicial elements in each skeleton. This introduces a nonuniform combinatorial factor that is not possible to account for at the time of writing due to the fact that there is no analytic algorithm for predicting the number of such inequivalent graphs and their combinatorial multiplicities. Of course, since we can explicitly compute the probabilities for generating a labeled state, we mention that this sampler can be equipped with a Metropolis filter to re-weight the probabilities to produce a uniform sampling on labeled states.

We now examine the raw probabilities for sampling a unique labeled state. Directly comparing the minimal probability in the $\Delta_{\frac{1}{2}}$ model with the equivalent complete state in the balanced model indicates that this state has a much greater probability of occurrence:

$$\frac{1}{2^n - n} > (\frac{1}{2})^{2^n - n - 1} \; \forall \; n > 2 \, . \tag{5.15}$$

To indicate whether the new algorithm has balanced the probabilities at large and removed sets of extremely suppressed measure would require looking at the minimal probability

bound for this algorithm and comparing it to C_n^* as generated from $\Delta_{\frac{1}{2}}$. Here, we must use the labeled combinatorial factor ξ_L for adequate comparison. Due to the balancing, the probabilities are minimized toward the half-graph state, as this maximizes the binomial coefficients at each level with many combinatorial possibilities equivalent to the removal of certain numbers of nodes. As we would like a lower bound, we set $\hat{k} = 0 \, \forall \, k$. Even though we are removing approximately half of the nodes at each level, to maximize the binomial contribution, maintaining the full combinatorial degree of each level will further decrease the probabilities.

In total, this gives an estimate for a lower bound of the following form:

With

$$E(x) = \begin{cases} \frac{x}{2} & \mod (x, 2) = 0 \\ \frac{x+1}{2} & \mod (x, 2) = 1 \end{cases},$$

$$\tilde{P} = \min_{C \in C_n} P(C) \approx \prod_{d=2}^{E(n)} \frac{1}{\binom{\binom{n}{d}}{E(\binom{n}{d})}^{\frac{1}{1+\sum_{k=d}^{n}\binom{n}{k}}}} . \tag{5.16}$$

Numerical analysis confirms that $\tilde{P}_{\frac{1}{2}} \leq \tilde{P}$ for reasonable values of n before they become numerically unstable due to the combinatorial explosion, as illustrated in Fig. 5.3. It is immediately apparent that this algorithm has a much stronger probability behavior and actively works against the suppression found in a product model.

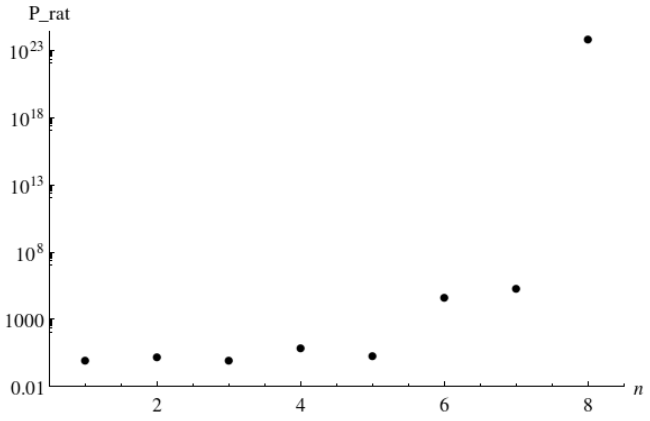

Figure 5.3: A Log-Plot of the Ratio $\frac{\tilde{P}}{\tilde{P}_{\frac{1}{2}}}$ as a Function of the Number of Roots n

Lastly, we advertised that the combinatorial balancing would allow for a broader access of states. Below we provide some simulation results to illustrate this property. Fig. 5.4 shows the number of unique geometric states encountered while sampling C_6 for a variety of sampling lengths. We can see that the balanced algorithm samples states at a faster rate than the $\Delta_{\frac{1}{2}}$ benchmark test. This is again demonstrated in Fig. 5.5, where 50000 samples were drawn on C_5. The balanced algorithm has appeared to converge, while the $\Delta_{\frac{1}{2}}$ benchmark has yet to find all of the inequivalent states. Naturally, the states with higher probability of being encountered were among the first to be sampled, explaining the correlation between the large initial fluctuations in the two algorithms given the first-representative binning process. However, the multiplicity fluctuations are much smaller for the balanced algorithm, indicating that the goal of heuristically rounding the space of state probabilities has been preliminarily accomplished by this algorithm.

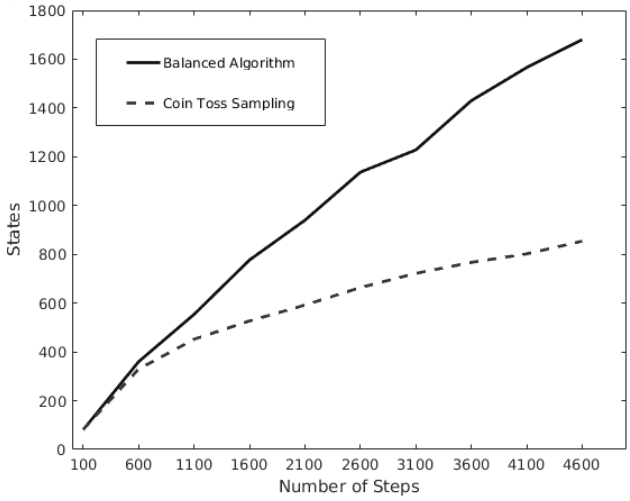

Figure 5.4: Number of Unique Geometric States While Sampling C_6 as a Function of the Sample Size, Linearly Interpolated

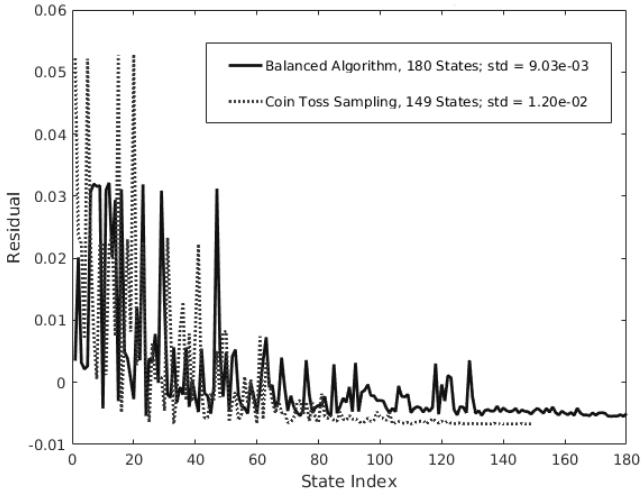

Figure 5.5: Multiplicity Residuals of Unique Geometric States on 50000 Samples on C_5, Linearly Interpolated

5.7 Local Random Walks

The algorithm introduced in Sec. 5.5 can be naturally used to perform an ergodic walk on the ASC space. We can jump from any state to another without a barrier as there is no dependence on the current state to restrict the space of next available states. This is a desirable feature from the perspective of sampling on the full space, as there are no regions of low conductance in the state space where our 'walk' can become trapped. However, when a Metropolis filter is utilized, the fact that this sampler can introduce transitions between arbitrary configurations may be a detriment to the acceptance rate if the filter is not naturally tuned to the intrinsic sampling probabilities of the walk. A local random walk between nearby configurations would be more likely to permit an acceptance with respect to a Metropolis filter, and as a result, may sample the full space faster. We would still like to be able to make this local random walk reversible, however, to ensure the Markov property. However, on the ASC space, the closure constraints make constructing a reversible local random walk very difficult. It is even still difficult to find *any* local random walk where one can compute forward and backward transition probabilities in order to force the walk to be reversible with respect to an additional Metropolis filter. In the following sections, we illustrate one example of a local random walk in the ASC space, and compare its properties to our global sampler.

5.8 A Local Random Walk on Abstract Simplicial Complexes

Our goal is to create a local random walk that has more favorable acceptance ratios for a Metropolis filter that is in some way sensitive to the topological structure of the current ASC. To that end, we define 'local' with respect to a new metric on the ASC space that is restricted to a unidirectional walk away from a given state.

Definition 3 (Unconstrained Nodes)**.** *Given an ASC in the graph representation $G[C]$, we define an 'unconstrained node'* u *as one that can be freely added or removed without requiring or destroying additional containment structure.*

An unconstrained node is 'removable' if is has no children and is itself not a root (as the we hold the roots fixed in C_n).

An unconstrained node is 'addable' if it is a member of $C_n^* \setminus C$ (the complete graph with the current state excluded) that has all of its parents in C.

We work with unconstrained nodes for two reasons. Foremost, we would like to have a walk that admits a range of local movement as opposed to simply a one step nearest-neighbor walk on individual simplices. If we admit moves that can add or remove an arbitrary number of nodes within the state space, one needs to worry about the closure constraints. These constraints will make it very difficult to generate a walk that has computable probabilities for reversibility, as the number of admissible additions or removals would be dynamic with each sub-step within the same transition move, and there can be multiple paths with different probabilities that could lead to the same state. We want to restrict down this capability, but still admit larger jumps through the state space. Hence, we work with the space of unconstrained nodes as pure additions or removals within this space will prevent such issues from arising and admit a walk with computable probabilities. The restriction that nodes are only added or removed in a single step additionally guarantees that we do not have any closed loops within our multi-step walk for a given transition.

Our notion of local distance is therefore the number of added or removed nodes in a given transition step, actioned by a binary flip on the boolean function representing C.

The algorithm mimics an exponential ball walk with respect to this distance measure. First, we compute the total number of nodes one could maximally flip on the state space. From this set, we establish a normalized probability function based on an exponential decrease in probability for larger numbers of binary flips. We decide to either add or remove nodes in a given transition. Once this choice is made, we compute all addable/removable nodes U for the current configuration. We select a distance δ to move based on the fixed probability measure. If that distance takes the state outside of the state space or beyond the number of admissible adds/removes, then the algorithm resets until an admissible move

is found—this is our rejection sampling step similar to a ball walk on the edge of the state space. Further logic handles the complete state and the state with only roots to speed up the process in those cases. Once a good distance is accepted, a uniformly random selection of those unconstrained nodes $u \in U$ have their entries flipped in the boolean representation. The forward and backward probabilities are symmetric with respect to the exponential distance weighting, as this is not dependent on the state itself. Therefore, a Metropolis filter would only need to account for the uniform selection step, producing a combinatorial factor of

$$\frac{P_B}{P_F} = \frac{\binom{|U_B|}{\delta}}{\binom{|U_F|}{\delta}} \,. \tag{5.17}$$

5.9 Computational Results

Since our sampler now has local correlations, it becomes necessary to characterize more carefully the efficiency of the random walk and breadth of sampling. We present two extreme situations for the initial start of the walk: beginning at a corner of the state space, C_n^*, and beginning at a 'central' state consisting of roughly half of the available simplices being activated. We examine both the multiplicity residuals as before, as well as the autocorrelation length.

To characterize the autocorrelation length, we use an initial convex sequence method that involves the greatest common minorant [28]. First, we implement a Metropolis filter utilizing Eq. 5.17 such that our samples can be expected to be i.i.d. To measure autocorrelation, we compute the signed displacement of a transition between two states C and C' as the difference in the sums of their boolean representations:

$$\delta = \|C\|_1 - \|C'\|_1 \,, \tag{5.18}$$

where $|\delta|$ still corresponds to the number of binary flips between the two, as discussed in the algorithm. We then look at the cumulative sum of the time sequence of δ_i values for each

step i in the walk. This gives some sense of a 1-dimensional projection of the random walk through the ASC space, making it a natural random variable to compute autocorrelations with.

Let an estimator for the sample mean on s samples be denoted

$$\hat{\mu}_s = \frac{1}{s}\sum_{i=1}^{n} \delta_i \,. \tag{5.19}$$

A natural estimator for the auto-covariance function at lag k is given by the following:

$$\hat{\gamma}_s = \frac{1}{s}\sum_{i=1}^{n-k} (\delta_i - \hat{\mu}_s)(\delta_{i+k} - \hat{\mu}_s) \,. \tag{5.20}$$

The greatest convex minorant at lag k,

$$\Gamma_k = \gamma_{2k} + \gamma_{2k+1}, \tag{5.21}$$

is a strictly positive, decreasing, and convex function for a reversible Markov chain. Therefore, examining our estimator $\hat{\Gamma}_k$ for the point at which it becomes nonpositive indicates the lag where we encounter autocorrelation. Due to the dependence on twice the lag, our autocorrelation is related to $2k'$ when $\hat{\Gamma}_{k'} \leq 0$.

We can see in Fig. 5.6 that the local random walk started from a central state, upon re-weighting with the Metropolis filter, produces autocorrelation out to about 16 steps, and the walk has a natural rejection rate on the order of 50%.

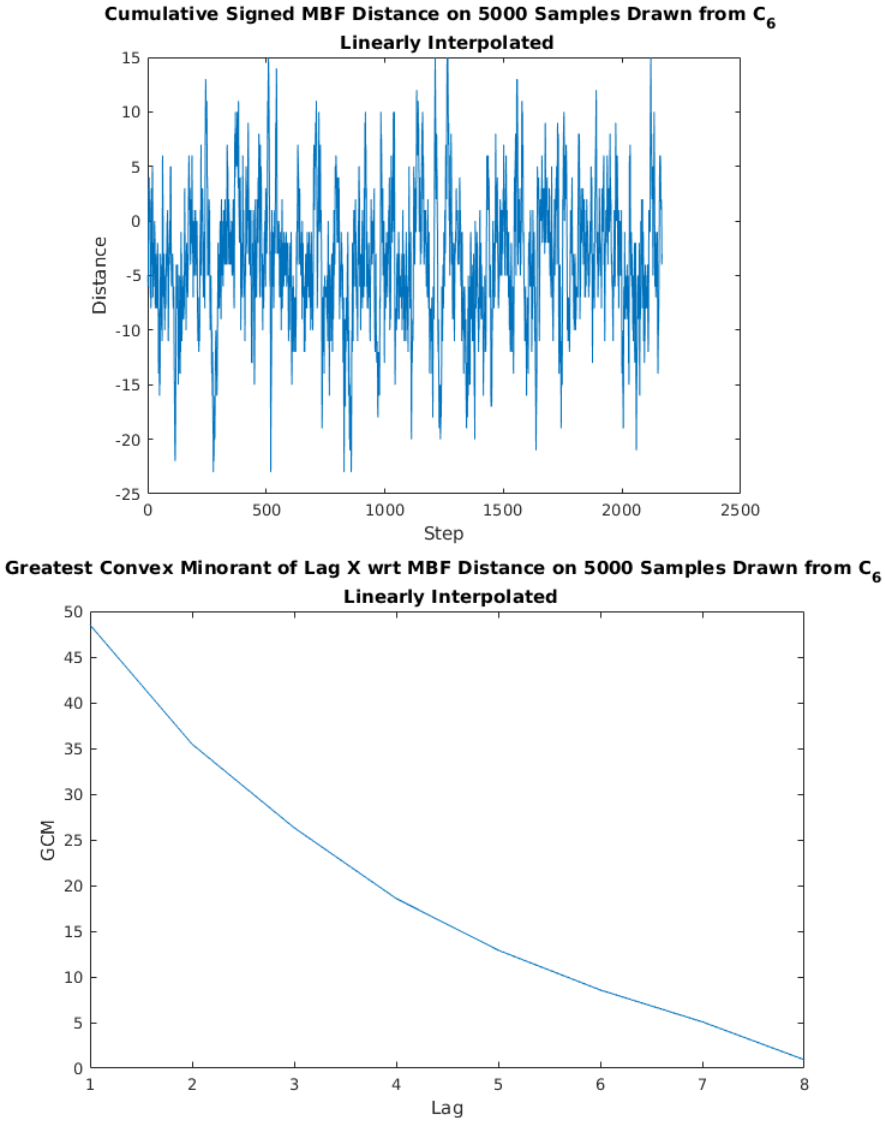

Figure 5.6: Autocorrelation Statistics for a Random Walk on C_6 with 5000 Steps, Starting from a Central State

Fig. 5.7 which was produced starting from a corner state tells not much of a different story, which indicates that the edges in the state space are not incredibly narrow, and that this random walk is good at working its way out of those corners. We see less than double the autocorrelation, which is not unexpected due to the time spent in the region of small state

density. A burn-in process would reduce this down to toward the autocorrelation lengths found in the central case.

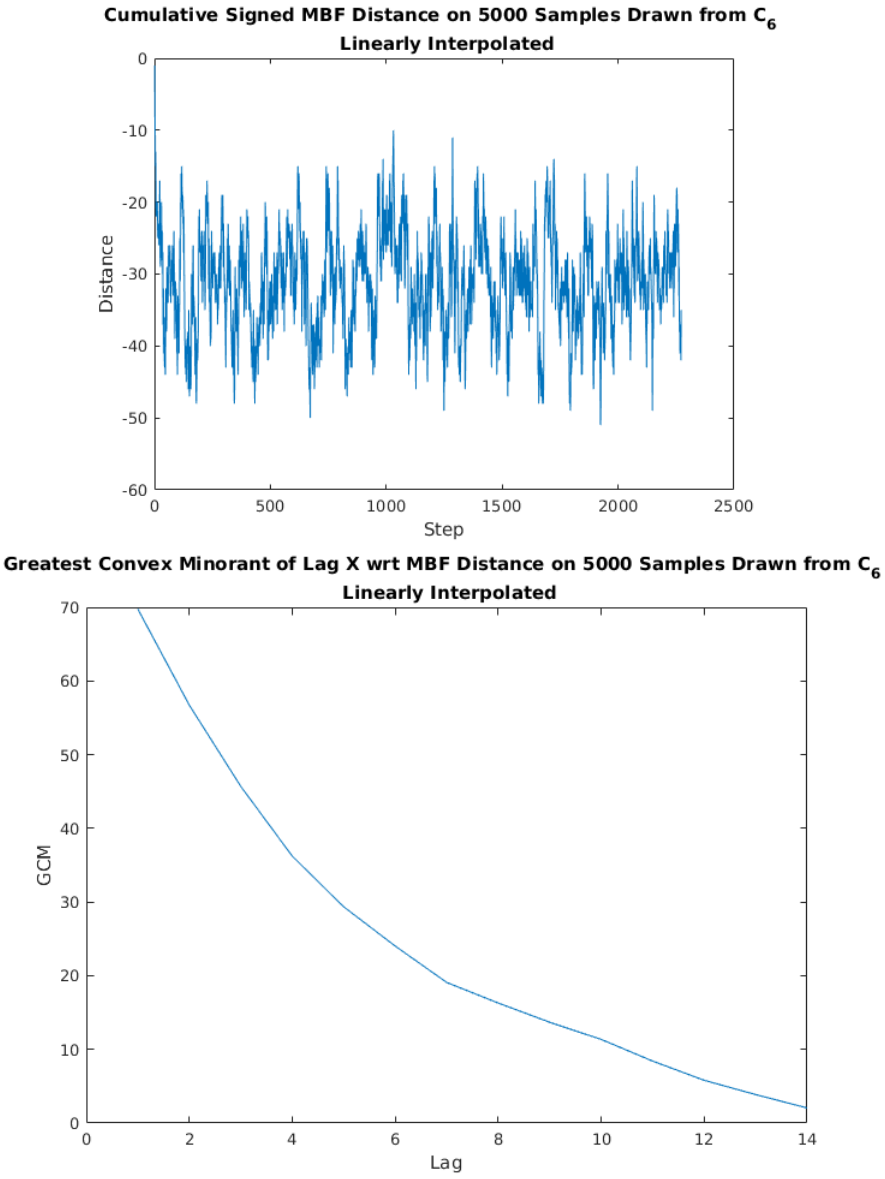

Figure 5.7: Autocorrelation Statistics for a Random Walk on C_6 with 5000 Steps, Starting from a Corner State

We lastly compare the efficiency of all of these algorithms for sampling geometrically

unique states. As seen in Figs. 5.8 and 5.9, the local random walk performs remarkably better, sampling more states with less accepted steps. This lends credence to the notion that the best sampler on this space would likely be a linear combination of the two Markov chains. Since such a construction still retains its theoretical properties, we can achieve the best of both algorithms by choosing to perform a local walk with some large probability to reap the rewards of the rapid sampling, while occasionally using the balanced sampler to avoid regions of narrow conductance bands and to promote ergodicity and large nonlocal transitions.

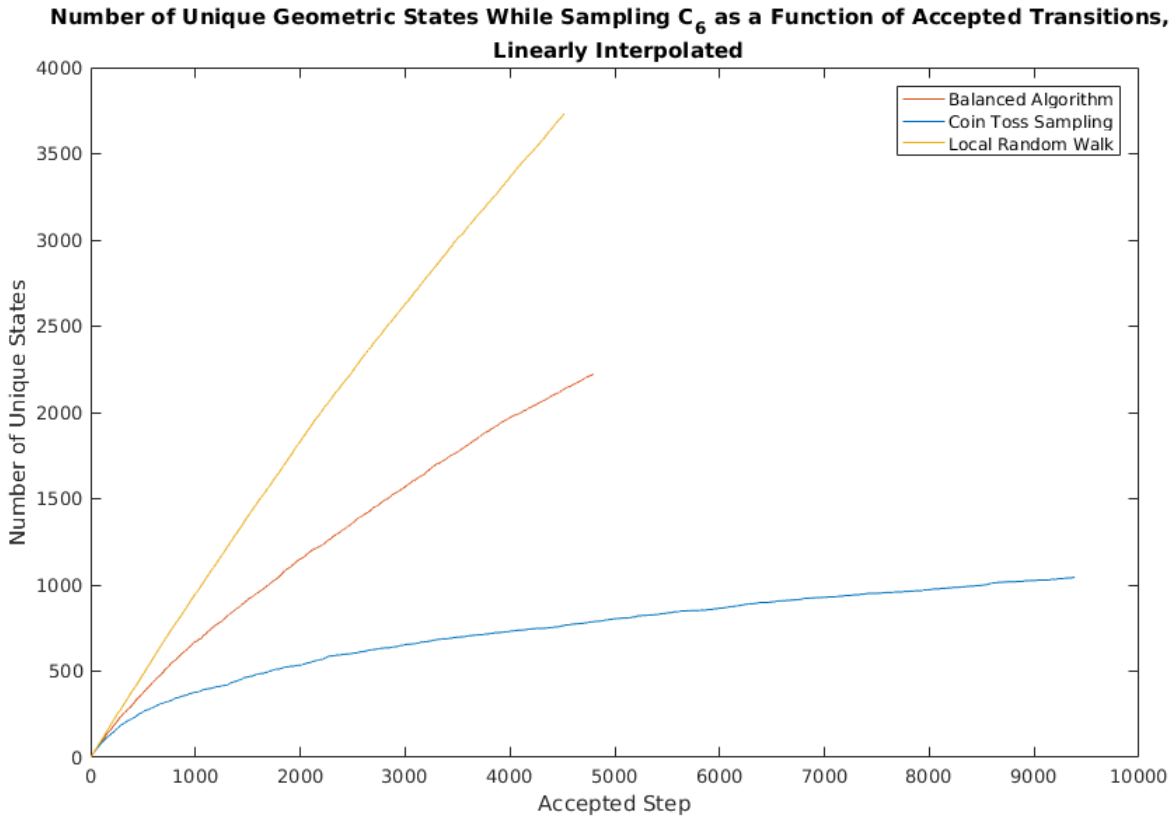

Figure 5.8: A Comparison of the Unique Geometric States Sampled on C_6 as a Function of Accepted Transitions for All Three Samplers

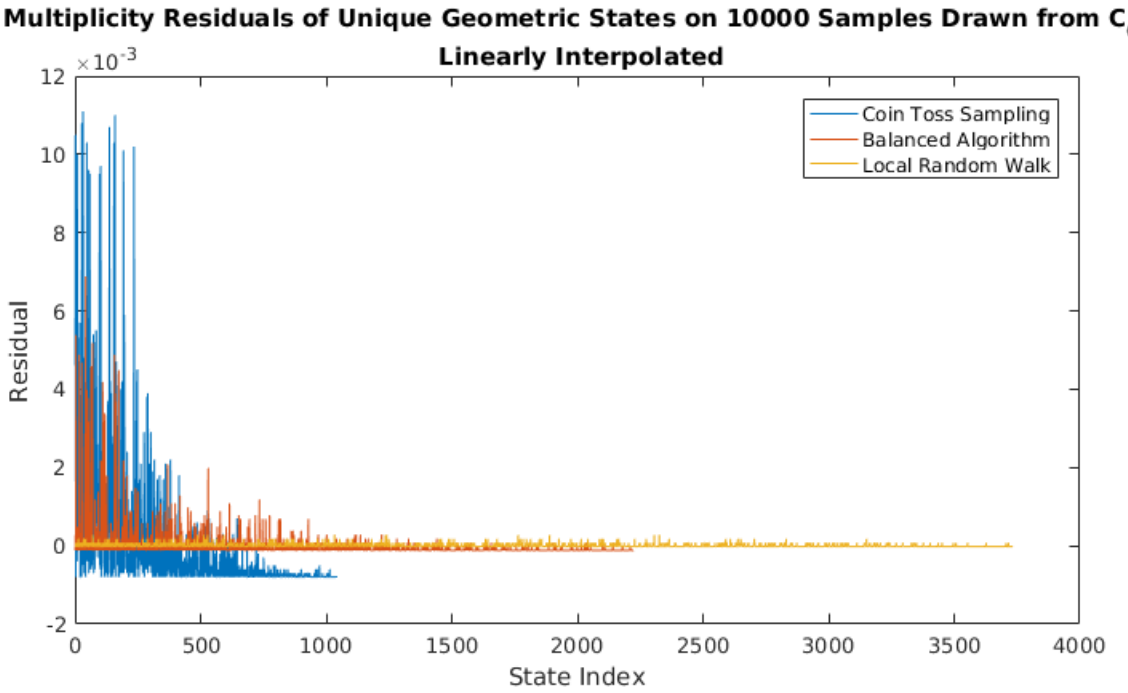

Figure 5.9: A Comparison of the Multiplicity Residuals of Unique Geometric States Sampled on C_6 for All Three Samplers, Linearly Interpolated

5.10 Discussion on the New Samplers

As is the case with a wide variety of combinatorial spaces, it is often very difficult to develop a sampling procedure with transition probabilities that can *a priori* sample such that the uniform distribution is the stationary distribution without the use of a Metropolis filter. In the case of abstract simplicial complexes, the unknown isomorphism classes of configurations make this problem seemingly intractable. We have introduced an algorithm that uses three simple principles to attempt to re-balance the sampling such that the algorithm more readily samples inequivalent configurations with a wide breadth across the space. Our analytical results show that this algorithm has a worst case lower-bound on state probabilities that is larger than the equivalent sampling through a uniformly weighted Kahle process, which we used as an unoptimized benchmark. Our simulations confirm that a direct comparison

between the two algorithms favors the balanced algorithm when attempting to sample across the geometric space of states.

We have also discussed a local random walk that can be made reversible. The advantage of this walk is to increase the acceptance rates for a Metropolis filter when sampling nearby states as opposed to large jumps in the state space, and we have illustrated through simulation its efficiency in also sampling from a wide range of states in the ASC space. However, in some applications with Metropolis filters, this walk may be sensitive to trapping regions, as it is not able to explore any possible configuration in a single transition step. Thus, a combination of our local walk and the balanced sampler can be used to promote ergodicity and rapid sampling.

Future work toward finding a better generative algorithm for sampling across equivalence classes of large random abstract simplicial complexes while maintaining analytical control is necessary in order to begin to probe the very large space of states. With a variety of applications on the horizon, we anticipate this problem being approached from a broad range of perspectives, and we hope to have provided some insight through some practical, simple algorithms that accomplish the first steps toward this task.

Chapter 6

COMBINATORIAL HIVES

6.1 Littlewood-Richardson Coefficients

We now step away from the physics of quantum gravity, and into the second portion of this manuscript: representation theory and combinatorial hives. We will first introduce the construction that we investigated, and provide some historical context for the utility of such a mathematical object.

Throughout physics, representation theory plays a crucial role—from understanding the particle content of the standard model, to basic questions in quantum mechanics about adding angular momenta and spin. One should recall the use of SU(2) representation theory for the latter, where the process of combining different spins involves Clebsh-Gordan coefficients that give the weightings of the irreducible representations after decomposition [60]. Here, we explore a very similar structure and associated combinatorial coefficients: Littlewood-Richardson coefficients.

In 1934, D. E. Littlewood and A. R. Richardson formulated a combinatorial rule for the multiplication of Schur polynomials [39]. Schur polynomials form a linear basis for the space of symmetric polynomials, which are polynomial functions where the interchange of any two variables results in the same function.

With the following decades producing a wide variety of proofs of this rule, a vast scope of applications throughout combinatorics and representation theory were discovered, with natural numbered Littlewood-Richardson coefficients (LRC) $c_{\mu\nu}^{\lambda}$ appearing in examples such as the symmetries of Young tableaux [63].

We will be concerned with the use of LRCs as the multiplicities in decompositions of tensor products of irreducible representations V on $\mathrm{GL}_n(\mathbb{C})$ for triples of dominant weights

(μ, ν, λ):

$$V^\mu \otimes V^\nu = \bigoplus_\lambda c_{\mu\nu}^\lambda V^\lambda \,. \tag{6.1}$$

For SU(2), the multiplicities of the half-integer labeled irreducible representations are either 1 or 0, and are given by the familiar integer-stepped Clebsh-Gordan series:

$$V^\mu \otimes V^\nu = V^{|\mu-\nu|} \oplus V^{|\mu-\nu|+1} \oplus \cdots \oplus V^{|\mu+\nu|} \,. \tag{6.2}$$

It becomes natural to ask under what conditions the LRC is non-zero based on the dominant weights. That is, when does a particular representation contribution to the decomposition? This is the context wherein Knutson and Tao (KT) introduce the 'hive' combinatorial model in their proof of the saturation conjecture, a conjecture that implies that satisfying a particular series of linear inequalities is actually a sufficient condition for the corresponding LRC to be positive [38]. We will now define the hive model and provide a pictorial example for intuition.

6.2 The Relationship Between Hives and LRCs

Consider a symmetric non-negative definite matrix M. Define a function $\sigma(M) \mapsto \mu$ which returns the spectrum μ of M, listed in weakly decreasing order.

We define the LR-Cone as the subspace of tuples (μ, ν, λ) such that there exists matrices M, N and $L = M + N$ with spectra given by $(\sigma(M), \sigma(N), \sigma(L)) = (\mu, \nu, \lambda)$. The KT proof demonstrates that if (μ, ν, λ) is an integer point in the LR-Cone, then the corresponding structure constant $c_{\mu\nu}^\lambda$ is greater than 0.

KT cast this condition into a geometric structure as follows: given a non-negative integer valued weakly decreasing 3-tuple of vectors (μ, ν, λ) each of length n, one can use these vectors to construct the boundary values of a triangular hive, illustrated in Fig. 6.1, that maps onto the previous condition provided that

$$\|\mu\|_1 + \|\nu\|_1 = \|\lambda\|_1 \,. \tag{6.3}$$

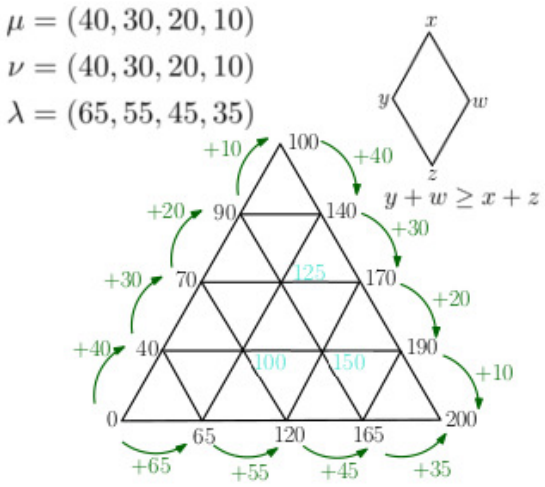

Figure 6.1: An example hive boundary setup and a possible interior labeling. A graphical representation of a rhombus inequality is shown for a vertical rhombus [50].

The triangle boundaries are built out of the cumulative sums of μ on the left edge starting at 0 on the left corner, $\mu+\nu$ continuing from the top into the right corner, and λ working from the left corner to the right corner, with Eq. 6.3 enforcing that the labels meet appropriately at the right corner. One can then tessellate the interior with triangles according to the lattice points of the boundary. If one assigns integer labels to the bulk interior points such that for every minimal rhombus in the triangulation

$$\sum (\text{Labels at the Obtuse Angles}) \geq \sum (\text{Labels at the Acute Angles}) \,, \tag{6.4}$$

then the resulting object is a member of the set $HIVE(\mu, \nu, \lambda)$. This condition enforces that the piecewise linear extension to the interior of the boundary triangle is a concave function.

The number of all possible integer hives with these fixed boundaries remarkably yields the corresponding LRC for the tuple. Thus, our goal of determining whether the LRC is positive for a given set of weight vectors is mapped onto the problem of finding an integer hive prescribed in this fashion. Enumerating all such hives will actually give the LRC itself.

While polynomial time algorithms exist for fixed rank Lie groups, in general computing an

LRC is a $\#P$-complete problem [56][49]. Although $\#P$-complete complexity is related to a subset of decision problems in NP, it has been shown that fully polynomial-time randomized approximation schemes are often capable of producing an arbitrarily good estimate with high probability for problems in this class [35]. This prompts the search for efficient estimation algorithms, and integer sampling on the hive space provides an opportunity to perform such estimations.

Numerically finding one such configuration, if it exists, is a linear programming (LP) problem on the hive polytope defined by the rhombus inequalities and the boundary data. KT have shown that finding the maximal hive using a real valued LP can be guaranteed to give integer solutions, keeping the optimization within the HIVE space [38]. However, finding more than one solution can not be done so easily as a constrained integer programming problem. Instead, estimations of the HIVE volume prompt the need for a random walk on the HIVE space. Our goal will be to investigate a method of generating hives from their boundaries by optimizations on Hermitian matrix pairs, as well as developing algorithms for estimating Littlewood-Richardson coefficients based on estimations of the HIVE volume.

6.3 Hives from Hermitian Matrices

Danilov and Koshevoy (DK), in an effort to provide a more elementary proof of the Horn problem concerning the sums of spectra of Hermitian matrix pairs, proposed a conjecture on the space of Hermitian matrices for generating real valued 'hives' from an optimization process that would lend itself as an analytic continuation of the integer HIVE space [16]. This was the first explicit constructive conjecture for finding hive coefficients given two generating matrices, and they demonstrated that their conjecture holds true for select special cases: 2 and 3 dimensional matrices, and matrices which commute. Appleby and Whitehead (AW) later considered a modified version of this proposal for which they sketch a proof claimed to produce hives in general [5]. This would provide a novel mechanism for the exploration of hive geometries on spaces of matrix ensembles with a study of experimental observables such as the mean hive and its fluctuations, if one could find a suitable algorithm for actually

implementing the optimization. We reproduce the construction to establish notation.

The optimization is concerned with finding a map from a triple of $n \times n$ Hermitian matrices $(M, N, L = M + N)$ into hives with indexed entries H_{ijk}, $i = n - j - k$ in the sense of KT, where i and k are coordinate labels on the vertical and horizontal triangulation axes. Provided such a map exists, then the tuple of the spectra of the matrices, $(\sigma(M), \sigma(N), \sigma(L)) = (\mu, \nu, \lambda)$, will generate a hive with the same coefficients. As in the KT case for the integer valued hives, the rhombus inequalities will again be satisfied for hive points. For completeness, we explicitly list the inequalities referenced in Eq. 6.4 for the right-facing, left-facing, and vertical interior rhombuses, in that order.

$$\begin{aligned} H_{ijk} + H_{(i+1)(j-2)(k+1)} &\leq H_{(i+1)(j-1)k} + H_{i(j-1)(k+1)} \\ H_{ijk} + H_{(i+1)(j+1)(k-2)} &\leq H_{(i+1)j(k-1)} + H_{i(j+1)(k-1)} \\ H_{ijk} + H_{(i-2)(j+1)(k+1)} &\leq H_{(i-1)(j+1)k} + H_{(i-1)j(k+1)} \end{aligned} \tag{6.5}$$

Let W be an n-dimensional complex vector space with a p-dimensional subspace U and a q-dimensional subspace V such that $U \subseteq V$. We denote $\mathbb{F}_{pq}(W)$ to be the set of all pairs of subspaces (U, V).

We also establish a notation for orthogonal projection $\pi_U : W \to U$ such that a Hermitian operator M on W has an action on U given by $M|_U = \pi_u \circ M \circ \pi_u$.

Provided (M, N), the proposal by AW claims that the hive coefficients are generated from a maximization of traces over all possible subspaces as follows:

$$H_{ijk} = \max_{(U,V)\in\mathbb{F}_{k,(j+k)}} \left(tr(M|_V) + tr(N|_U)\right). \tag{6.6}$$

We note that this departs from the conjecture by DK, wherein the original proposal optimized over pairs of *mutually orthogonal* subspaces (U, U') of dimensions k and j where $k + j \leq n$. Here, AW optimize over the set of all pairs of subspaces (U, V) with the containment structure defined by $\mathbb{F}_{pq}(W)$. Of course, these ideas are not entirely distinct as one can

reduce to the DK conjecture by taking $U' = V \cap U_\perp$. It is the theorem as presented by AW that we will work with.

Although it appeared to be a constructive theorem, this optimization problem seems to not actually guarantee hives in all cases. We detail below the obstruction that we have noticed in the AW proof and illustrate numerical counterexamples to the theorem as local optima (that may or may not be global, but are not provably so). Nevertheless, we conclude that the construction is not rendered entirely ineffective as it does work in reduced cases, such as when M and N have compatible eigenstructures and frames.

6.4 Obstruction for the Subspace-Contained Optimization

In the process of showing that the Hermitian matrix construction satisfies the rhombus inequalities, AW use the following abridged argument: by finding the subspace pairs $(U^*, V^*), (U^{**}, V^{**})$ that independently maximize each term in the left side of the inequalities in Eq. 6.5, one can always form an orthonormal basis of the union $U^* \cup V^* \cup U^{**} \cup V^{**}$ such that the space can be again subdivided into subspaces that have the right dimensions for the subspace pairs (but not necessarily those that maximize the traces) $(U', V'), (U'', V'')$ of the right side of the inequalities. When the matrices M and N are projected into the new re-partitioned space, their traces will be at most equal to the hive coefficients of the obtuse components of the rhombus. As an explicit example presented in reference [5], look at the right rhombus inequality:

$$\begin{aligned}
H_{ijk} + H_{(i+1)(j-2)(k+1)} &= \max_{(U,V)\in F_{k,k+j}} (tr(M|_V) + tr(N|_U)) + \max_{(U,V)\in F_{k+1,k+j-1}} (tr(M|_V) + tr(N|_U)) \\
&= [tr(M|_{V^*}) + tr(N|_{U^*})] + [tr(M|_{V^{**}}) + tr(N|_{U^{**}})] \\
&= [tr(M|_{V'}) + tr(N|_{U'})] + [tr(M|_{V''}) + tr(N|_{U''})] \qquad (6.7) \\
&\leq \max_{(U,V)\in F_{k,k+j-1}} (tr(M|_V) + tr(N|_U)) + \max_{(U,V)\in F_{k+1,k+j}} (tr(M|_V) + tr(N|_U)) \\
&= H_{(i+1)(j-1)k} + H_{i(j-1)(k+1)} \,.
\end{aligned}$$

The first and last equalities come from the hive coefficient definition; the second equality

comes from the definition of the maximal subspaces; the penultimate inequality comes from the maximum principal. However, we claim that the central equality that accomplishes the re-distribution of subspaces is not always true.

The dimension counting arguments foremost do not strictly hold in the case when the subspace pairs have nontrivial overlap and the structures are generic. In this situation, it is not in general true that any reshuffling of basis elements from the first union space will guarantee that the subspaces on the right side of the inequality can be reconstructed while maintaining the total traces. We can certainly guarantee that the union of the bases for $(U^*, V^*), (U^{**}, V^{**})$ is equal to that of $(U', V'), (U'', V'')$ by dimension counting. But, if in order for the sums of traces to be equivalent, it is necessary for a shared dimension to be passed from one subspace pair to another, the second subspace pair will not change rank and this may cause a hive deficiency (a failure of a rhombus inequality) as the second subspace pair will not actually have the correct dimension.

Another way to see this obstruction manifest more clearly is that it is not generically true that the rearrangement of the subspaces will result in an invariant of the sum of the traces of M and N upon carrying out the new projections. This is the converse of the above case, wherein we can satisfy the proper subspace dimensionality, but there is no guarantee on the total trace sums. We will construct an example for which

$$[tr(M|_{V^*})+tr(N|_{U^*})]+[tr(M|_{V^{**}})+tr(N|_{U^{**}})] > [tr(M|_{V'})+tr(N|_{U'})]+[tr(M|_{V''})+tr(N|_{U''})] \tag{6.8}$$

may hold. This would infringe on the crucial inequality in Eq. 6.7 for the right-facing rhombus condition.

Consider $(n, j, k) = (5, 2, 3)$, a coefficient that admits a right-facing rhombus inequality. To make our argument even more apparent, we consider positive-definite Hermitian matrices. Using a subscript notation to describe the rank of the projections with tildes denoting different subspaces in the case of dimensional equivalence, we claim that

$$tr(M|_5) + tr(N|_3) + tr(M|_4) + tr(N|_4) \overset{?}{>} tr(M|_{4'}) + tr(N|_{3'}) + tr(M|_{5'}) + tr(N|_{\tilde{4}'})\,. \quad (6.9)$$

Recall the variational definition of the eigenvalues of a hermitian operator acting on an n dimensional vector space W: for spectra in weakly decreasing order $\sigma(M) = [\mu_1, \ldots, \mu_n]$ and for all k such that $0 < k \leq n$,

$$\max_{\substack{\dim(U)=k \\ U \subseteq W}} tr(M|_U) = \mu_1 + \cdots + \mu_k\,. \quad (6.10)$$

For the first trace on the left of Eq. 6.9, the subspace is maximal with respect to the vector space. This implies that the joint optimization between M and N breaks down, and we simply yield the summed spectra of M with the partial spectra of N:

$$tr(M|_5) + tr(N|_3) = \|\mu\|_1 + \nu_1 + \nu_2 + \nu_3\,. \quad (6.11)$$

Similarly, in the second optimization on the left side of Eq. 6.9 where the subspaces are identical, another reduction can be made directly to the eigenvalues of the summed matrices:

$$\begin{aligned} tr(M|_4) + tr(N|_4) &= tr((M+N)|_4) \quad (6.12) \\ &= \lambda_1 + \lambda_2 + \lambda_3 + \lambda_4\,. \end{aligned}$$

For the right side of Eq. 6.9, by a similar argument, we know that at most

$$tr(M|_{5'}) + tr(N|_{\tilde{4}'}) \leq \|\mu\|_1 + \nu_1 + \nu_2 + \nu_3 + \nu_4\,. \quad (6.13)$$

This is due to the fact that the subspaces are not guaranteed to be those that maximize the individual traces. We substitute the maximal values as the strongest attempt for our conjectured inequality to fail. This results in requiring that

$$\begin{aligned} tr(M|_{4'}) + tr(N|_{3'}) &\overset{?}{<} \lambda_1 + \lambda_2 + \lambda_3 + \lambda_4 - \nu_4 \\ &\overset{?}{<} \|\mu\|_1 + \|\nu\|_1 - \lambda_5 - \nu_4 \quad (6.14) \\ &\overset{?}{<} (\mu_1 + \mu_2 + \mu_3 + \mu_4) + (\nu_1 + \nu_2 + \nu_3) + (\mu_5 + \nu_5 - \lambda_5). \end{aligned}$$

It is easy to conceive of an example where this difference of the last term is 0, so we proceed with such a case:

$$\begin{aligned} \mu &= (40, 30, 20, 10, 2) \\ \nu &= (40, 30, 20, 10, 2) \\ \lambda &= (65, 55, 45, 35, 4) \end{aligned} \tag{6.15}$$

In an example like this, it would be therefore necessary for the traces to yield the partial spectra, or greater (which is not possible due to the positive definite assumption and the variational eigenvalue definition), for our claim to be false. However, it is not necessarily true that in nonmaximal or nonidentical subspaces that the joint optimization over the independent matrices M and N will yield the partial sums of their spectra over the constrained dimensions they are projected into, let alone subspaces that were only selected for their ranks as we have here. In fact, this is generically not the case. Such lower dimensional projections from the full vector space may therefore not yield equivalent traces and highly depend on the structure of the re-partitioning of the original total union space and the initial maximization.

One may ask what would happen in this example if the repartitioned subspaces *were* the precise subspaces that could produce the spectral sums, giving us equality in the tightest case. We show that this does not generically hold in this example due to reasoning similarly suggested in our first argument.

In order for the exception to hold, one would need to use the same subspaces produced in the maximizations on the left side of Eq. 6.9 for the right side (barring accidental degeneracies or special structures). That is, we would require equality of subspaces such that, in the least,

$$3 = 3' \,. \tag{6.16}$$

Since we are examining the case of a tight equality where we know we are already utilizing the maximizing subspaces, it also must be true (by the definition of the optimization over F_{pq}) that

$$3' \subset 4' \tag{6.17}$$

Thus, in order to enforce equality of traces, we must also have a guarantee that

$$3 \subset 4' \,, \tag{6.18}$$

which is not generically true as one subspace comes from the independent maximization of N while the other comes from the joint maximization of M and N (and yet still must yield the result of the independent maximization of M).

For matrices that do not have such an additional structure, our inequality in Eq. 6.9 is true, which violates the original equality used in Eq. 6.7 by AW to support their theorem.

This condition leads us to new matrix domains where the optimization *is* guaranteed to hold: matrices with the same eigenstructure ranking. Sorted diagonal matrices, or matrices for which $M = N$, are two examples of classes of matrices wherein this constraint will be automatically satisfied. Although these are more trivial classes than one would hope to study in general, it will still give some avenue to utilizing the optimization problem presented above in order to study hive structures.

6.5 Optimization Space Transformation for a Practical AW Implementation

Sampling over all such projections into the constrained subspaces as per the AW construction would be akin to an optimization problem on a flag manifold, or a collection of ordered sets of vector subspaces. This is a difficult process to accomplish algorithmically, and it could be considered a generalization of independent subspace analysis [51]. Instead, we introduce a map of the AW optimization problem into a numerically equivalent problem on a product space of Grassmannians, on which one can perform a Riemannian optimization scheme. We produce the analytic Euclidean gradients and Hessians necessary to implement a traditional gradient-descent or trust-region algorithm, which we can then transform to work on the product space and return the individual hive coefficients.

We begin by trivially turning our maximization into a minimization for the following

algorithm:

$$\begin{aligned} H_{ijk} &= \min_{(U,V)\in\mathbb{F}_{k,(i+k)}} -(tr(M|_V) + tr(N|_U)) \\ &= \min_{(U,V)\in\mathbb{F}_{k,(i+k)}} -(tr(\pi_V M \pi_V) + tr(\pi_U N \pi_U))\,. \end{aligned} \tag{6.19}$$

We introduce an explicit form for the projection with $\vec{\alpha}_i$ defined implicitly as follows:

$$\begin{aligned} \pi_a &= A(A^TA)^{-1}A^T \\ &\text{s.t.} \\ A &= \mathrm{col}(\vec{\alpha}_i)\,|\,i\in\{0,\ldots,\mathrm{rank}(a)\} \\ a &= \mathrm{span}(\vec{\alpha}_i)\,. \end{aligned} \tag{6.20}$$

Expanding out, we can now optimize over new variables:

$$H_{ijk} = \min_{\substack{A=\mathrm{col}(\vec{\alpha}_i)\,|\,V=\mathrm{span}(\vec{\alpha}_i) \\ B=\mathrm{col}(\vec{\beta}_i)\,|\,U=\mathrm{span}(\vec{\beta}_i)\subseteq V}} -(tr(A(A^TA)^{-1}A^TMA(A^TA)^{-1}A^T)+tr(B(B^TB)^{-1}B^TNB(B^TB)^{-1}B^T))\,. \tag{6.21}$$

Now we decompose A into the subspace containing U and any orthogonal space, $A = \begin{bmatrix} B & \tilde{A} \end{bmatrix}$:

$$\begin{aligned} H_{ijk} = \min_{\substack{\tilde{A}=\mathrm{col}(\vec{\alpha}_i)\,|\,\mathrm{span}(\vec{\alpha}_i)\perp U \\ B=\mathrm{col}(\vec{\beta}_i)\,|\,U=\mathrm{span}(\vec{\beta}_i)\subseteq V}} & - (tr(\begin{bmatrix} B & \tilde{A} \end{bmatrix}(\begin{bmatrix} B & \tilde{A} \end{bmatrix}^T\begin{bmatrix} B & \tilde{A} \end{bmatrix})^{-1}\begin{bmatrix} B & \tilde{A} \end{bmatrix}^T M \begin{bmatrix} B & \tilde{A} \end{bmatrix}(\begin{bmatrix} B & \tilde{A} \end{bmatrix}^T\begin{bmatrix} B & \tilde{A} \end{bmatrix}) \\ & + tr(B(B^TB)^{-1}B^TNB(B^TB)^{-1}B^T)) \\ & \equiv \min_{\substack{\tilde{A}=\mathrm{col}(\vec{\alpha}_i)\,|\,\mathrm{span}(\vec{\alpha}_i)\perp U \\ B=\mathrm{col}(\vec{\beta}_i)\,|\,U=\mathrm{span}(\vec{\beta}_i)\subseteq V}} -(f(B,\tilde{A},M)+g(B,N))\,, \end{aligned}$$

for functions f and g defined as the respective portions of the cost function.

It is at this step that we notice that if one were to drop the orthogonality constraint, the optimization over $\tilde{A}$ and B would live on a product space of Grassmannians,

$$(\tilde{A},B)\in\mathfrak{Gr}_i^n\times\mathfrak{Gr}_k^n\,. \tag{6.23}$$

Formally, we can impose the orthogonality by introducing a cost penalty C of the following form:

$$C = \lim_{\xi \to \infty} e^{\xi((i+k)-\mathrm{rank}(A))} \,. \tag{6.24}$$

This gives an infinite penalty whenever A is not full rank, or in other terms, whenever $\tilde{A}$ has a span that becomes subspace degenerate with the column span of B. This cost is not possible to implement or account for numerically. However, if one were randomly sampling matrices from the product space with double precision numerics, this degeneracy would occur with vanishing probability and $(A^T A)^{-1}$ will never be singular. Yet, in an optimization scheme, one has to worry about whether the optimal flow will drive toward such a degeneracy. A simple heuristic argument can convince the reader that this should not happen for symmetric positive-definite matrices, however. The projection will yield a positive semi-definite matrix with null columns on orthogonal projected subspaces. Larger rank subspaces (i.e., whenever $\tilde{A}$ is full) contribute more to the maximizing trace we are optimizing. Therefore, the minimum (negative trace) should be driven *away* from these degenerate configurations and we should not expect numerical instability arising from nearly singular matrices. In practice, this is confirmed.

In this way, we have transformed the problem from constrained optimization on a flag manifold into an unconstrained optimization over a product of Grassmannians.

6.6 Euclidean Computations for the Grassmannian Map

To proceed with a trust-region or gradient descent method, we need to compute the Euclidean gradients and Hessians of our cost function:

$$
\begin{aligned}
H_{ijk} &= \min_{\substack{\tilde{A}=\mathrm{col}(\vec{\alpha}_i)\,|\,\mathrm{span}(\vec{\alpha}_i)\perp U \\ B=\mathrm{col}(\vec{\beta}_i)\,|\,U=\mathrm{span}(\vec{\beta}_i)\subseteq V}} -(f(B,\tilde{A},M)+g(B,N)) \qquad (6.25)\\
f(B,\tilde{A},M) &\equiv (tr(\begin{bmatrix}B & \tilde{A}\end{bmatrix}(\begin{bmatrix}B & \tilde{A}\end{bmatrix}^T\begin{bmatrix}B & \tilde{A}\end{bmatrix})^{-1}\begin{bmatrix}B & \tilde{A}\end{bmatrix}^T M\begin{bmatrix}B & \tilde{A}\end{bmatrix}(\begin{bmatrix}B & \tilde{A}\end{bmatrix}^T\begin{bmatrix}B & \tilde{A}\end{bmatrix})^{-1}\begin{bmatrix}B & \tilde{A}\end{bmatrix}^T)\\
g(B,N) &\equiv tr(B(B^TB)^{-1}B^TNB(B^TB)^{-1}B^T))
\end{aligned}
$$

for functions f and g defined as the respective portions of the cost function.

6.6.1 Gradients

$\nabla_{\cdot} f$

We compute the first order Frechet derivative of f with respect to B to begin, using a small perturbation d. Recall that the Frechet derivative of a function $f : S \to \mathbb{R}$ at a point s in a normed linear space S is defined as the unique linear operator $\mathscr{D}$ tangent to f at s that satisfies

$$f(s+d) = f(s) + \mathscr{D}(d) + \mathcal{O}^+ . \qquad (6.26)$$

On the space of real matrices equipped with the Frobenius norm, the gradient should satisfy the relation

$$\mathscr{D}(d) = \langle \nabla_s f, d\rangle = tr((\nabla_s f)^T d) . \qquad (6.27)$$

We use the notation $[left]$ to denote duplication of 'the same block of terms as expanded on the left,' for conciseness.

$$
\begin{aligned}
f(B+d,\tilde{A},M) &= tr(\begin{bmatrix}B+d & \tilde{A}\end{bmatrix}(\begin{bmatrix}B^T+d^T\\ \tilde{A}^T\end{bmatrix}\begin{bmatrix}B+d & \tilde{A}\end{bmatrix})^{-1}\begin{bmatrix}B^T+d^T\\ \tilde{A}^T\end{bmatrix}M[left]) \qquad (6.28)\\
&= tr(\begin{bmatrix}B+d & \tilde{A}\end{bmatrix}(\begin{bmatrix}B^TB & B^T\tilde{A}\\ \tilde{A}^TB & \tilde{A}^T\tilde{A}\end{bmatrix}+\begin{bmatrix}B^Td+d^TB & d^T\tilde{A}\\ \tilde{A}^Td & 0\end{bmatrix})^{-1}\begin{bmatrix}B^T+d^T\\ \tilde{A}^T\end{bmatrix}M[left])\\
&+ \mathcal{O}^+ .
\end{aligned}
$$

Let

$$X \equiv \begin{bmatrix} (X_1)_{k\times k} & (X_2)_{k\times i} \\ (X_3)_{i\times k} & (X_4)_{i\times i} \end{bmatrix} \equiv (\begin{bmatrix} B & \tilde{A} \end{bmatrix}^T \begin{bmatrix} B & \tilde{A} \end{bmatrix})^{-1} . \tag{6.29}$$

be the block matrix representing the inverse of the symmetric matrix $\begin{bmatrix} B & \tilde{A} \end{bmatrix}^T \begin{bmatrix} B & \tilde{A} \end{bmatrix}$. Given that inverses preserve symmetry, we note the following properties:

$$\begin{aligned} X^T &= X \\ X_1^T &= X_1 \\ X_4^T &= X_4 \\ X_2^T &= X_3 . \end{aligned} \tag{6.30}$$

Using this notation, we can expand the inverse assuming our perturbation d is infinitesimal:

$$f(B+d,\tilde{A},M) = tr(\begin{bmatrix} B+d & \tilde{A} \end{bmatrix} (X - X \begin{bmatrix} B^T d + d^T B & d^T \tilde{A} \\ \tilde{A}^T d & 0 \end{bmatrix} X) \begin{bmatrix} B^T + d^T \\ \tilde{A}^T \end{bmatrix} M[left]) + \mathcal{O}^+ . \tag{6.31}$$

Expanding all terms left of M up to first order in d, we result in two terms built out of sums of $n \times n$ matrices that we have grouped according to their sign:

$$\begin{aligned} f(B+d,\tilde{A},M) &= tr([\{BX_1B^T + dX_1B^T + \tilde{A}X_3B^T + BX_1d^T + \tilde{A}X_3d^T + BX_2\tilde{A}^T + \tilde{A}X_4\tilde{A}^T\} \\ &- \{BX_1B^TdX_1B^T + BX_1d^TBX_1B^T + BX_1d^T\tilde{A}X_3B^T + \tilde{A}X_3B^TdX_1B^T \\ &+ \tilde{A}X_3d^TBX_1B^T + \tilde{A}X_3d^T\tilde{A}X_3B^T + BX_2\tilde{A}^TdX_1B^T + \tilde{A}X_4\tilde{A}^TdX_1B^T \\ &+ BX_1B^TdX_2\tilde{A}^T + BX_1d^TBX_2\tilde{A}^T + BX_1d^T\tilde{A}X_4\tilde{A}^T + \tilde{A}X_3B^TdX_2\tilde{A}^T \\ &+ \tilde{A}X_3d^TBX_2\tilde{A}^T + \tilde{A}X_3d^T\tilde{A}X_4\tilde{A}^T + BX_2\tilde{A}^TdX_2\tilde{A}^T + \tilde{A}X_4\tilde{A}^TdX_2\tilde{A}^T\}]M[left]) \\ &+ \mathcal{O}^+ . \end{aligned} \tag{6.32}$$

We now introduce useful shorthands to illustrate some of the symmetry in this equation. Let the second term in curly brackets be denoted $\{*\}$. Similarly, let

$$\{**\} \equiv \{dX_1B^T + BX_1d^T + \tilde{A}X_3d^T = dX_2\tilde{A}^T - \{*\}\}, \tag{6.33}$$

and

$$\{***\} \equiv \{BX_1B^T + \tilde{A}X_3B^T + BX_2\tilde{A}^T + \tilde{A}X_4\tilde{A}^T\}. \tag{6.34}$$

Expanding further considering the orders of d contained in $[left]$, we can pull off the gradient contribution by looking at the first order terms in d:

$$\mathscr{D}f = tr(\{***\}M\{**\} + \{**\}M\{***\}). \tag{6.35}$$

Now note that by making liberal use of the symmetry properties of the blocks of X, $\{***\}^T = \{***\}$. Similarly, $\{*\}^T = \{*\}$ therefore $\{**\}^T = \{**\}$. Recalling that traces are invariant under transpose, and that the trace of a sum is the sum of the traces, along with the fact that M is symmetric, we can reduce this to the following compact form:

$$\mathscr{D}f = 2tr(\{***\}M\{**\}). \tag{6.36}$$

A remarkable simplification is that $\{***\} = \begin{bmatrix} B & \tilde{A} \end{bmatrix} X \begin{bmatrix} B & \tilde{A} \end{bmatrix}^T = \pi_V$. Expanding out the full expression and utilizing the cyclic property of the trace to push all of the d and d^T terms to the right, we find the following expression:

$$\begin{aligned}
\mathscr{D}f &= 2tr(X_1B^T\pi_V Md + \pi_V MBX_1d^T + \pi_V M\tilde{A}X_3d^T + X_2\tilde{A}^T\pi_v Md - X_1B^T\pi_V MBX_1B^Td \\
&- BX_1B^T\pi_V MBX_1d^T - \tilde{A}X_3B^T\pi_V MBX_1d^T - X_1B^T\pi_V M\tilde{A}X_3B^Td - BX_1B^T\pi_V M\tilde{A}X_3d^T \\
&- \tilde{A}X_3B^T\pi_V M\tilde{A}X_3d^T - X_1B^T\pi_V MBX_2\tilde{A}^Td - X_1B^T\pi_V M\tilde{A}X_4\tilde{A}^Td - X_2\tilde{A}^T\pi_V MBX_1B^Td \\
&- BX_2\tilde{A}^T\pi_V MBX_1d^T - \tilde{A}X_4\tilde{A}^T\pi_V MBX_1d^T - X_2\tilde{A}^T\pi_V M\tilde{A}X_3B^Td - BX_2\tilde{A}^T\pi_V M\tilde{A}X_3d^T \\
&- \tilde{A}X_4\tilde{A}^T\pi_V M\tilde{A}X_3d^T - X_2\tilde{A}^T\pi_V MBX_2\tilde{A}^Td - X_2\tilde{A}^T\pi_V M\tilde{A}X_4\tilde{A}^Td).
\end{aligned} \tag{6.37}$$

Using the trace to relate to the norm on our space, we can rewrite these terms to remove all transposes on the perturbation d and read off the effect of the gradient:

$$
\begin{aligned}
\mathscr{D}f &= 2(\langle M\pi_V BX_1, d\rangle + \langle \pi_V MBX_1, d\rangle + \langle \pi_V M\tilde{A}X_3, d\rangle + \langle M\pi_V \tilde{A}X_3, d\rangle \\
&- \langle BX_1B^TM\pi_V BX_1, d\rangle - \langle BX_1B^T\pi_V MBX_1, d\rangle - \langle \tilde{A}X_3B^T\pi_V MBX_1, d\rangle - \langle BX_2\tilde{A}^TM\pi_V BX_1, d\rangle \\
&- \langle BX_1B^T\pi_V M\tilde{A}X_3, d\rangle - \langle \tilde{A}X_3B^T\pi_V M\tilde{A}X_3, d\rangle - \langle \tilde{A}X_3B^TM\pi_V BX_1, d\rangle - \langle \tilde{A}X_4\tilde{A}^TM\pi_V BX_1, d\rangle \\
&- \langle BX_1B^TM\pi_V \tilde{A}X_3, d\rangle - \langle BX_2\tilde{A}^T\pi_V MBX_1, d\rangle - \langle \tilde{A}X_4\tilde{A}^T\pi_V MBX_1, d\rangle - \langle BX_2\tilde{A}^TM\pi_V \tilde{A}X_3, d\rangle \\
&- \langle BX_2\tilde{A}^T\pi_V M\tilde{A}X_3, d\rangle - \langle \tilde{A}X_4\tilde{A}^T\pi_V M\tilde{A}X_3, d\rangle - \langle \tilde{A}X_3B^TM\pi_V \tilde{A}X_3, d\rangle - \langle \tilde{A}X_4\tilde{A}^TM\pi_V \tilde{A}X_3, d\rangle)\,.
\end{aligned} \tag{6.38}
$$

With a clever observation, one can rearrange these terms back into a matrix equation for the gradient itself. Using $\mathscr{S}(\cdot)$ to denote the symmetric part of a square matrix given by $\mathscr{S} : M \mapsto \frac{M+M^T}{2}$, we finally produce the following equation:

$$
\nabla_B f = (\mathbb{I}_{n\times n} - \pi_V)\mathscr{S}(M\pi_V)AX \begin{bmatrix} \mathbb{I}_{k\times k} \\ \mathbb{O}_{i\times k} \end{bmatrix}\,. \tag{6.39}
$$

A strong intuition might suggest that the gradient with respect to $\tilde{A}$ has a similar form with the other projected column of X. This can be checked to be the case:

$$
\nabla_{\tilde{A}} f = (\mathbb{I}_{n\times n} - \pi_V)\mathscr{S}(M\pi_V)AX \begin{bmatrix} \mathbb{O}_{k\times i} \\ \mathbb{I}_{i\times i} \end{bmatrix}\,. \tag{6.40}
$$

$\nabla . g$

Our computation for the second term $g(B, N)$ is much simpler.

We can immediately see that

$$
\nabla_{\tilde{A}} g = 0\,. \tag{6.41}
$$

For $\nabla_B g$, we take a similar approach to the above computation, beginning with our expansion in d up to linear order. For shorthand, we let $Y \equiv (B^TB)^{-1}$.

$$\begin{aligned} g(B+d,N) &= tr([(B+d)((B+d)^T(B+d))^{-1}(B+d)^T]N[left]) \\ &= tr([(B+d)(B^TB+B^Td+d^TB)^{-1}(B^T+d^T)]N[left])+\mathcal{O}^+ \\ &= tr([(B+d)(Y-Y(B^Td+d^TB)Y)(B^T+d^T)]N[left])+\mathcal{O}^+ \qquad (6.42) \\ &= tr([BYB^T+BYd^T-\pi_UdYB^T-BYd^T\pi_U+dYB^T]N[left])+\mathcal{O}^+ . \end{aligned}$$

Pulling off the first order term and exploiting trace and transpose symmetries as above, we find

$$\mathscr{D}g = 2tr(\{\diamond\}N\{\diamond\diamond\}) , \qquad (6.43)$$

where

$$\begin{aligned} \{\diamond\} &\equiv BYB^T \qquad (6.44) \\ \{\diamond\diamond\} &\equiv BYd^T-\pi_UdYB^T-BYd^T\pi_U+dYB^T . \qquad (6.45) \end{aligned}$$

Massaging this into the form for our inner product $\langle\cdot,d\rangle$, we simplify to this expression:

$$\mathscr{D}g = 2(\langle NBY,d\rangle - \langle\pi_UNBY,d\rangle) . \qquad (6.46)$$

We can finally read off our last gradient as follows:

$$\nabla_Bg = 2(\mathbb{I}_{n\times n}-\pi_U)NBY . \qquad (6.47)$$

6.6.2 Hessians

At this stage, let the perturbed coordinates in a secondary direction be distinguished by a dot notation, $\dot{X}$.

Handling g first this time, we note through the chain rule and derivatives of matrix inverses that

$$\begin{aligned} \dot{Y} &= Y(\dot{B}^T B + B^T \dot{B})Y \\ \dot{\pi}_U &= \dot{B}YB^T + B\dot{Y}B^T + BY\dot{B}^T \,. \end{aligned} \tag{6.48}$$

This results in a Hessian of the form:

$$H(g) = 2[(\mathbb{I}_{n\times n} - \pi_U)N(\dot{B}Y + B\dot{Y}) - \dot{\pi}_U NBY] \,. \tag{6.49}$$

Similarly, using

$$\begin{aligned} \dot{A} &= \begin{bmatrix} \dot{B} & \dot{\tilde{A}} \end{bmatrix} \\ \dot{X} &= X(\dot{A}^T A + A^T \dot{A})X \\ \dot{\pi}_V &= \dot{A}XA^T + A\dot{X}A^T + AX\dot{A}^T \,, \end{aligned} \tag{6.50}$$

we find that our two components of the Hessian have the following form:

$$H(f) = [(\mathbb{I}_{n\times n} - \pi_V)(\mathscr{S}(M\dot{\pi}_V)AX + \mathscr{S}(M\pi_V)(\dot{A}X + A\dot{X})) - \dot{\pi}_V \mathscr{S}(M\pi_V)AX]\{ \begin{bmatrix} \mathbb{O}_{k\times k} \\ \mathbb{I}_{i\times k} \end{bmatrix}, \begin{bmatrix} \mathbb{I}_{k\times i} \\ \mathbb{O}_{i\times i} \end{bmatrix} \} \,, \tag{6.51}$$

where the projection vector in curly braces is chosen according to which component of the gradient is being used.

6.6.3 Testing the Grassmannian Map

Once we have computed the Euclidean gradients and Hessians, the `MANOPT` MATLAB package can internally perform the required transformation to relate our operators with the operators on the product manifold of Grassmanians [12].

We have checked the accuracy of our expressions against numerically calculated gradients and Hessians. Our expression is confirmed to stay within the correct tangent space and have the proper magnitude.

The graphical and numerical output from `MANOPT` for a sample optimization is reproduced below and illustrated in Fig. 6.2.

> [Gradient] The slope should be 2. It appears to be: 1.99989. If it is far from 2, then directional derivatives might be erroneous. The residual should be 0, or very close. Residual: 4.51188e-16. If it is far from 0, then the gradient is not in the tangent space.
>
> [Hessian] The slope should be 3. It appears to be: 2.99794. If it is far from 3, then directional derivatives or the Hessian might be erroneous. The residual should be zero, or very close. Residual: 9.48494e-16. If it is far from 0, then the Hessian is not in the tangent plane. $< d1, H[d2] > - < H[d1], d2 >$ should be zero, or very close. Value: 0.541143 - 0.541143 = -9.76996e-15. If it is far from 0, then the Hessian is not symmetric.

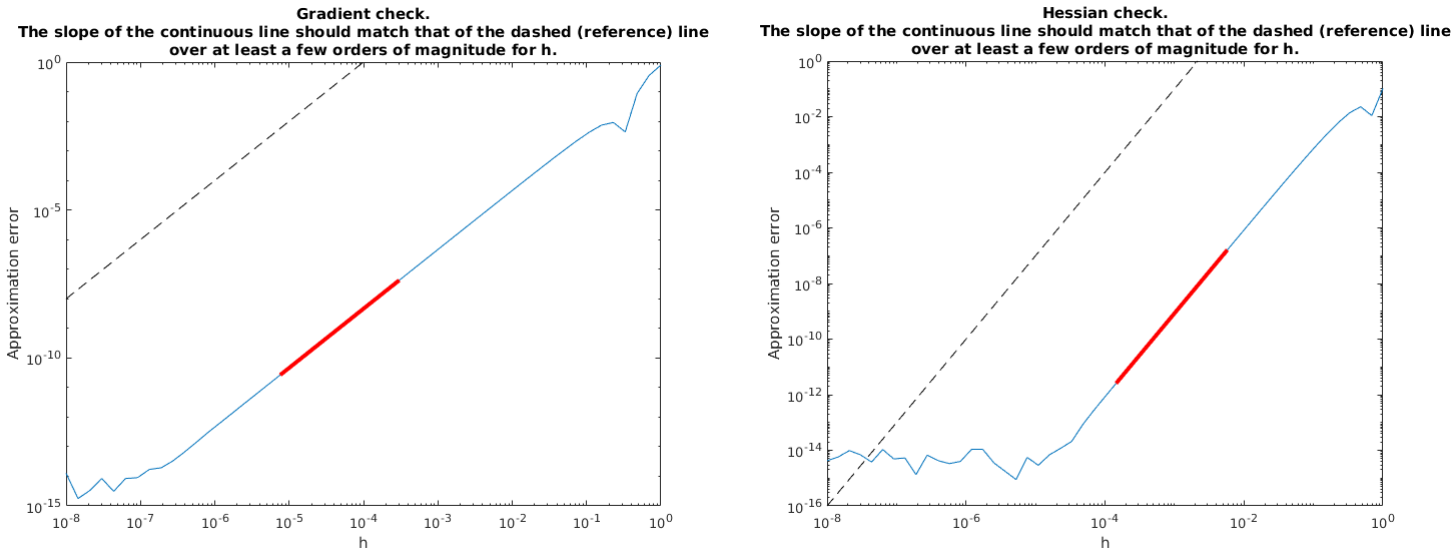

Figure 6.2: Gradient and Hessian accuracy test, indicating strong agreement between slow and potentially unstable numerical approximations and our derived results.

A further check that our analytical work is producing the correct hive coefficients can be performed by looking at the boundary elements of the hive. These elements are known by construction using simple algebra after the spectrum of the matrices are determined; however, we can ask our algorithm to compute these elements by way of the optimization scheme instead. Finding the boundary elements of the hive involves looking at the special cases when the contained subspace U is empty, when it is the same as V, and when there is no dimensional reduction projection for the larger of the subspaces and V spans W. Agreement with our optimization algorithm and the boundary data would therefore imply that our prescription is not only valid on the special cases when the Grassmann manifold dimensions i and k are 0, but in a general case whenever the product manifold is full rank $i + k = n$ and is thus a very good indicator. We find excellent agreement between the two, as illustrated in Fig. 6.3.

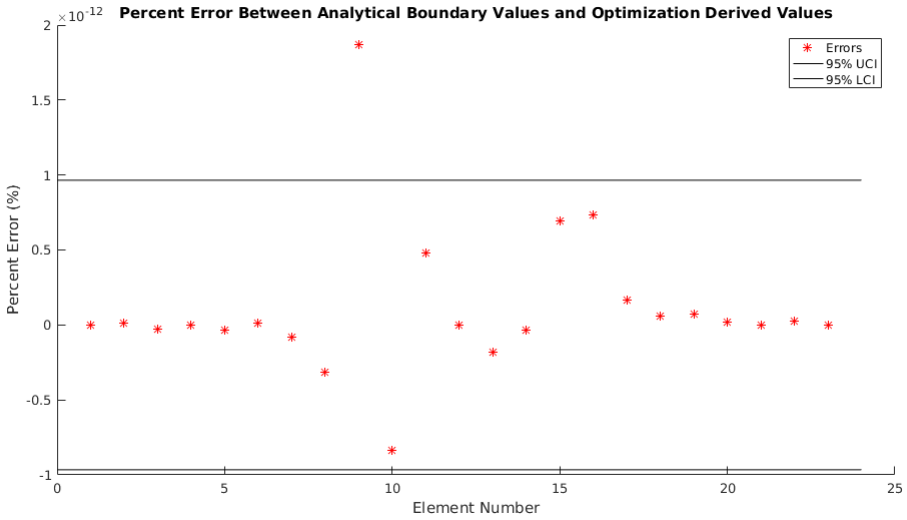

Figure 6.3: A hive boundary accuracy test for an 8-D vector space, illustrating that our optimization can achieve the correct hive boundary values on the order of machine precision percent error. Upper and lower 95% confidence intervals are illustrated.

6.7 Statistics on Generating Hives

We can use our analysis to generate local numerical solutions to the optimization problem that may or may not be global solutions (as provably global numerical solutions can not be guaranteed from this paradigm). These solutions, given our analytical map and its success for generating correct boundary data, may provide strong numerical evidence for the veracity of the theorem. Our solutions illustrate that using random Hermitian matrices does not always guarantee a hive, contradicting the optimization theorem as written and potentially implying that in addition to the insufficiency of the AW proof that we have noted, the theorem itself may be suspect. Examples of a success and failure from the Gaussian Orthogonal Ensemble $GOE(6)$ are shown in Fig. 6.4.

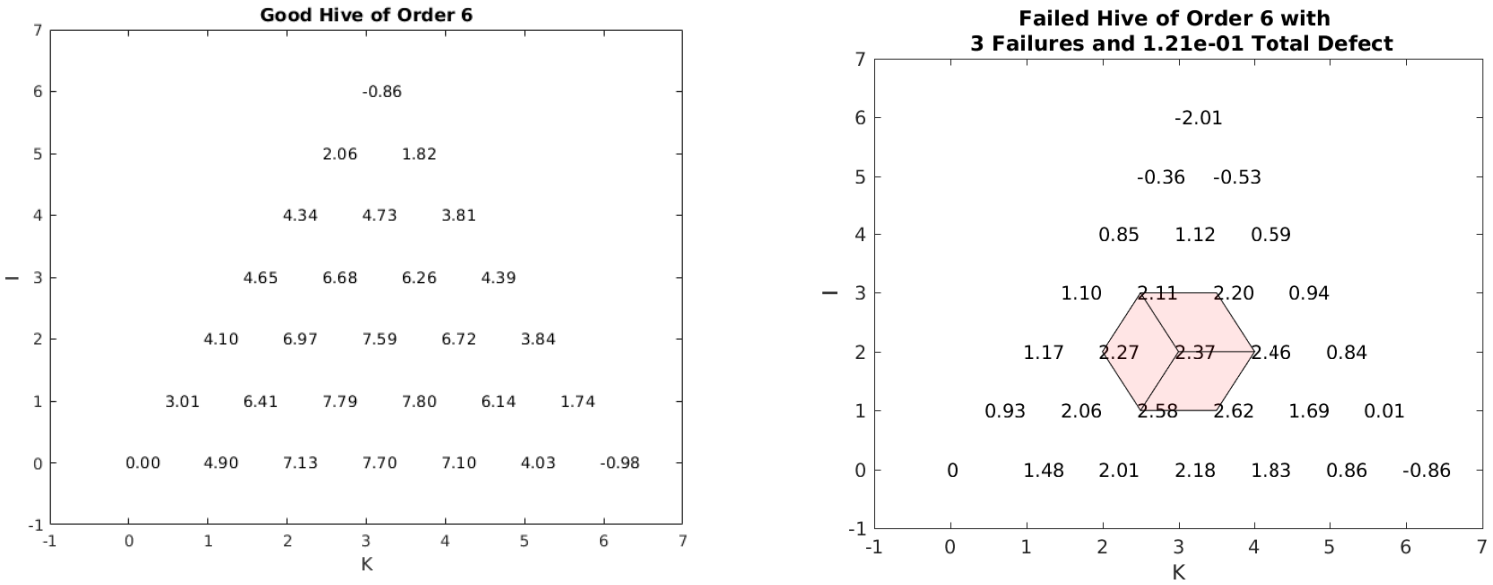

Figure 6.4: On the left we show a proper hive generated by our optimization map using matrices from $GOE(6)$; on the right is an improper hive from the same ensemble with the rhombus failures highlighted. This failure was unable to be rectified by over 1000 global re-optimizations, suggesting a possible genuine numerical counterexample to the AW proposal.

To get a sense for the scaling of the ability to find a hive as a function of matrix dimension in the case when the construction is not guaranteed, we sampled over such a set. We allowed for up to 5 re-optimizations per boundary in an attempt to eliminate accidental instabilities or local minima that were not hives. Additionally, each hive coefficient allowed for 5 re-optimizations in order to handle any individual numerical instabilities. If no hive could be found after such re-optimization attempts, the matrix pair was counted as not being able to produce a hive with respect to this optimization algorithm. The results are shown in Fig. 6.5, showing a stark decline in probability for GOE(n) with increasing matrix dimension. However, if we let $M = N$ or consider sorted diagonal matrices (also illustrated in Fig. 6.5) the algorithm appears to work with almost certain probability.

It should be noted that as a corollary to their Proposition 4, DK proved their conjecture for matrices of dimension 3 and mention that dimension 4 may be the first case where the conjecture is false [16]. Our numerical results appear to confirm that the AW construction also holds in general for 3×3 matrices where there is only a single interior hive point.

As mentioned in Sec. 6.4, one way to guarantee that the resulting traces are invariant after redistributing the subspace pair is to let $M = N$. The equality of the matrices is a structure that prevents such a failure as the traces are now maximized over the same subspaces, just with a dimensional restriction. We will always be able to trade dimensions to construct the new subspaces while maintaining the traces as the spaces overlap.

If we use this setup numerically, for convergent optimizations, we yield hives with extremely strong probability. Numerical instabilities in the high dimensional optimizations may induce hive failures, but this is due to nonconvergent optimizations discussed in Sec. 6.8 and not failures of the maximization condition. Of course, the optimization is in theory far easier now and the form *could* be reduced significantly when we exploit $M = N$. However, in our implementation, the optimization has not been adjusted to exploit the symmetry and it is still optimizing over the full space assuming M and $N(= M)$ are independent. This is further strong evidence for the obstruction illuminated in Sec. 6.4 and that the equality of the traces in the new subspaces is necessary for a hive to form.

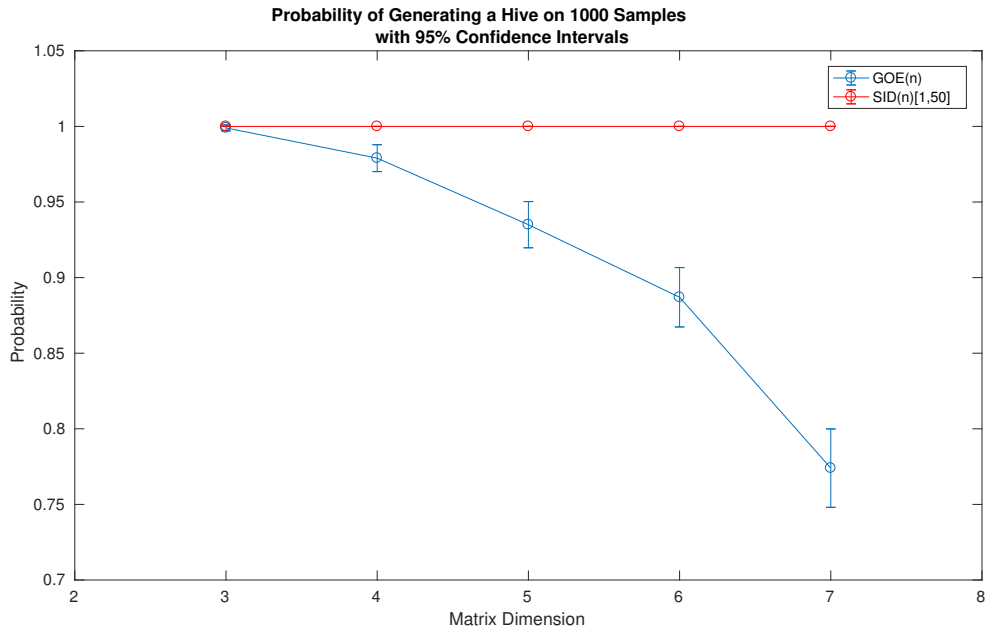

Figure 6.5: Probability and 95% confidence intervals for finding a hive on independent GOE(n) matrices, and on sorted integer diagonal matrices with entries within $[1, 50]$ (SID(n)$[1, 50]$)

This setup is restrictive, however, as it forces the main boundaries to have identical eigenvectors. One way to satisfy the new trace requirements while allowing for additional freedom is to simply use sorted diagonal matrices. Let the desired eigenvalue distributions be specified in a weakly ordered form, and let the matrices M and N be the diagonal matrices built from the eigenvalue distributions.

$$\begin{aligned} M &= diag([\mu_1 \cdots \mu_n]) \\ N &= diag([\nu_1 \cdots \nu_n])\,. \end{aligned} \tag{6.52}$$

We note that for the integer valued case, the third boundary will also naturally have integer values due to this structure. It is otherwise not generically true that the sum of two symmetric matrices with integer spectra yields a third matrix with integer spectra.

The ordering does not have to be descending—it is only important that the matrices have coherent ordering. This is enough structure to ensure that the trace equality will be met, as subspace containment during the first optimization (similar to the identical matrix case) will be guaranteed due to the ordering. This setup was again confirmed numerically as shown in Fig. 6.5.

As an additional test, if we reorder the highest and lowest eigenvalues in just one of the matrices as follows:

$$M \to diag([\mu_n \ \mu_2 \cdots \mu_{n-1} \ \mu_1]),$$

the optimization appears to fail guaranteed production of hives with respect to our definition of a hive optimization failure. Fig. 6.6 illustrates the decline in probability.

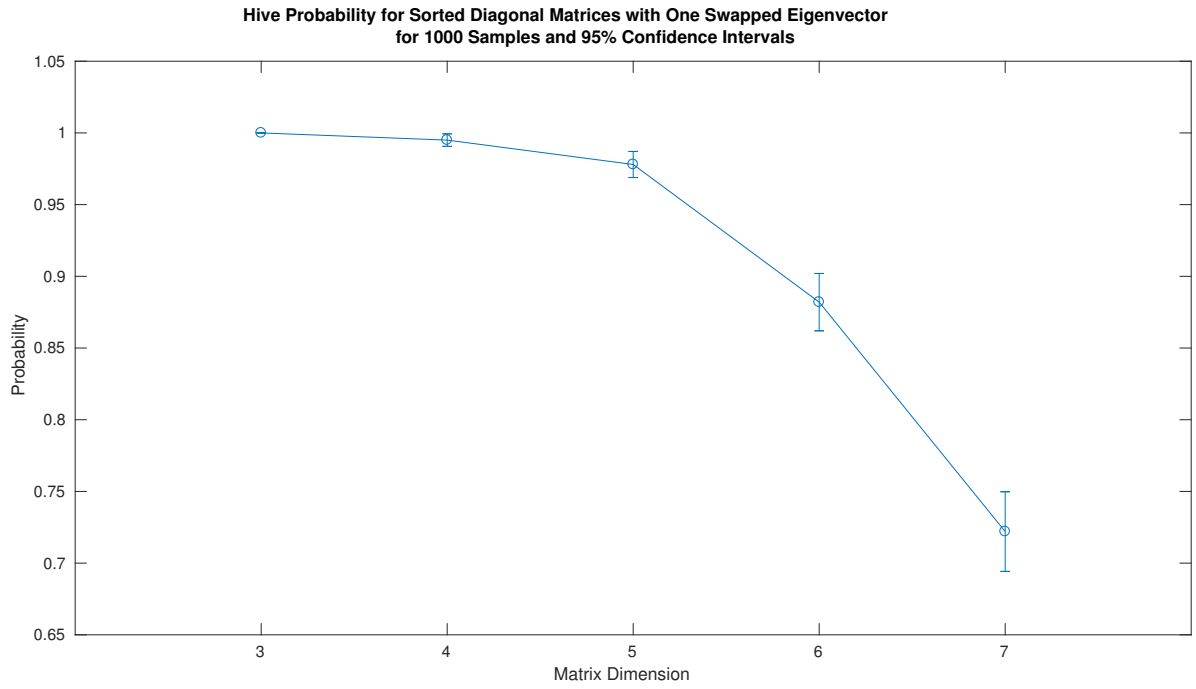

Figure 6.6: Probability and 95% confidence intervals for finding a hive on sorted integer diagonal matrices with entries within $[1, 50]$, where one of the matrices had its highest and lowest eigenvalues flipped.

In the original conjecture by DK, commuting matrices were proven to be a domain over which their proposal holds true [16]. If we investigate the optimization failures in Fig. 6.6 further, we find that there exists many nearby local optima that the algorithm may settle into which are not global solutions. The structure of such instabilities and modes of failure are discussed in Sec. 6.8. We can clean our statistics and filter out more of such failures by simply allowing for additional reoptimizations before considering a candidate hive to be a failure, reducing our false-positive counterexamples at the cost of computation time. Fig. 6.7 illustrates that on the same sample space of reordered integer diagonal matrices, or even a more general case of commuting symmetric real matrices, if we allow for the samples to be indefinitely reoptimized, the algorithm will ultimately produce a proper hive from each of the randomly generated boundaries from the respective classes.

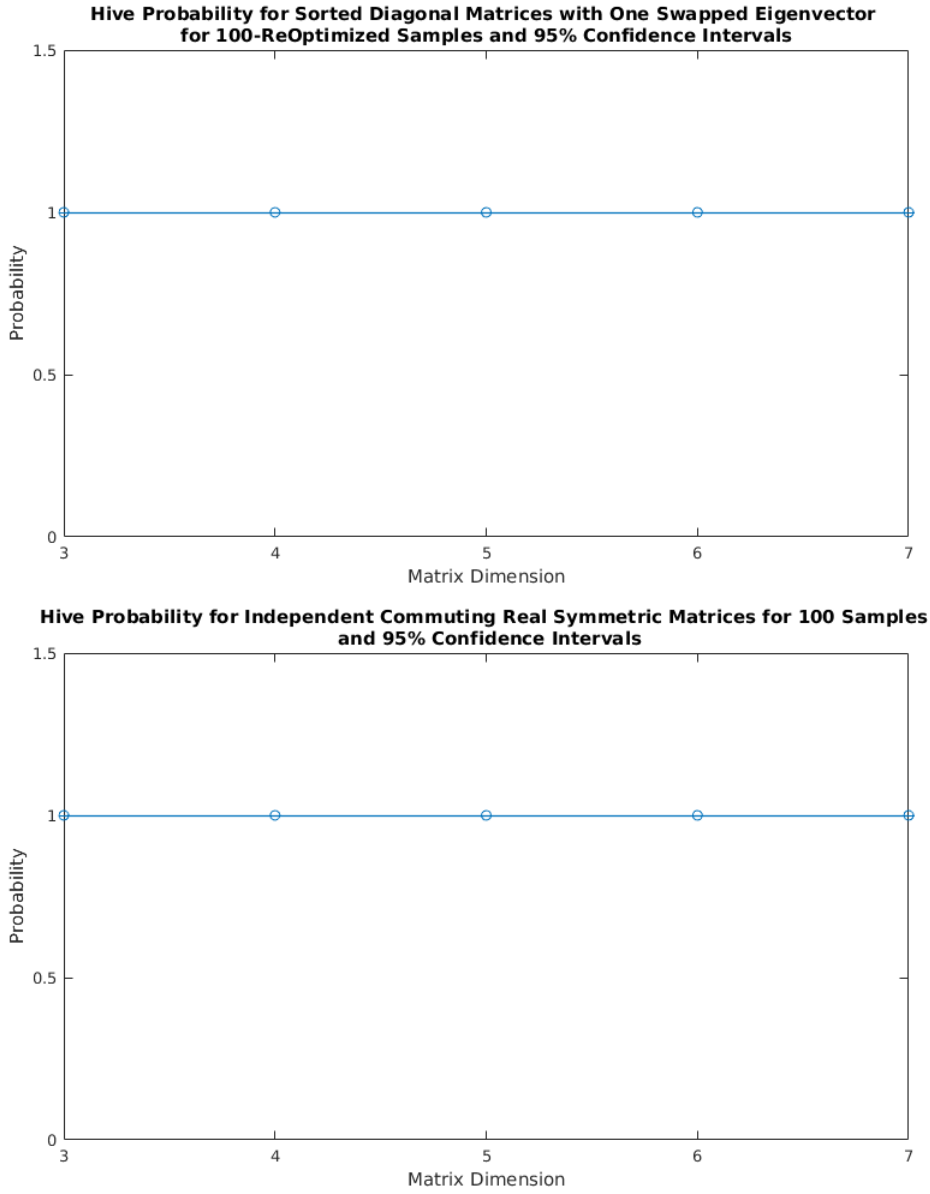

Figure 6.7: Probability and 95% confidence intervals for finding a hive on sorted integer diagonal matrices with entries within $[1, 50]$, where one of the matrices had its highest and lowest eigenvalues flipped, and for independent symmetric real commuting matrices. Here, we allow for an arbitrary number of reoptimizations, and the uniform probability at 1 indicates that the algorithm supports the theoretical results of DK as well.

In this way, we can confirm that the AW prescription, like the DK conjecture, produces valid hives over a domain of commuting symmetric matrices. We also gain an understanding about the required increase in reoptimizations as a function of matrix dimension, providing a useful tool for characterizing the efficacy of our algorithm. These results now strengthen our evidence that our mapping and algorithm are performing as expected, therefore increasing the probability that the noncommuting matrix counterexample in Fig. 6.4, which could not be resolved through reoptimization, is a genuine high dimensional counterexample to the AW theorem.

We further examine the nature of one of these candidate failures in Fig. 6.8. In addition to our trust-region methods, we also allowed for a particle swarm optimization method to attempt to find the optimum of each hive coefficient. We selected the deepest solution to the cost function from the union of these two optimizers, and yet, the hive failure remained even after over 1000 reoptimization attempts. We notice in this example, however, that it appears that the coefficient $(i, k) = (2, 1)$ is tight at roughly 121.99. If we simply adjust this to 122 by hand, a good hive is produced. We can now ask whether our previous solution was still a local optimum and if numerical difficulties prevented us from reaching such a global solution, or whether there was a larger obstruction to finding the rectified hive.

This example was constructed from non-commuting matrices with positive integer spectra for (M, N) (but not integer for $L = M + N$). The approximate spectra (in their natural subspace ranking) are as follows:

$$\begin{aligned} \mu &= (35, 28, 18, 12) \\ \nu &= (34, 35, 40, 41) \\ \lambda &= (46.48, 58.80, 70.88, 66.84) \end{aligned} \tag{6.53}$$

The coefficient we modified would have been computed from an optimization of the following form:

$$\max_{(U,V)\in\mathbb{F}_{1,3}} \left(tr(M|_V) + tr(N|_U)\right). \tag{6.54}$$

We note that the only way to achieve a maximization that would yield 122 would be to take the partial sum of the three largest eigenvalues for μ and add that to the largest eigenvalue of ν. This would mean that we are requiring the optimization to utilize the subspaces which maximize each partial trace individually. However, this is not possible, as the eigenvector for the eigenvalue of 41 for N does not live in the eigenspace spanned by the largest three eigenvalues of M, and we require subspace containment in the theorem. Therefore, achieving 122 for this coefficient with the theorem is simply impossible and not a failing of our algorithm or optimization. This is precisely the situation we describe in Sec. 6.4, where the spaces which allow for the trace conditions to be met that satisfy the rhombus inequalities are not subspaces which are permitted—the eigenstructures of the matrices are not coherent, and the subspaces are not properly contained. Although we have yet to produce a proof or a numerical counterexample that can be explicitly checked in its entirely by hand, this analysis provides further evidence for the failure of the theorem.

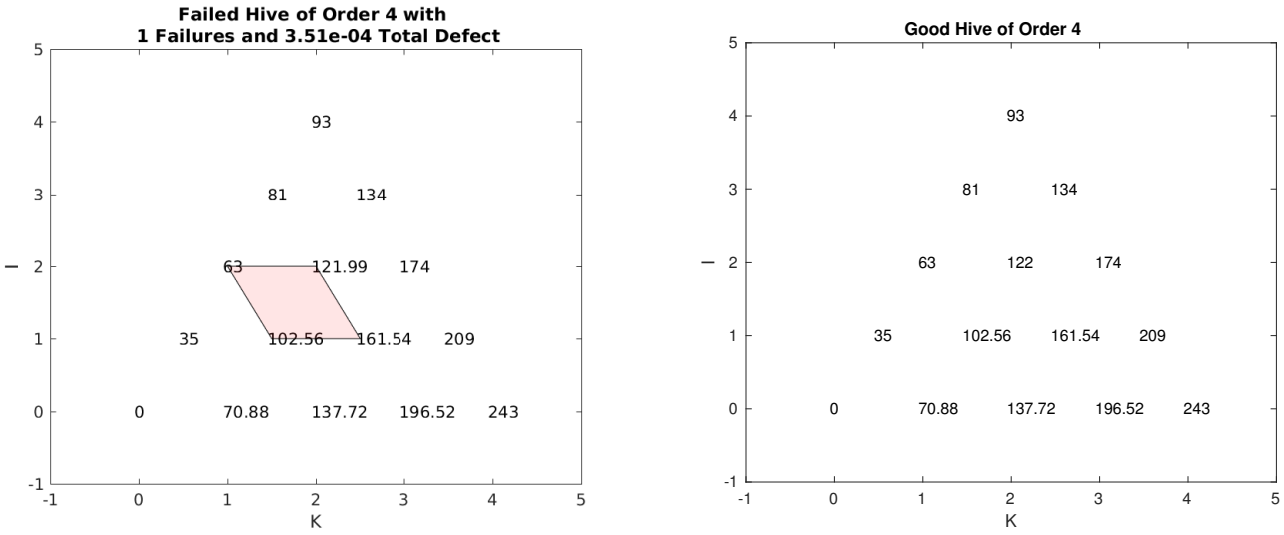

Figure 6.8: Another candidate for a genuine failure to the AW theorem as produced by our algorithm, and a resolved hive from manual adjustment of a single coefficient

6.8 Optimization Instabilities

We note that in terms of numerical instabilities, we occasionally see an oscillation in the gradient norm followed by a fixed-point that is accompanied by a divergence of the joint-matrix inverse. This is illustrated in Fig. 6.9. This would be indicative of the type of divergence described above when considering the missing orthogonality constraint on the product manifolds, but given the same matrix data for positive-definite matrices, re-optimizations can resolve this divergence and produce a valid hive. This indicates that the divergence is, if fact, not located at the optimum, but is instead due to unstable attractors or simply overshoot in the algorithm. As can be seen in Fig. 6.10, the symmetries of the Grassmannians as well as the properties of the traces in the cost function induce symmetries in the cost function space with a variety of nearby minima. Oscillations between such minima are possible, as well as issues handling the multi-dimensional saddles that clearly arise. We claim that these are the driving factors behind any instabilities in the optimization, and not any null-space issues arising from the formulation map itself (at least for the matrix ensembles with positive spectra). Finding a description of the optimization problem that does not contain redundant degrees of freedom may ameliorate some of these issues.

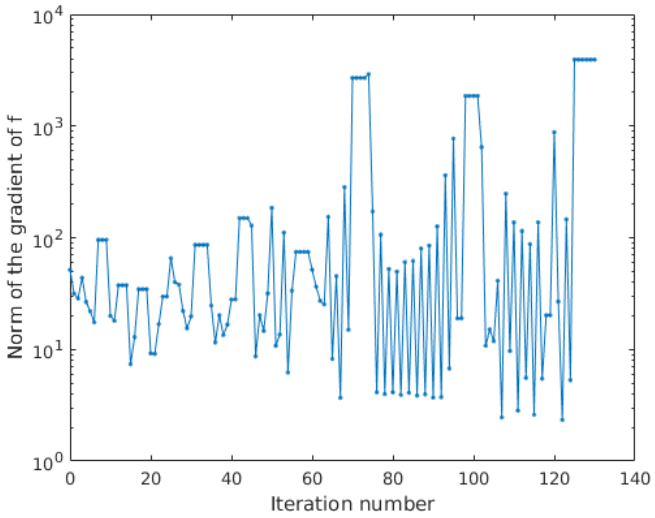

Figure 6.9: A failure of convergence in the gradient norm from the trust-region algorithm iteration steps

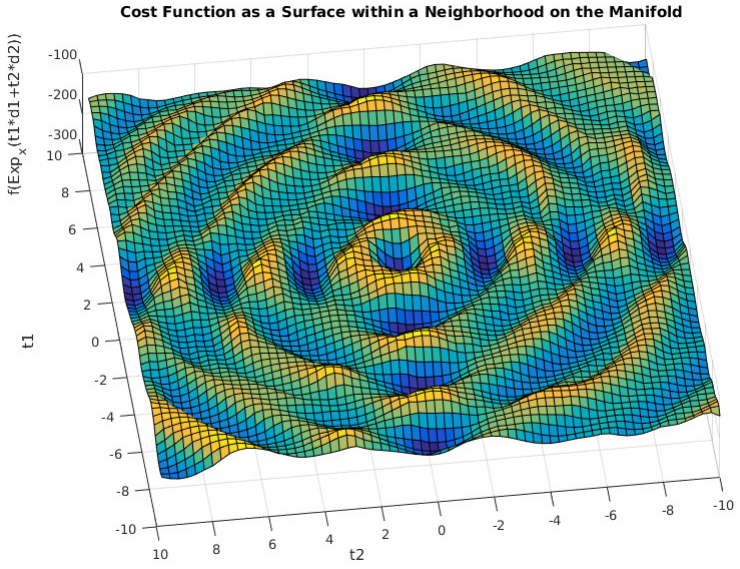

Figure 6.10: An example cost function 2-D subspace in a local neighborhood about the optimum

6.9 An Open Study of Hive Properties on Accessible Matrix Ensembles

Lastly, we examine a few matrix ensembles that give hives with extremely high probability for their average hive surface, average Gaussian curvature, and average mean curvatures. These are a few natural observables to compute when studying the random surfaces generated by the hive ensembles. We set a standardized placement of the hive points on a flat plane, and triangulate the interiors of the numerical hives using a Delaunay triangulation with the hive values as heights in an orthogonal direction. We then randomly sample from the matrix ensembles until we gather a fixed number of good hive samples. We render the algebraic average of the hive surfaces, as well as the mean curvatures. The curvatures on the edges are set to 0 by default, creating edge effects that should be noted.

6.9.1 GOE(n)

Pairs of identical matrices from the GOE create a highly symmetric parabolic surface. As we expect the distribution of eigenvalues to follow the Wigner semicircle law in the large matrix dimension limit, the cumulative sums on the angled boundaries also exhibit this behavior. With the bottom left corner normalized to 0, and with an even average of signed eigenvalues from the Wigner law, the tip of the triangulation also averages to 0 and the projected boundary curves resemble that of a parabola provided the right triangulation spacing [66].

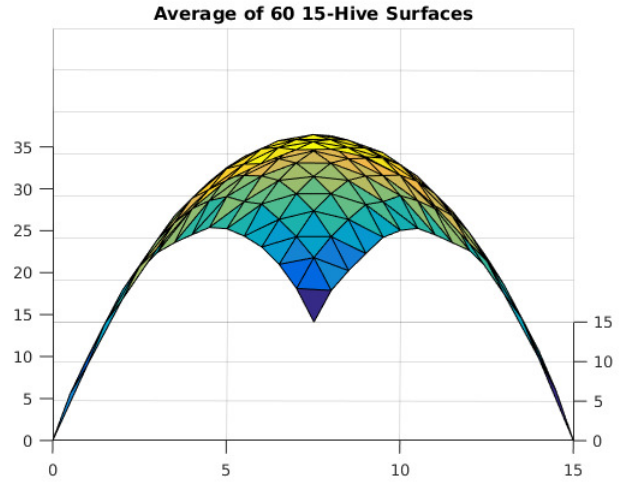

Figure 6.11: Average hive surface on 60 identical pairs of random GOE(15) matrices, illustrating the 'bowl-like' nature of the hives

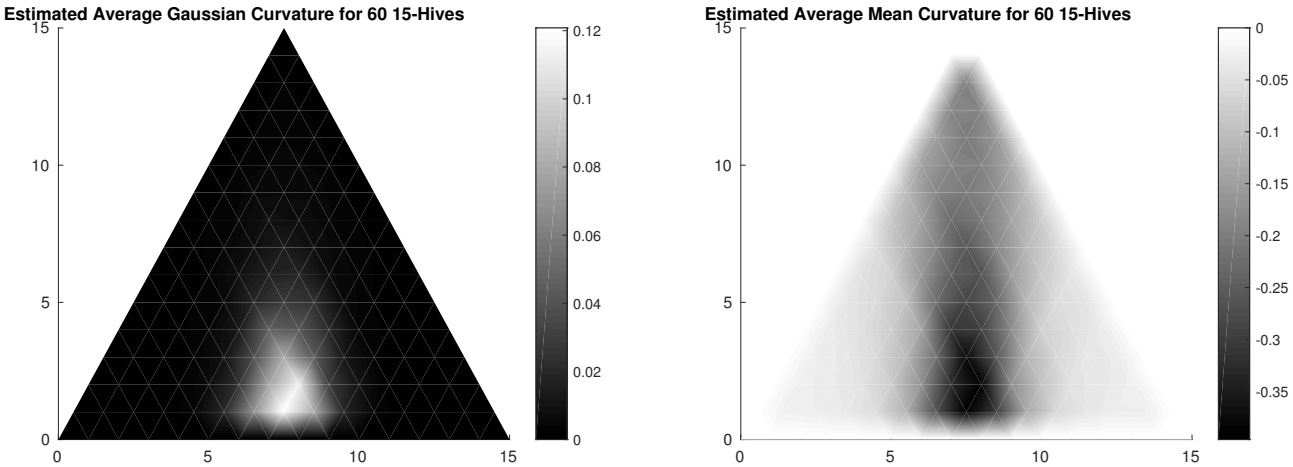

Figure 6.12: Average gaussian and mean curvatures on 60 identical pairs of random GOE(15) matrices

6.9.2 Integer Diagonal

Without the oppositely signed eigenvalues, the diagonal matrices produce a surface of nearly constant 0 Gaussian curvature and a tapering mean curvature that becomes nearly flat at

its highest point.

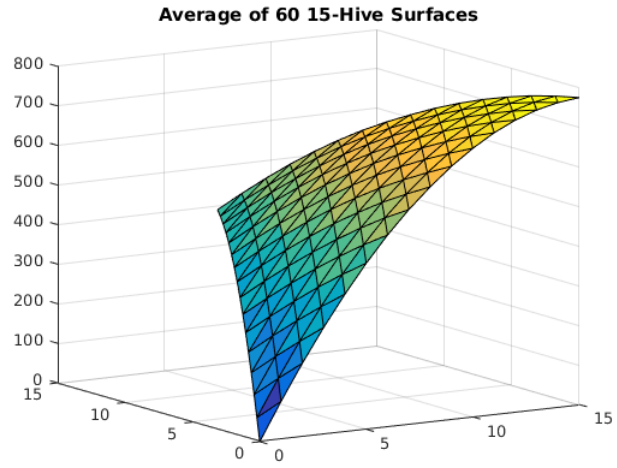

Figure 6.13: Average hive surface on 60 pairs of weakly decreasing positive integer 15×15 diagonal matrices, uniformly distributed on $[1, 50]$

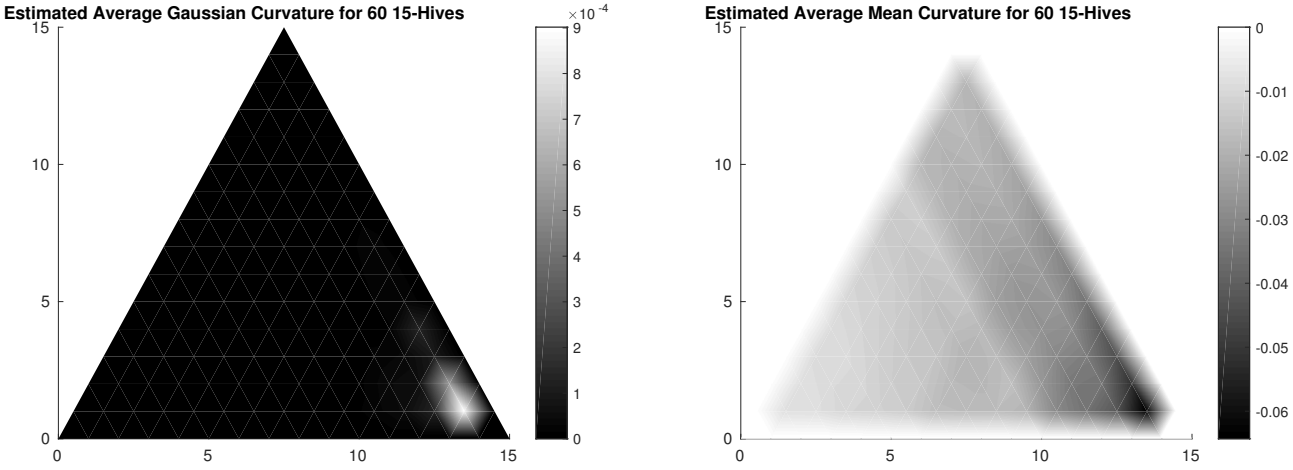

Figure 6.14: Average gaussian and mean curvatures on 60 pairs of weakly decreasing positive integer 15×15 diagonal matrices, uniformly distributed on $[1, 50]$

6.9.3 SPD(n)

The normally distributed symmetric positive definite (SPD) ensembles create a significantly more warped surface than the diagonal matrices, but in contrast, the diagonally dominant SPD matrices show a nearly flat surface over the whole triangulation.

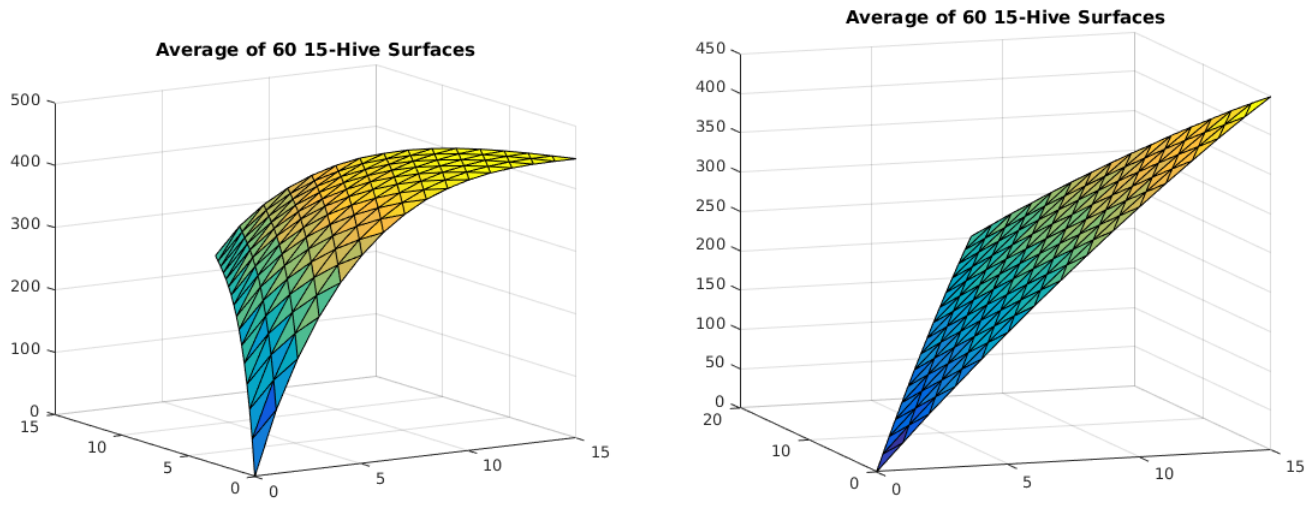

Figure 6.15: Average hive surface on 60 identical pairs of normally distributed SPD(15) matrices on the left, and diagonally dominant SPD(15) on the right

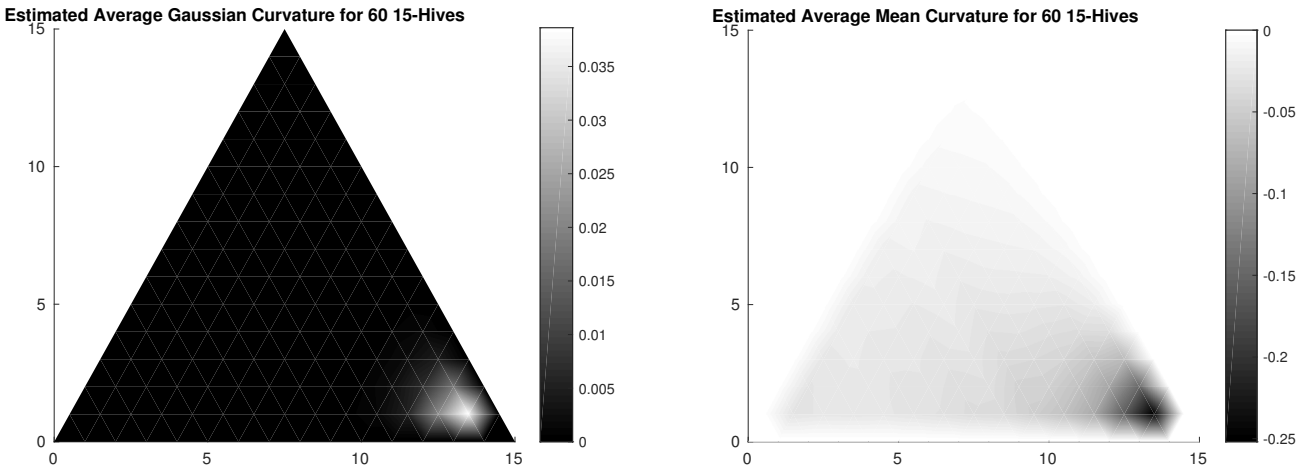

Figure 6.16: Average gaussian and mean curvatures on 60 identical pairs of normally distributed SPD(15) matrices

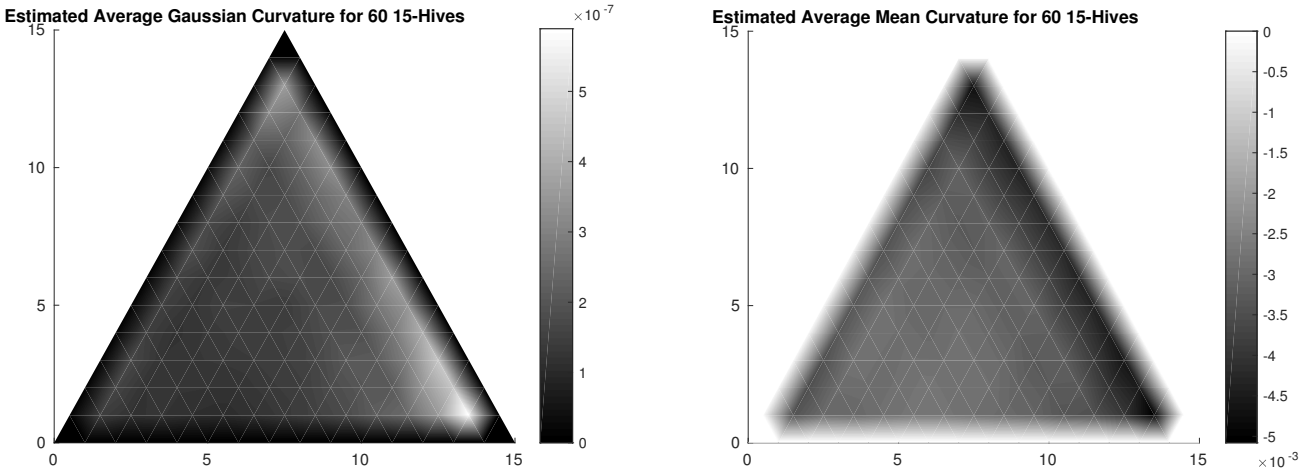

Figure 6.17: Average gaussian and mean curvatures on 60 identical pairs of diagonally dominant SPD(15) matrices

6.10 Summary of Hives from Hermitian Matrix Pairs

The conjecture provided by Danilov and Koshevoy was the first generative scheme for finding interior hive coefficients in the sense of Knutson and Tao for pairs of Hermitian matrices. With the modification by Appleby and Whitehead which was accompanied by a proposed sketch of a proof, this optimization theoretically opened the door to a wide area of study of random continuum hives from various matrix ensembles, if the construction could be implemented as a numerical algorithm. We have analytically shown that the supporting arguments by AW are not generically true, which prevents such a general study from being undertaken using that construction. However, we provided the first implementation of their proposal by way of an analytic map onto a product space of Grassmannians that allowed for the AW construction to be tested, and we characterized the probability to which the optimization fails to find proper hives. Furthermore, we note several cases where we can generate hives with remarkable probability, in agreement with the work from DK. In those ensembles, we have undertaken the first preliminary study of geometric observables of hive surfaces.

As noted, the usage of hives extends to the realm of computing Littlewood-Richardson coefficients for the integer valued cases. We now detail further results we have gained from studying combinatorial hives to that end.

6.11 Rounded Estimation of LRCs using Hit-and-Run on the Hives

It is possible to provide an estimate for the LRC associated with the 3-tuple of weight vectors (μ, ν, λ) given the hive construction. In this section, we discuss our implementation of the algorithm described by Narayanan in "Estimating Certain Non-Zero Littlewood-Richardson Coefficients" [50]. To our knowledge, this is the first implementation of a randomized approximation scheme for computing LRCs based on combinatorial hives. The algorithm relies on first forming the hive polytope $P^{\lambda}_{\mu\nu}$ constructed from the linear rhombus inequalities and the boundary equalities such that

$$Ax - b^{\lambda}_{\mu\nu} \preceq 0\,, \tag{6.55}$$

where A encodes the hyperplane structures and $b^{\lambda}_{\mu\nu}$ includes a vector of constants specifying the boundaries.

The polytope is then enlarged by a relaxation of the affine hyperplanes, providing a rescaling of the polytope $Q^{\lambda}_{\mu\nu}$ defined by some small fixed dilation as follows:

$$Ax - b^{\lambda}_{\mu\nu} \preceq 2\ . \tag{6.56}$$

An estimate for the continuum volume $\tilde{V}(Q^{\lambda}_{\mu\nu})$ of the enlarged polytope is then required. Once found, it is necessary to determine the number of integer lattice points of the interior original polytope that also fall inside the dilated polytope. Given this fractional estimate f, we can provide an approximation for the number of integer lattice points in the original hive as simply $V(HIVE(\mu,\nu,\lambda)) = f\tilde{V}(Q^{\lambda}_{\mu\nu})$.

In our implementation, the enlarged polytope volume is computed by using Cousins and Vempala's "A Practical Volume Algorithm," which includes empirical convergence tests, an adaptive annealing scheme, and a new rounding algorithm built upon the framework of Lovasz and Vempala's nested convex body approach for volume estimation [15] [45]. We take extra care in the preprocessing step of the polytope to avoid translations of the center of mass of the polytope to the origin, as this is not a lattice number preserving transform. However, we do perform the rounding preprocessing that violates the lattice volume. We discuss the implications of this in Section 6.12.1.

We then perform a sampling of rational points in the larger polytope using an adaptive centering hit-and-run method with an implementation provided by Benham [9]. We round the resulting points to the integer lattice, and test those points against the inequalities that define the original hive polytope, continuing to gather and test points until we achieve a convergence of the relative lattice volume estimate within some desired tolerance. Multiplying the outer continuum volume estimate by the fractional lattice volume estimate yields the desired integer lattice volume estimate for the original hive and thus the associated LRC.

6.11.1 Results of the Rounded Algorithm

We test the accuracy of this algorithm against known LRC values with respect to a user defined relative error parameter. The known LRC values were computed using Anders Buch's LRC C-based calculator that uses a computationally expensive exhaustive algorithm [13]. We pick a known 4-dimensional tuple, and look at scalar multiples of these weights that correspond to dilations of the hive polytope as a way of systematically testing the robustness of the algorithm for finding coefficients from progressively larger convex bodies. We see in Fig. 6.18 that the absolute accuracy of the algorithm decreases with hive volume, but the lower relative error parameter is able to compensate at the cost of computational time. Regardless of the error parameter, the algorithm has un-patterned fluctuations in its relative percent error with a wide deviation and no clear trend as a function of volume. However, we were able to achieve less than 5% absolute relative error out to LRC's with hive volumes on the order of 10^5 in under 5 seconds of computation time on a variety of modern architectures, where the exact Buch implementation would take on the order of minutes.

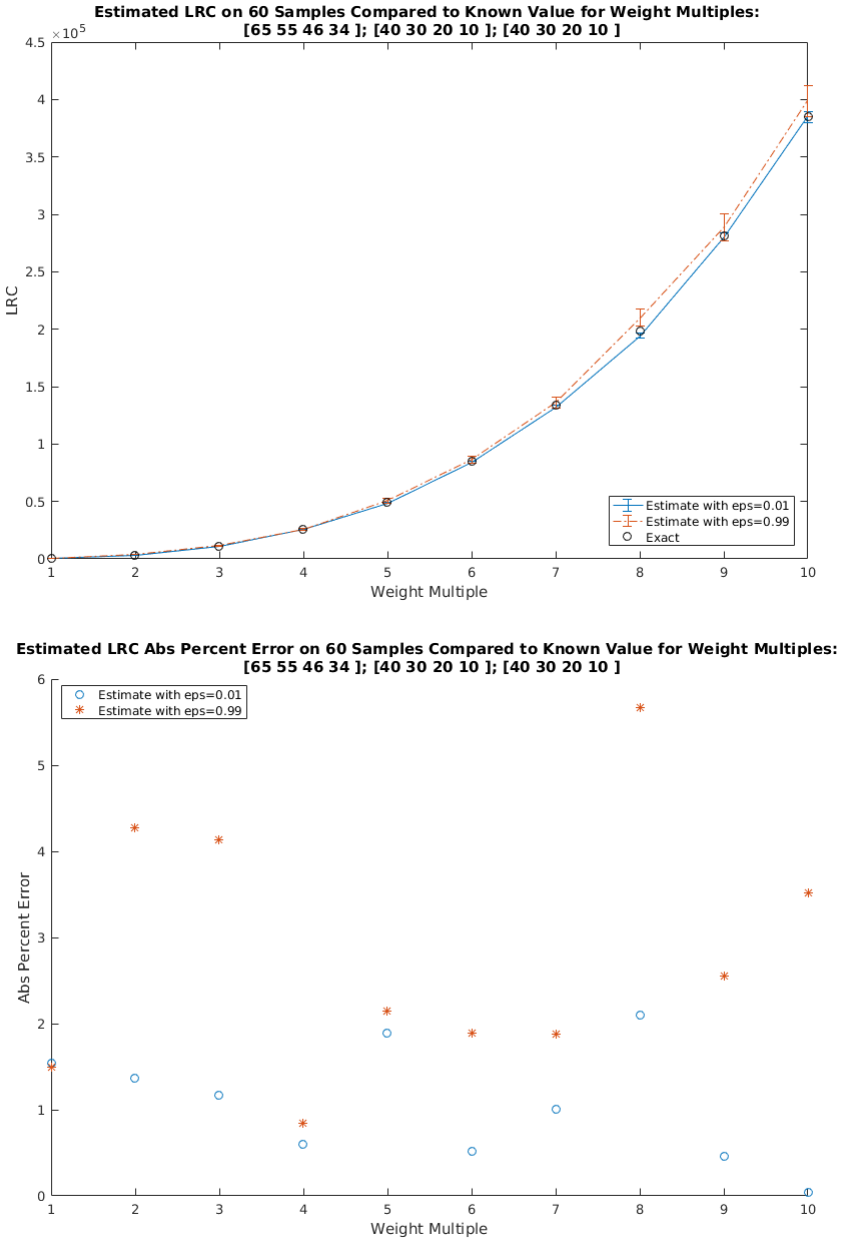

Figure 6.18: Accuracy of rounded LRC estimator for weight vector multiples, 95% confidence intervals and absolute percent error

6.12 Coordinate Hit-and-Run on the Hive Lattice Itself

We created a second estimation algorithm for the hive volumes, where instead of working in the continuum and rounding to the integer lattice, we attempt to estimate the lattice volumes directly using a lattice coordinate hit-and-run (CHAR). We use a similar volume ratio approach, but work directly on the lattice and utilize smart resampling in the style of Ge, Ma, and Zhang's "A Fast and Practical Method to Estimate Volumes of Convex Polytopes" [27]. Our algorithm takes the following form.

First, we formulate the maximum LP from the boundary data as it is guaranteed to give an integer point in the hive by Knutson and Tao. Assuming one can be found, this lattice point will be the start of a CHAR algorithm that is designed to approximate the full lattice volume of the hive. We avoid performing any rounding of the hive polytope, as this would not preserve lattice volume. Since the rhombus inequalities are constraints on 4 interior hive coordinates for each possible rhombus, the hyperplane matrix A has at most 4 nonzero entries per row with values ± 1. This indicates that the polytopes themselves are not markedly dissimilar to hypercubes in terms of their aspect ratios, and we do not expect extreme channels of small volume to appear that would cause conductance issues in our sampling algorithm. An illustration of this can be seen in Fig. 6.19, where we show the polytope corresponding to 4D weight vectors that yield the 3D interior hive volume from the 3 free bulk coordinates. The structure takes the form of a multi-faceted rounded rectangle that does not have an extreme aspect ratio or have narrow regions separating large volumes, etc.

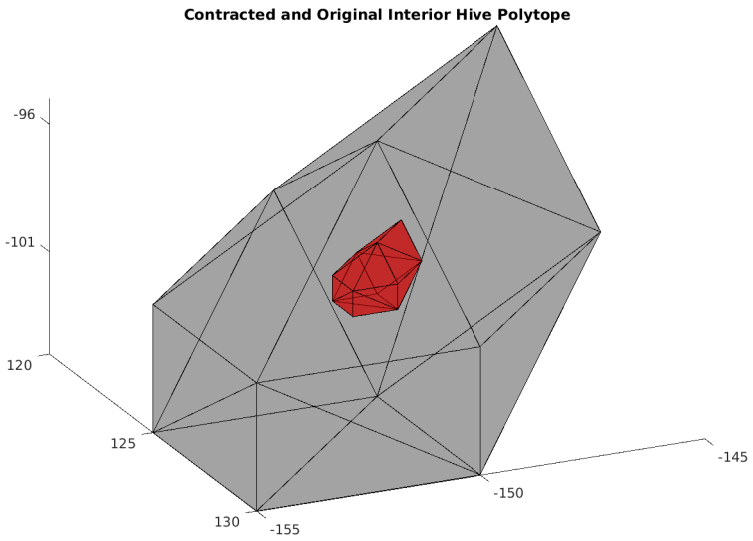

Figure 6.19: Original and Contracted Hive Polytope for a 4D Weight Vector Tuple

With our initial integer hive found, we then progressively constrain the hyperplanes uniformly in the LP by solving a series of LPs

$$Ax - b^{\lambda}_{\mu\nu} \preceq \xi \tag{6.57}$$

for $\xi \in [0, \ldots, \xi^*] \subset \mathbb{Z}^-$, shrinking the hive volume until no solution can be found at ξ^*, which indicates that there is no longer an integer point in the interior of the hive volume. We take as a shrunken polytope the hive defined by

$$Ax - b^{\lambda}_{\mu\nu} \preceq \min\left(0, \tilde{\xi} \equiv \xi^* + 2\right) \tag{6.58}$$

in order to avoid excessively small volumes that may induce lattice points that are not accessible by the coordinate alignment of our hit-and-run and give a false lattice volume. This contracted polytope is also illustrated in Fig. 6.19.

At this point, the algorithm takes a branching path: if the starting 'contracted' polytope is the original, the number of lattice points should be small enough that a stochastic enumerative sampler can be utilized to calculate the hive volume. That is, we can perform a CHAR

on the original hive saving only unique lattice points until the number of such unique points appears to become stationary with respect to some computational heuristic. The number of discovered lattice points directly yields the LRC for the weight tuple.

If the hive volume is large, multiple contractions will be necessary. In this branch, we need to estimate the lattice size, as direct counting methods are clearly unfeasible (especially in high dimensions, where the curse of dimensionality will prevent us from reliably sampling from a subset of the target space). Given $\tilde{\xi}$, we now have a sequence of nested polytopes with decreasing volume from our desired original hive such that each contracted polytope is wholly contained in the next larger, and the geometry is preserved (in contrast to the methods in [27] that rely on nested hyperballs within the desired convex body that require delicate arguments and rounding procedures to ensure that in high dimensions the bulk of the desired polytope volume is not excised by even the largest inscribing sphere). Following the volume ratio arguments provided by [50], we consider the sequence of n polytopes $P^{\lambda}_{\mu\nu}(\xi_n \in [\tilde{\xi}, \tilde{\xi}+2, \ldots, 0])$ such that $P^{\lambda}_{\mu\nu}(\xi_0) = P^{\lambda}_{\mu\nu}(\tilde{\xi})$ and $P^{\lambda}_{\mu\nu}(\xi_n) = P^{\lambda}_{\mu\nu}(0) = P^{\lambda}_{\mu\nu}$. This sequence admits volume ratios between successive contractions that scale by at most a constant. If $\tilde{\xi}$ is not even, we include one additional ratio down to the minimum that will clearly have a volume ratio even closer to 1 than the others. We assume $\tilde{\xi}$ is even for this discussion.

By the telescoping volume argument,

$$vol(P^{\lambda}_{\mu\nu}) = vol(P^{\lambda}_{\mu\nu}(\tilde{\xi})) \prod_{n=0}^{n-1} \frac{vol(P^{\lambda}_{\mu\nu}(\xi_{n+1}))}{vol(P^{\lambda}_{\mu\nu}(\xi_n))} \,. \tag{6.59}$$

We push this to the d-dimensional lattice volumes contained within each convex contraction, letting our hive sequence be defined by $HIVE(\mu, \nu, \lambda)(\xi_n) = P^{\lambda}_{\mu\nu}(\xi_n) \cap \mathbb{Z}^d$.

The innermost hive is estimated directly by a unique accumulating CHAR just as in the minimal case. We then estimate the successive lattice volume ratios by first performing a fixed number of steps in a CHAR on the largest (original) hive. We check to see how many of these points fall inside the next inner contracted polytope. The ratio of the total number of samples to the number of samples that fall inside the next contracted interior is proportional

to our desired volume ratio. To save computational time, we note that the original random walk on the largest space, if enough data was sampled for the distribution to be nearly uniform, will induce a nearly uniform distribution of points in each of the contracted hives as well. As a result, we can then save the points that tested positive to lie in the interior of the contracted hive, and resample from the smaller hive only enough points such that the relative error between each ratio remains constant. This outer-to-inner sampling procedure was demonstrated by [27] to save over 70% time consumption for a wide range of polytopes. Repeating this process until all of the lattice volume ratios are known will yield the required telescoping product constituents. For the inner starting points, we choose from the uniform distribution over the previously sampled points known to be in the contracted interior, and proceed with a new CHAR.

Our implementation of the lattice CHAR works directly with the rhombus constraints. The maximal hive produced by the LP serves as a starting hive for the random walk. We treat each interior bulk hive index as a coordinate direction in the polytope space. We systematically check each index for 'flex': that is, until we find a coordinate that has the ability to take on a different integer value while still satisfying the rhombus inequalities, we proceed to examine the 12 rhombuses associated with each coordinate (4 vertical, 4 left facing, 4 right facing) and thereby find the integer subset over which the inequalities would still hold. This is an exact constant time process unlike Cousins' algorithm that, although general to handle arbitrary convex bodies, requires a bisection subdivision search to approximate the intersection of the hit-and-run axis with the boundary of the polytope. If each coordinate has an empty subset, the hive is 'tight' and may indicate that there is only 1 integer solution for the provided weight vectors—the algorithm then returns. The first instance of flex becomes the first coordinate choice, wherein a new value is chosen from the uniform distribution on the available integer line segment. New coordinates are chosen uniformly randomly from the total bulk index set, their allowed 1D integer spaces are computed, and new values are selected. The random walk proceeds in this way for a fix number of steps, ensuring that we always remain in the HIVE space by construction (therefore no rejection sampling is needed),

and we walk directly on the integer lattice without having to round our walk.

6.12.1 Results of the Lattice Algorithm

We note that this algorithm relies on a few key assumptions. Foremost, we require that our inner hive estimation is good. A variety of convergence heuristics can be employed to determine when the inner unique walk has settled; however, if the contracted volume has lattice points that are not aligned with our coordinatization of the hive polytope, then this process will always under-represent the hive volume. For example, each individual coordinate may appear tight with respect to the starting solution from the LP. However, global changes in the bulk coordinates (or the simultaneous change in simply more than one coordinate at a time) may have enabled a new integer point to be found. This is not accessible from our CHAR due to our basis choice. Although it is a natural basis for the hive lattice, there is no guarantee that the polytope is coordinate aligned.

Future work in characterizing unimodular (lattice preserving) transforms of the hive polytope in order to better align the lattice with the hive coordinates is underway.

Fig. 6.20 shows the accuracy of this algorithm in the same comparison test used above with the Cousins' volume estimation. We see a large degradation of accuracy with the large error parameter. This is expected, as the error parameter conditions the initial convergence for the unique point accumulator in the minimal hive volume search, and if this is inaccurate, all subsequent products against this ratio will will be inaccurate. Lower relative error parameters product results competitive with the rounded algorithm described in Sec. 6.11.1.

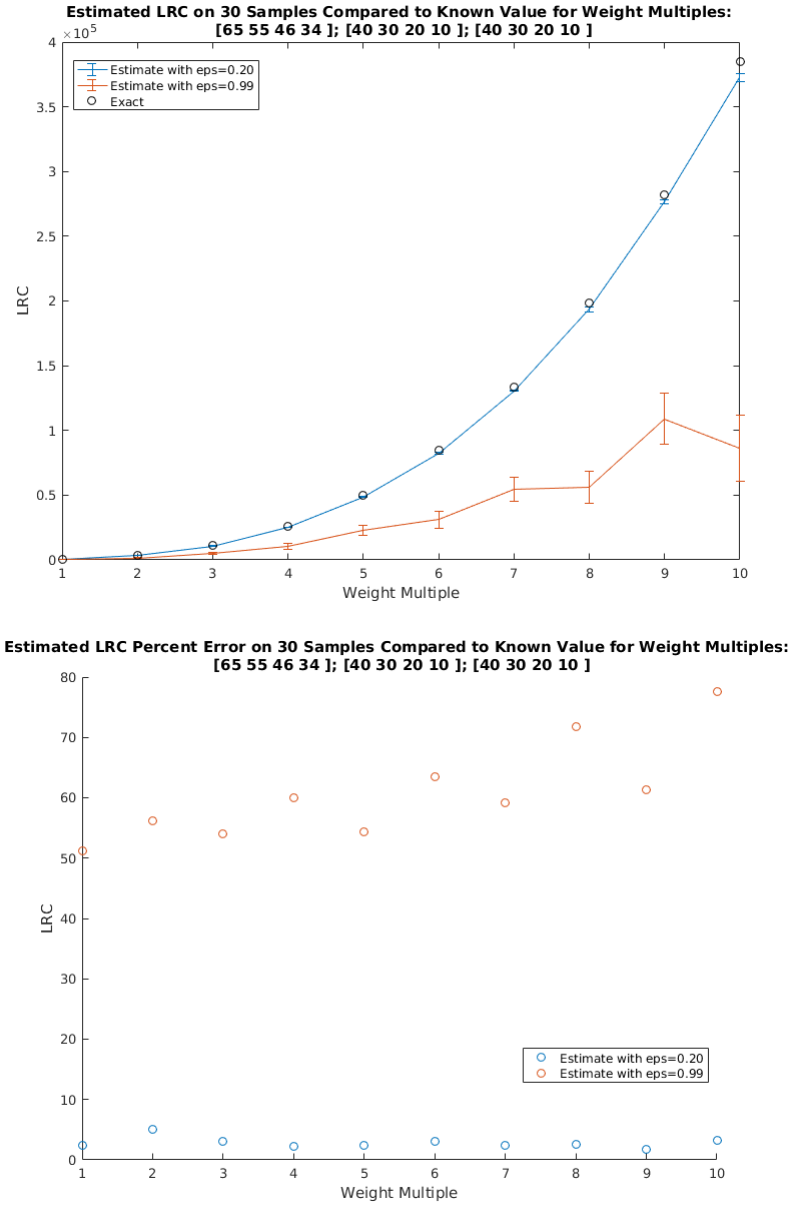

Figure 6.20: Accuracy of lattice LRC estimator for weight vector multiples, 95% confidence intervals and absolute percent error

The above results were hive volume scalings wherein the algorithm was able to perform a connected walk over the full hive space. A unique accumulating run over the original

full lattice would yield the exact LRC of 505 for the base weight vectors. However, the tuple $([40, 30, 20, 10], [40, 30, 20, 10], [65, 55, 45, 35])$, which is a near perturbation of the other tuple and has an LRC of 506, appears to contain a lattice point that is not aligned with the basis of our CHAR, and as a result, any long-running accumulating sampler only finds 505 unique configurations. This has dramatic effects on the quality of the estimations in general once we consider multiples of the weight vectors, and one can see the difference in the fractional errors illustrated in Fig. 6.21 for the same low error parameter as in the above sampling compared with other volume estimation algorithm over the same set. Now, even for the previously acceptable error parameter for roughly the same sized polytope volumes, we have poor accuracy. As mentioned, unimodular transforms may aid in this type of systematic inaccuracy, but this may be a characteristic failure of fixed axis CHAR algorithms on embedded discrete sets.

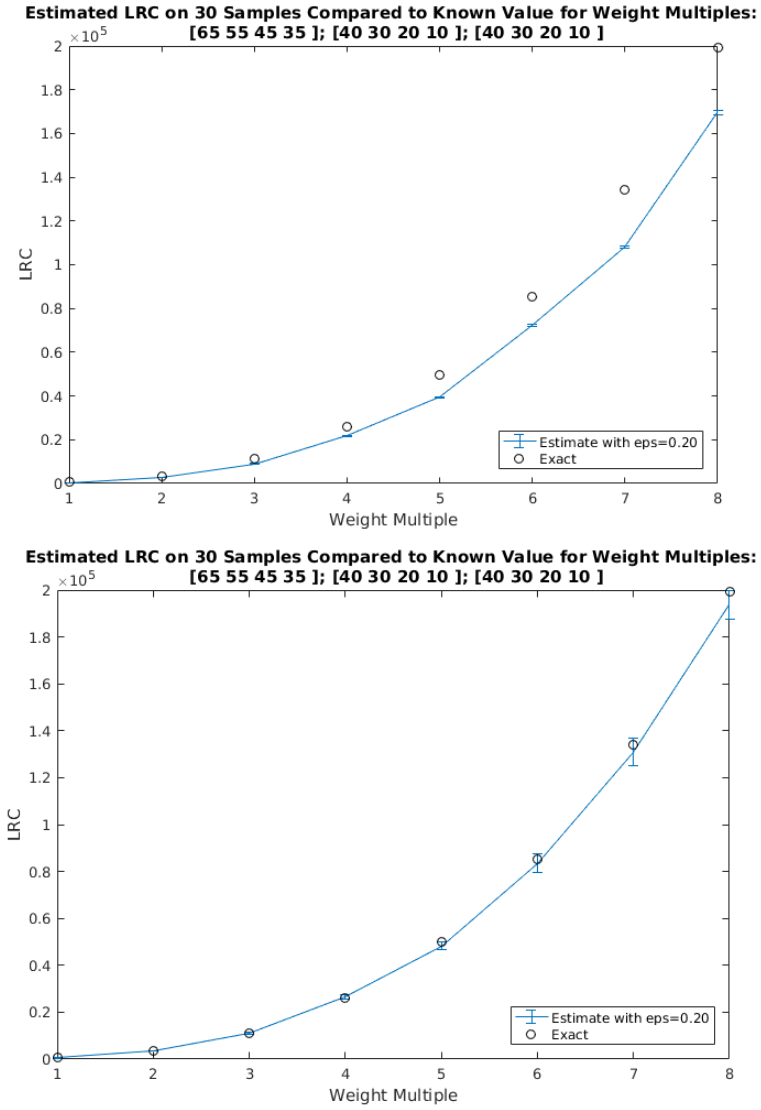

Figure 6.21: Accuracy of LRC estimators for weight vector multiples with poor lattice alignment with the rounded estimator on the bottom

Although there are no proven bounds on the mixing time of CHAR algorithms in the continuum, in practice they have been shown to have the same properties as traditional hit-and-run with the bonus of fewer computational steps [20]. On lattice walks, however, the CHAR is strongly susceptible to the issues presented here unless appropriate care is taken

based on foreknowledge of the lattice volume within the convex body one is trying to sample.

In the limit where the number of lattice points is assumed to be large, the rounding preprocessing of the polytope will not affect the estimation on an order more significant than the errors from the volume estimation itself, despite the fact that the transforms are not lattice preserving. However, for small lattice volumes, this affect can be comparable, and the direct lattice walk that preserves the structure outperforms in accuracy as shown in Fig. 6.22.

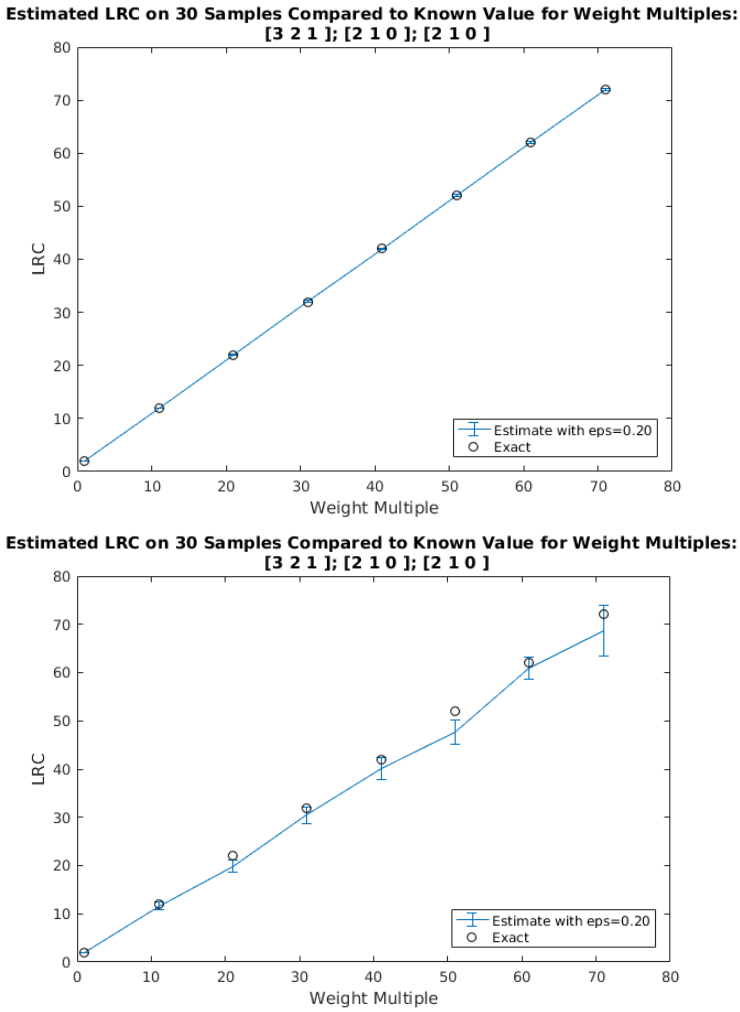

Figure 6.22: Accuracy of LRC estimators for weight vector multiples with small volume with the rounded estimator on the bottom

6.13 Future Work on Hives

We have presented an exploration of a few analytical and numerical aspects of combinatorial hives and their applications. Future directions for this research would involve finding an appropriate modification of the Appleby-Whitehead construction to produce real valued hives in all cases. With respect to Littlewood-Richardson calculations, finding and implementing unimodular rounding schemes would be greatly beneficial for both algorithms, producing

more accurate results with respect to lattice counts. A thorough study of the algorithms for much higher dimensional vector spaces should also be undertaken to better characterize their efficiency.

Chapter 7

FINAL THOUGHTS

The problems presented in this thesis are storied in their history, rich in their merit, and despite concentrated effort from the respective areas in which these challenges arise, only just now are the paths toward their potential solutions being firmly shaped. And yet, notwithstanding the uncertain gamble of the plunge in attempting to address these problems, we have still demonstrated novel approaches to tackling them, from introducing an innovative paradigm for studying emergent geometry, to algorithmic developments for sampling the space of abstract simplicial complexes, to advancements in the practical usage and numerical properties of combinatorial hives. In each chapter, we have outlined particular direct action that can be taken to further these studies by highlighting our open questions and immediate directions to take. However, with regard to our work on quantum gravity, we would like to provide perspective on the broader goal of our research and fruitful paths forward. Certainly there is much work to be done studying the IR limits of our theory, understanding combinatorial diffeomorphisms and the flow toward macroscopic geometry, probing bulk-boundary correlations, and extending the model toward making contact with existing physics. Ultimately, however, our paradigm was constructed with the intention to ask what are the minimal elements required to reproduce emergent macroscopic piecewise linear geometry from foundational building blocks without explicit prescription. More generally, we use this theory to question the assumptions that we build into our effective theories, and removing those assumptions so that they can instead materialize as complex statistical behavior, we attempt to formalize a model that can begin to rigorously distinguish which properties are intrinsic to the mathematics of combinatorial geometry, and which are intrinsic to separate postulates imposed to reproduce the physics of our universe. We encourage

future research both within our paradigm and using new techniques to further disentangle these concepts, and importantly, to map such constructions onto contemporary frameworks for quantum gravity.

In addition to the presentation of our results, we hope to have also imparted upon the reader the criticality of the confluence of the wide array of techniques from disparate fields that was necessary for such progress to be made. As the boundaries of our collective knowledge continue to be pushed in narrow bands through intensely pointed study, we would like to take a moment to highlight that a broad approach that pulls together both research and researchers from disjoint branches of science to concentrate on a common problem has been and will continue to be an incredibly effective tool in our kit. Further, without the willingness to explore beyond what is comfortable for progress in graduate study, and without also the sincerely appreciated willingness of our peers to learn foreign research dialects to communicate ideas across new landscapes for mutual benefit, the issues tackled in this thesis would have surely not been actioned upon during this graduate tenure. It has been a tremendous pleasure and privilege to make some strides, however small, toward a better understanding of these topics, and we again extend our gratitude to the curious colleagues who have enabled this endeavor and joined us for segments of our journey to make the unknown known.

BIBLIOGRAPHY

[1] J. Ambjørn, J. Jurkiewicz, and R. Loll. The Spectral Dimension of the Universe is Scale Dependent. *Physical Review Letters*, 95(17):171301, October 2005.

[2] Jan Ambjorn, Jerzy Jurkiewicz, and Renate Loll. Quantum Gravity, or The Art of Building Spacetime. In D. Oriti, editor, *Approaches to Quantum Gravity*, chapter Quantum Gravity, or The Art of Building Spacetime. Cambridge University Press, 2006.

[3] Jan Ambjorn, Jerzy Jurkiewicz, and Renate Loll. Quantum gravity as sum over spacetimes. *Lect. Notes Phys.*, 807:59–124, 2010.

[4] Franklin Antonio. Faster line segment intersection. In David Kirk, editor, *Graphics Gems III (IBM Version)*, pages 199 – 202. Morgan Kaufmann, San Francisco, 1992.

[5] Glenn Appleby and Tamsen Whitehead. Honeycombs from hermitian matrix pairs. *Discrete Mathematics and Theoretical Computer Science*, pages 899–910, 2014.

[6] Neil Ashby. Relativity and the global positioning system. *Physics Today*, 41, May 2002.

[7] John C. Baez. An Introduction to Spin Foam Models of Quantum Gravity and BF Theory. *Lect. Notes Phys.*, 543:25–94, May 2000.

[8] Benjamin Bahr and Bianca Dittrich. Regge calculus from a new angle. *New Journal of Physics*, 12(3):033010, 2010.

[9] Tim J. Benham. Uniform distribution over a convex polytope. School of Mathematics and Physics, University of Queensland, 2012. Matlab.

[10] Alain Berlinet and Christine Thomas. *Reproducing kernel Hilbert spaces in Probability and Statistics*. Kluwer Academic Publishers, 2004.

[11] Ginestra Bianconi, Christoph Rahmede, and Zhihao Wu. Complex quantum network geometries: Evolution and phase transitions. *Phys. Rev. E*, 92:022815, Aug 2015.

[12] N. Boumal, B. Mishra, P.-A. Absil, and R. Sepulchre. Manopt, a Matlab toolbox for optimization on manifolds. *Journal of Machine Learning Research*, 15:1455–1459, 2014.

[13] Anders Buch. Littlewood-richardson calculator, 1999.

[14] Armindo Costa and Michael Farber. Random simplicial complexes. In Filippo Callegaro, Frederick Cohen, Corrado De Concini, Eva Maria Feichtner, Giovanni Gaiffi, and Mario Salvetti, editors, *Configuration Spaces: Geometry, Topology and Representation Theory*, pages 129–153. Springer International Publishing, Cham, 2016.

[15] Ben Cousins and Santosh Vempala. A practical volume algorithm. *Mathematical Programming Computation*, 8(2):133–160, 2016.

[16] V. I. Danilov and G. A. Koshevoy. Discrete convexity and hermitian matrices. *Proceedings of the Steklov Institute of Mathematics*, 241:58–78, 2003.

[17] R. Dedekind. Uber zerlegungen von zahlen durch ihre grossten gemeinsamen teiler. *Festschrift der Technischen Hochschule zu Braunschweig bei Gelegenheit der 69. Versammlung Deutscher Naturforscher und Arzte*, pages 1–40, 1897.

[18] Sanjib Dey, Anha Bhat, Davood Momeni, Mir Faizal, Ahmed Farag Ali, Tarun Kumar Dey, and Atikur Rehman. Probing noncommutative theories with quantum optical experiments. *Nuclear Physics B*, 924:578 – 587, 2017.

[19] Bianca Dittrich and Sebastian Steinhaus. Time evolution as refining, coarse graining and entangling. *New Journal of Physics*, 16(12):123041, December 2014. arXiv: 1311.7565.

[20] I. Emiris and V. Fisikopoulos. Efficient random-walk method sfor approximating polytope volume. In *Proceedings of the 30th Annual Symposium on Computational Geometry*, page 318. ACM, 2014.

[21] Charles Fefferman, Sanjoy Mitter, and Hariharan Narayanan. Testing the manifold hypothesis. *J. Amer. Math. Soc.*, February 2016.

[22] L. H. Ford. Gravitational radiation by quantum systems. *Ann. Phys.*, 144(2):238–248, 1982.

[23] Robin Forman. Bochner's Method for Cell Complexes and Combinatorial Ricci Curvature. *Discrete & Computational Geometry*, 29(3):3, February 2003.

[24] Laurent Freidel and David Louapre. Diffeomorphism and spin foam models. *Nucl.Phys. B*, 662, December 2002.

[25] R. Friedberg and T.D. Lee. Derivation of Regge's Action from Einstein's Theory of General Relativity. *Nucl. Phys. B*, 3(242):242, Feb 1984.

[26] G. Gabrielse, D. Hanneke, T. Kinoshita, M. Nio, and B. Odom. New determination of the fine structure constant from the electron g value and qed. *Phys. Rev. Lett.*, 97, 2006. Erratum, Phys. Rev. Lett. 99, 039902 (2007).

[27] Cunjing Ge, Feifei Ma, and Jian Zhang. A fast and practical method to estimate volumes of convex polytopes. *CoRR*, abs/1401.0120, 2014.

[28] Charles Geyer. Introduction to mcmc. In Steve Brooks, Andrew Gelman, Galin Jones, and Xiao-Li Meng, editors, *Handbook of Markov Chain Monte Carlo*, chapter Introduction to MCMC. Chapman and Hall, 2011.

[29] Josiah Willard Gibbs. *Elementary Principles in Statistical Mechanics.* Charles Scribners Sons, 1902.

[30] J. B. Hartle and S. W. Hawking. Wave function of the universe. *Phys. Rev. D*, 28:2960–2975, Dec 1983.

[31] Allen Hatcher. *Algebraic Topology.* Cambridge University Press, 2002.

[32] Sabine Hossenfelder. Phenomenology of space-time imperfection i: Nonlocal defects. *Phys. Rev. D*, 88(124030):124030, December 2013.

[33] Sabine Hossenfelder. Phenomenology of space-time imperfection ii: Local defects. *Phys. Rev. D*, 88(124031):124031, December 2013.

[34] C.J. Isham. Quantum geometry. In Steven Christensen, editor, *Quantum Theory of Gravity*, chapter Quantum Geometry. Adam Hilger Ltd, Techno House, 1984.

[35] Mark R. Jerrum, Leslie G. Valiant, and Vijay V. Vazirani. Random generation of combinatorial structures from a uniform distribution. *Theoretical Computer Science*, 43:169 – 188, 1986.

[36] Matthew Kahle. Topology of random simplicial complexes: A survey. *AMS Contemp. Math.*, 620:201–22, 2014.

[37] Oliver Knill. A graph theoretical Gauss-Bonnet-Chern Theorem, November 2011.

[38] Allen Knutson and Terence Tao. The honeycomb model of $gl_n(\mathbb{C})$ tensor products i: Proof of the saturation conjecture. *J. Amer. Math. Soc.*, 12:1055–1090, 1999.

[39] D. E. Littlewood and A. R. Richardson. Group characters and algebra. *Philosophical Transactions of the Royal Society of London*, 233:99–141, 1934.

[40] Renate Loll. Discrete approaches to quantum gravity in four dimensions. *Living Reviews in Relativity*, 13, 1998.

[41] Renate Loll. A discrete history of the lorentzian path integral. In D. Giulini, C. Kiefer, and C. Lammerzahl, editors, *Quantum Gravity: From Theory to Experimental Search*, chapter A Discrete History of the Lorentzian Path Integral, pages 131–171. Springer, 2003.

[42] Renate Loll. The Emergence of Spacetime, or, Quantum Gravity on Your Desktop. *Classical and Quantum Gravity*, 25(11):11, June 2008.

[43] John Lombard. Network gravity. *Phys. Rev. D*, 95:024001, Jan 2017.

[44] John Lombard. Honey from the hives: A theoretical and computational exploration of combinatorial hives. *Experimental Mathematics*, 2018.

[45] L. Lovasz and S. Vempala. Simulated annealing in convex bodies and an $O^*(n^4)$ volume algorithm. *J. Comput. Syst. Sci*, 72(2):392–417, 2006.

[46] S Maletic and M Rajkovic. *Complex Networks (Studies in Computational Intelligence Series)*, volume 207, chapter Simplicial Complex of Opinions on Scale-Free Networks, pages 127–34. Springer-Verlag, Berlin, 2009.

[47] Warner A. Miller. The Hilbert action in Regge calculus. *Classical and Quantum Gravity*, 14(12):12, December 1997.

[48] Tomas Moller. A fast triangle-triangle intersection test. *Journal of Graphics Tools*, 2(2):25–30, 1997.

[49] H. Narayanan. On the complexity of computing kostka numbers and littlewood-richardson coefficients. *Journal of Algebraic Combinatorics*, 24(3), November 2006.

[50] Hariharan Narayanan. Estimating certain non-zero littlewood-richardson coefficients. *Formal Power Series and Algebraic Combinatorics*, 06 2014.

[51] Yasunori Nishimori, Shotaro Akaho, and Mark D. Plumbley. Riemannian optimization method on the flag manifold for independent subspace analysis. In Justinian Rosca, Deniz Erdogmus, José C. Príncipe, and Simon Haykin, editors, *Independent Component Analysis and Blind Signal Separation: 6th International Conference, ICA 2006, Charleston, SC, USA, March 5-8, 2006. Proceedings*, pages 295–302. Springer Berlin Heidelberg, Berlin, Heidelberg, 2006.

[52] T. Padmanabhan and Dawood Kothawala. Lanczos-lovelock models of gravity. *Physics Reports*, 531(3):3, October 2013.

[53] Alejandro Perez. The new spin foam models and quantum gravity. *Papers in Physics*, 4(040004):040004, 2012.

[54] Alejandro Perez. The spin foam approach to quantum gravity. *Living Rev. Rel*, 16(3):1205–2019, 2013.

[55] M. Planck. Uber irreversible strahlungsvorgange. *Verl. d. Kgl. Akad. d. Wiss.*, 1899.

[56] E. Rassart. A polynomiality property for littlewood-richardson coefficients. *Journal of Combinatorial Theory*, A 107(2):161–179, 2004.

[57] T. Regge. General relativity without coordinates. *Il Nuovo Cimento (1955-1965)*, 19(3):558–571, Feb 1961.

[58] Carlo Rovelli. *Quantum Gravity*. Cambridge University Press, 2004.

[59] Carlo Rovelli and Francesca Vidotto. *Covariant Loop Quantum Gravity*. Cambridge University Press, 2015.

[60] J. J. Sakurai and San F. Tuan. *Modern quantum mechanics*. Addison-Wesley Pub. Co., revised edition, September 1994.

[61] D. M. Y. Sommerville. *An Introduction to the Geometry of n Dimensions*. Dover, New York, 1958.

[62] Tamon Stephen and Timothy Yusun. Counting inequivalent monotone boolean functions. *Discrete Applied Mathematics*, 167:15 – 24, 2014.

[63] Marc A A van Leeuwen. *The Littlewood-Richardson rule, and related combinatorics*, volume 11 of *MSJ Memoirs*, pages 95–145. Mathematical Society of Japan, 2001.

[64] O.Y. Viro V.G. Turaev. State sum invariants of 3-manifolds and quantum 6j-symbols. *Topology*, 31(4):865–902, October 1992.

[65] Steven Weinberg. A model of leptons. *Phys. Rev. Lett.*, 19:1264–1266, Nov 1967.

[66] E Wigner. Characteristic vectors of bordered matrices with infinite dimensions. *Ann. of Math*, 62:548–564, 1955.

[67] Zhihao Wu, Giulia Menichetti, Christoph Rahmede, and Ginestra Bianconi. Emergent complex network geometry. *Nature Scientific Reports*, 5(10073):10073, December 2015.

[68] Konstantin Zuev, Or Eisenberg, and Dmitri Krioukov. Exponential random simplicial complexes. *Journal of Physics A: Mathematical and Theoretical*, 48(46):465002, 2015.